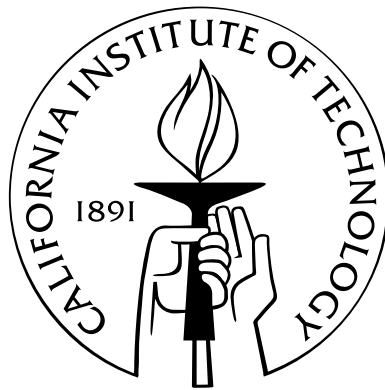


Earthquake source characterization using 3D Numerical Modeling

Thesis by
Vala Hjörleifsdóttir

In Partial Fulfillment of the Requirements
for the Degree of
Doctor of Philosophy



California Institute of Technology
Pasadena, California

2007
(Defended March 13, 2007)

© 2007

Vala Hjörleifsdóttir

All Rights Reserved

Acknowledgements

I have now spent a large part of my adult life at Caltech, with the overarching goal of writing this thesis. As such, it seems that everyone that has somehow touched my life during this time, owns a little, or not so little, part of it. Academically, many people have contributed in a very direct way to the thesis. First I would like to thank my advisor, Jeroen Tromp, for being very supportive and patient. I would like to thank Jeroen for giving me the freedom to study what I was interested in, guidance when I needed it and always taking the time to listen to me. Much of this thesis represents continued work on what started off as a class project in Hiroo Kanamori's class when I was his TA, and I have benefitted tremendously from his continued input, guidance and help. It has been a tremendous experience for me to work with two such great, and different, researchers.

I have also worked with many of the students in the lab, and in particular Brian Savage, Qinya Liu and Ozgun Konca have taught me a lot and been very helpful. Many of the plots in this thesis trace their ancestry to Brian's, Qinya's and Ozgun's codes. I was a diligent attendee of the Seismolab coffee break for a long time and I very much enjoyed the interaction with the people there, especially Hiroo, Don Anderson, Clarence Allen, Jascha Polet, Anupama Venkataraman, Tom Heaton and Mark Simons. Those were some of the most fun and educative times at the lab. Furthermore, the field trips, in particular the cruise on the R.V.I.B Nathaniel B. Palmer, the division field trip to Hawaii, and several field trips to the Sierras, Death Valley and Utah have given me the chance to explore the Earth without the aid of a computer.

The members of the staff at Caltech are truly amazing at what they do, and I have been continually impressed with their competence, and I very much thank everyone that has helped me throughout the years.

When work is such a big part of ones life, the lines between work life and personal life blur, and ups and downs in one inevitably cause ups and downs in the other. The

first people to feel it when the codes are not working, or the results are not as expected are the office mates. I would like to thank Leo, Sidao, Charlotte, Kaiwen, Jane, Alisa, Chris, YoungHee and Lijun (in order of appearance) for putting up with me. I hope the chocolate helped make up for some of my cursing. We should never have stopped the Wednesday beer on Thursday tradition. I have been very lucky that Viola Carter has been the administrative assistant for Jeroen during my stay here, as she is, in my opinion, the glue that keeps the lab together. Thanks for always being up to something silly, and for always going over and beyond helping me, whether it had to do with the student faculty retreat, travel reimbursements or personal matters. But the biggest thanks for being a friend. I would like to thank my “oldest” friends at Caltech, Junjun, Ozgun, Brian, Javier, Jane, Anu and Jascha for always being ready to go to coffee when fortran could not decide whether a variable should be in single or double precision, or when life just sucked for other reasons. I would like to thank Oliver, for coming here with me. Things don’t always work out like we hope, but what is life if we are not brave and try our best.

I was very fortunate to get to know another group of friends, that I have had a lot of fun with during my later years here; thanks to Hannes, Gerdur, Helen, Kristján, Lisa, Guillaume, Alan and Allison for letting me be my sometimes over the top Icelandic self. I would also like to thank my “second family”; Angel, Chris and Lydia, for all the good times. Your friendship means a lot to me. Special thanks to Angel for always being there. With all of this written, I still have so many good memories shared with people I have yet to mention. To all of you, thanks, you know who you are.

I would also like to take this opportunity to thank the people that I worked with at the Science institute in Iceland before coming to Caltech; Bryndís Brandsdóttir, Páll Einarson and Leó Kristjánsson. They gave me my first opportunities to work on geophysics research, even though I did not know much and my greatest qualification was that i was big and could carry car batteries. Special thanks to Bryndís, my geophysical mother. I also would like to thank Freysteinn Sigmundsson for encouraging me to apply to Caltech, without your input my life would have taken a very different direction.

And, in the tradition of always keeping the best piece of chocolate for last, I would like to thank my family: my parents, Bibba and Hjöllli; siblings, Anna and Einar; grandparents, Vala, Siggi, Lillý and Einar; aunts and uncles, for countless messages, emails, christmas cards and phone calls, reminding me that life is so much more than a silly thesis.

Abstract

To understand the physics of earthquakes, it is important to know what happens during individual events. Disassembling the information about the source process from the recorded seismograms is a difficult and non-unique process, as there are severe trade-offs between many of the source parameters. In this thesis we attempt to add information from frequencies not used during the initial modeling of individual events to put more constraints on the source process, to learn about specific source parameters important to the physics of earthquakes. We model earthquakes using a spectral element method for wave-propagation that accurately accounts for the Earth's 3D elastic structure. We study the rupture speed of the 2001 Kunlun, China earthquake, the continuity of slip during the 1998 Balleny Islands event and the duration of slip during the 2004 Sumatra-Andaman, Indonesia earthquake. Finally, we explore the feasibility of using adjoint methods to learn about the earthquake source.

Contents

Acknowledgements	iii
Abstract	v
1 Introduction	1
2 The 2001 Bhuj, India earthquake	3
2.1 Introduction	3
2.2 Data retrieval and processing	5
2.3 Quantifying the quality of a model	5
2.3.1 Combining measurements	6
2.4 Importance of the crust	8
2.5 Discussion	23
3 The 2001 Kunlun, China earthquake	24
3.1 Introduction	24
3.2 Body-wave modeling	25
3.2.1 Data	25
3.2.2 Inversion	27
3.2.3 Body-wave inversion results	29
3.3 Surface-wave analysis	36
3.3.1 Data and measurements	36
3.3.2 Results	36
3.4 Relationship between surface offsets and the moment-rate function	42
3.5 Conclusions	44

4	The 1998 Balleny Islands earthquake	46
4.1	Introduction	46
4.2	Point sources	48
4.3	Body-wave source model	49
4.4	Modification of the body-wave model	58
4.5	Discussion	60
4.6	Conclusions	65
5	The 2004 Sumatra, Indonesia earthquake	67
5.1	Introduction	67
5.2	Constraints from long-period surface waves	67
5.2.1	Data and processing	67
5.2.2	Harvard CMT and preliminary finite-fault model	68
5.2.3	Final slip models	71
5.3	Constraints from GPS measurements	74
5.3.1	Data and modeling	76
5.3.2	Results	77
5.4	Discussion and conclusions	78
5.5	Acknowledgements	80
6	Adjoint source inversions	81
6.1	Introduction	81
6.2	Theory	82
6.3	The connection between adjoint methods, time-reversal imaging and stacking	87
6.4	Back-propagation of high frequency radiation	89
6.4.1	Stacking	90
6.4.2	Time-reversal imaging of high-frequency data	94
6.5	Time-reversal imaging of long-period data	94
6.5.1	Data and processing	96
6.5.2	Interpretation of adjoint strain maps	97
6.5.3	Application to the 2004 Sumatra earthquake	98
6.5.4	Application to the 2001 Kunlun China earthquake	98
6.5.5	Application to the 1998 Balleny Islands earthquake	108

6.6	Conclusions and future direction	112
6.7	Acknowledgments	113
A	Quantifying differences between two time series: Multitaper measurements	114
A.1	Multitaper measurements	115
A.2	Prolate spheroidal eigentapers	116
A.3	Transfer function for multitaper measurements	118
A.4	Effect of taper parameters	119
A.5	Combining measurements	119
B	Fault-Plane Kernels	123

List of Figures

2.1	Map and focal mechanism for the 2001 Bhuj earthquake.	4
2.2	Data, synthetics and reconstructed synthetics for a 1D Earth model (a) . . .	9
2.3	Data, synthetics and reconstructed synthetics for a 1D Earth model (b) . . .	10
2.4	Data, synthetics and reconstructed synthetics for a 1D Earth model (c) . . .	11
2.5	Data, synthetics and reconstructed synthetics for a 1D Earth model (d) . . .	12
2.6	Data, synthetics and reconstructed synthetics for a 1D Mantle model combined with a 3D crustal model (a)	13
2.7	Data, synthetics and reconstructed synthetics for a 1D Mantle model combined with a 3D crustal model (b)	14
2.8	Data, synthetics and reconstructed synthetics for a 1D Mantle model combined with a 3D crustal model (c)	15
2.9	Data, synthetics and reconstructed synthetics for a 1D Mantle model combined with a 3D crustal model (d)	16
2.10	Data, synthetics and reconstructed synthetics for a 3D Earth model (a) . . .	17
2.11	Data, synthetics and reconstructed synthetics for a 3D Earth model (b) . . .	18
2.12	Data, synthetics and reconstructed synthetics for a 3D Earth model (c) . . .	19
2.13	Data, synthetics and reconstructed synthetics for a 3D Earth model (d) . . .	20
2.14	Time shifts $\delta\tau$, and amplitude anomalies $\delta \ln A$ for a period of 207 seconds. .	21
2.15	Amplitude and phase anomalies, averaged over all stations, as a function of frequency.	22
3.1	Map showing the location of the Kunlun earthquake.	26
3.2	Data used for body-wave inversions.	27
3.3	Slip distributions obtained with fixed rupture speeds and the moment con- strained to values obtained from surface waves (a).	31

3.4	Slip distributions obtained with fixed rupture speeds and the moment constrained to values obtained from surface waves (b).	32
3.5	Moment-rate functions for models constrained to a moment of $M_0 = 6.75 \times 10^{20}$ Nm.	33
3.6	Waveform fits obtained for slip distributions with the rupture speed fixed at (i) 2.5 km/s (ii) 3.0 km/s (iii) 3.5 km/s (iv) 4.0 km/s (v) 4.5 km/s.	34
3.7	Waveform misfit as a function of rupture speed.	35
3.8	Amplitude ratios ($\delta \ln A$) and time shifts (δt) as measured at each station, for a frequency of 4.8 mHz (period of 207 seconds).	37
3.9	Multitaper measurements for the 3 different suites of models, for rupture speeds of 2.5, 3.0, 3.5, 4.0 km/s.	39
3.10	Same as Fig. 3.9, for rupture speeds $v_r=3.0, 3.2, 3.4, 3.6$ km/s.	40
3.11	Measurements of $\overline{\delta \ln A}$, $\overline{\delta \tau}$, $\sigma^{\ln A}$ and σ^τ	41
4.1	Map showing the location of the Balleny Island earthquake.	47
4.2	Radiation patters for three different unit point sources, computed at 256 seconds.	48
4.3	Waveforms at stations between 60 and 120 degrees computed for the Harvard CMT.	50
4.4	Amplitude anomalies and time shifts for the Harvard best-fit point source.	51
4.5	Source model from <i>Henry et al.</i> (2000) that is used in the simulations.	52
4.6	Waveforms computed for model HenryF.	54
4.7	Amplitude anomalies and time shifts for the <i>Henry et al.</i> (2000) source model, with focal mechanism HenryF.	55
4.8	Waveforms computed for model HenryD.	56
4.9	Amplitude anomalies and time shifts for the <i>Henry et al.</i> (2000) source model, with focal mechanism HenryD.	57
4.10	The modified slip model.	59
4.11	Same as Fig. 4.8 except with synthetics computed for the modified source model.	61
4.12	Amplitude anomalies and time shifts for the modified source model.	62
4.13	Moment-rate functions for the models presented, both in time domain and frequency domain.	63

4.14	Multitaper measurements averaged over all azimuths and over a band between 100 and 500 seconds.	64
5.1	Topography/Bathymetry in the region of the great 2004 Sumatra earthquake.	68
5.2	Slip distribution and waveforms computed for the preliminary finite-fault model.	69
5.3	Amplitude ratios and time shifts for the Harvard CMT and the preliminary slip model.	70
5.4	Slip distribution and waveforms computed for Model III.	72
5.5	Slip distribution and waveforms computed for Model II.	73
5.6	Amplitude ratios and time shifts for the final source models, Model II and Model III.	74
5.7	The moment rate of the Sumatra earthquake compared with a seismogram and the moment rate of the 2001 Kunlun earthquake.	75
5.8	Example of estimating the static field from the seismograms.	77
5.9	Observed and computed static displacements for model III.	78
5.10	Observed and computed static displacements for model II.	79
5.11	Observed and computed static displacements for model a static source model.	79
6.1	Cartoon depicting the difference between a forward simulation and an adjoint simulation.	84
6.2	Map showing the Hinet array, the Sumatra source region, and the region used for time-reversal simulations.	90
6.3	Brightness function in the Sumatra source region, obtained from stacking of unfiltered Hinet data.	92
6.4	Brightness function in the Sumatra source region, obtained from stacking of unfiltered Hinet data.	93
6.5	Time-reversed high-frequency data from the Hinet array.	95
6.6	Adjoint strain for the Sumatra earthquake, component EE	99
6.7	Adjoint strain for the Sumatra earthquake, component EZ	100
6.8	Adjoint strain for the Sumatra earthquake, component NE	101
6.9	Adjoint strain for the Sumatra earthquake, component NN	102
6.10	Adjoint strain for the Sumatra earthquake, component NZ	103
6.11	Adjoint strain for the Sumatra earthquake, component ZZ	104

6.12	Adjoint strain for the Kunlun earthquake, component EE	105
6.13	Adjoint strain for the Kunlun earthquake, component NE	106
6.14	Adjoint strain for the Kunlun earthquake, component EZ	106
6.15	Adjoint strain for the Kunlun earthquake, component NN	107
6.16	Adjoint strain for the Kunlun earthquake, component NZ	107
6.17	Adjoint strain for the Kunlun earthquake, component ZZ	108
6.18	Adjoint strain for the Kunlun earthquake, component EE	109
6.19	Adjoint strain for the Kunlun earthquake, component EZ	109
6.20	Adjoint strain for the Kunlun earthquake, component NE	110
6.21	Adjoint strain for the Kunlun earthquake, component NN	110
6.22	Adjoint strain for the Kunlun earthquake, component NZ	111
6.23	Adjoint strain for the Kunlun earthquake, component ZZ	111
A.1	Boxcar	116
A.2	2.5pi tapers	117
A.3	Effect of k	120
A.4	Effect of k	121

List of Tables

2.1	Average amplitude anomalies and time shifts for the three models, averaged over all stations and frequencies from 0 to 0.02 Hz	21
2.2	Average amplitude anomalies and time shifts for the three models, averaged over all stations and frequencies from 0 to 0.01 Hz	23
3.1	Crustal model used in body-wave source inversions	29
4.1	Comparison of focal mechanisms used to model the Balleny Island earthquake	48

Chapter 1

Introduction

At the core of earthquake seismology is understanding what happens during an earthquake, and why. The difficulty of studying many aspects of Earth science, and earthquake seismology in particular, is that several components of the experimental setup are not under our control. We cannot control where and when the earthquakes occur. Instead the community has diligently distributed seismometers around the globe, on sparsely populated islands, in the deserts of Africa and even on the South Pole, continuously recording data, waiting for the next signal to arrive. However, even with this great network of seismometers, the data available to study earthquakes is often not as complete as we had wanted and we are left to make judgments based on the limited data available. This leads to non-uniqueness.

As the recorded seismogram contain both information on the source of the earthquake and the propagation path between the source and the station, earthquake seismologists are left to separate the effects, in order to learn about the earthquake source. This leaves us to use the parts of the traces where the effects of the structure are well understood. In an oversimplification, we can say that the very long-period surface waves, which can in general be modeled well using simple 1D structural Earth models, give a point source view of the earthquake, such as the magnitude and the orientation of the fault plane involved. The first arrival body-waves have higher resolution to changes in the magnitude and orientation of slip along the fault-plane but are not very sensitive to the long period components of the slip, i.e. the moment.

The goal of this thesis is to increase the available data by using additional phases and periods, to add constraints to pre-existing models. By accurately accounting for the Earth's 3D structure, we can include phases that are sensitive to 3D structure in the modeling. Computing full wave field seismograms for a 3D structure is a difficult problem and compu-

tationally expensive. Here we use a spectral element method (SEM) to compute accurate 3D synthetics for finite source models and compare to data.

In Chapter 2 we develop measurement techniques that will be used throughout the thesis, applying the 3D modeling to the 2001 Bhuj, India earthquake, that had a simple source, in order to estimate how well we can account for the 3D structure.

In Chapter 3 we use traditional body-wave modeling to construct several different source models for the 2001 Kunlun, China earthquake, each with a fixed rupture speed. By computing global surface-waves for these models, and comparing them to data, we put a limit on the rupture speed. The rupture speed is critical in understanding the fracture energy of earthquakes.

In Chapter 4 we focus our attention on the 1998 Balleny Islands, Antarctic Plate earthquake. This large intraplate event is thought to have had a large non-double couple component and perhaps be comprised of two events separated by a 100 km unbroken patch. The unbroken patch implies dynamic triggering of earthquake rupture over a large distance. Here we show that we can match a wide range of data with continuous slip on a single fault plane, that can be explained by standard rupture-propagation models.

The 2004 Sumatra earthquake was the largest event to occur in the age of modern broadband seismology. In Chapter 5 we describe the constraints imposed on the source model by long-period surface waves, and 3D modeling of static offsets recorded on far-field GPS receivers. Due to the large size of the event we have to look at periods larger than those normally used to infer information about source processes.

In chapter Chapter 6 we describe how to use adjoint methods to obtain source models of earthquakes using a variety of data. We discuss the connection between adjoint methods, time-reversal and stacking. We apply time-reversal methods to high-frequency P-waves from the Sumatra earthquake, and compare with results from stacking. We further do time-reversal simulations of the Sumatra earthquake, as well as simulate the first step of an adjoint method to obtain better source models.

Chapter 2

The 2001 Bhuj, India earthquake

2.1 Introduction

In later chapters of this thesis we use 3D spectral-element method (SEM) numerical simulations of seismic wave propagation to extract information about the earthquake source, assuming that the Earth's elastic structure is accurately accounted for. In this chapter we wish to test that assumption for a source that is well known. This can be accomplished effectively by comparing data and synthetics for an event that has a simple source, i.e., a source that is compact in both space and time relative to the periods and wavelengths of the simulated waves.

The M_w 7.6, January 26, 2001, Bhuj, India, event (Fig. 2.1) fits this requirement very well. The rupture area is small, $40 \text{ km} \times 40 \text{ km}$, as inferred from aftershocks (*Negishi et al.*, 2001). Finite fault inversions indicate that the main slip occurred on a smaller patch of the fault, $15 \text{ km} \times 25 \text{ km}$ or $10 \text{ km} \times 20 \text{ km}$, as estimated by *Antolik and Dreger* (2003) and *Mori* (2001), respectively. Throughout the following chapters we consider waves with periods longer than 40 seconds and wavelengths on the order of hundreds of kilometers, much larger than the source dimensions. The source-time function of the Bhuj event is also short, about 20 s (*Antolik and Dreger*, 2003; *Mori*, 2001). Since the source region is much smaller than the wavelength of the waves we are considering and the source duration is shorter than the periods we use, the source can be adequately described as a point source for our purposes. Due to the large moment of the event, the signal-to-noise ratio is high, even at long periods. In this section we will focus on estimating the relative effects of the 3D crust and mantle on waveforms of surface waves. We use the Harvard centroid-moment tensor (CMT) solution (*Ekström et al.*, 2003) for all the simulations.

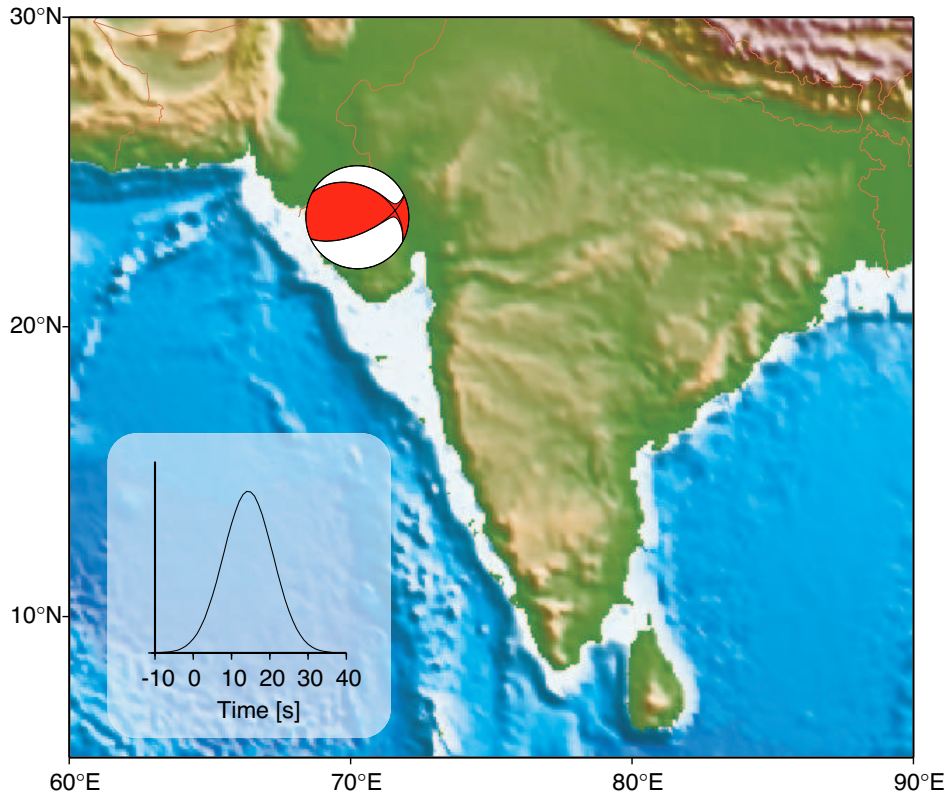


Figure 2.1: The 2001 Bhuj, India, earthquake ruptured a relatively small fault patch given its large magnitude. The compactness of the source, both in space and time, makes it ideal for studying the effects of 3D heterogeneity on seismic waveforms. The high variability in crustal structure near the source provides a difficult test for current 3D models. In this study we simulate the event based upon the moment tensor from the Harvard CMT catalog (*Ekström et al.*, 2003) and a Gaussian source-time function.

2.2 Data retrieval and processing

We retrieve data for the event from the IRIS data center (www.iris.edu) for most permanent global stations recording 1 sample-per-second broadband data. We remove the instrument response from the records using deconvolution to obtain ground displacement. For each event we calculate synthetic waveforms, using mode summation for one-dimensional (1D) Earth models and a spectral element method (SEM) for 3D Earth models (*Komatitsch and Tromp, 2002a,b*). We use 1D Earth model PREM (*Dziewonski and Anderson, 1981*) and a 3D Earth model that combines mantle model S20RTS (*Ritsema et al., 1999*) and crustal model Crust2.0 (*Bassin et al., 2000*). The 3D SEM synthetics incorporate the effects of gravity, rotation, topography and bathymetry, the oceans, and attenuation.

We limit our attention to the period range between 40 s and 500 s. The upper bound is determined by the noise at periods beyond the long-period corner of the instrument response (360 s for most stations used in this study), which tends to be amplified by deconvolution of the response; the lower bound reflects the shortest period of the 3D synthetics.

2.3 Quantifying the quality of a model

Throughout this thesis we will be comparing how well different models fit the observed data. Furthermore, we want to see how the differences vary with frequency. We choose to quantify the difference between the three component data, \mathbf{d} , and synthetics, \mathbf{s} , in terms of a transfer function that can be represented by two terms; a frequency-dependent amplitude anomaly $\delta \ln A_i(f)$ and a frequency-dependent time-shift $\delta \tau_i(f)$, for station i as a function of frequency f . We use a multi-taper measurement technique (*Thomson, 1982*) based on prolate spheroidal eigentapers (*Slepian, 1978*) following *Laske and Masters (1996)* and *Zhou (2004)*, to obtain the transfer function. A discussion on multi-taper measurements is given in appendix A. In this formulation the best model is the one that requires the smallest shifts and amplitude corrections.

We use an 800 second window centered on $t = \Delta/3.7$ km/s, where Δ is the epicentral distance, for the measurements. We use the first five 2.5π prolate spheroidal tapers to estimate the transfer function. This choice leads to independent estimates of the true spectra every $2.5/L$ Hz, where L is the length of the time series. For a window length of 800 s this corresponds to independent estimates every $2.5/800 = 0.003125$ Hz.

The transfer function tells us how to “multiply and shift” each frequency component in order to best fit the data. If the data and synthetics are similar to start with, the “reconstructed” synthetic will be nearly identical to the data. If the traces are dissimilar, there is no way to shift and multiply the different frequency components to make the traces look like each other. In this case the interpretation of the obtained measurements, $\delta \ln A_i(f)$ and $\delta \tau_i(f)$, is not obvious, and thus we discard those data. Again we are faced with choosing a misfit parameter. Three parameters that could be used are the waveform misfit:

$$WM = |\mathbf{d} - \mathbf{s}|^2 / (\mathbf{d} \cdot \mathbf{d}), \quad (2.1)$$

the maximum cross-correlation value (note that since the waveforms are already aligned, this is the value at zero shift),

$$CC_{max} = \mathbf{d} \cdot \mathbf{s} / [(\mathbf{d} \cdot \mathbf{d})(\mathbf{s} \cdot \mathbf{s})]^{1/2}, \quad (2.2)$$

and the “amplitude ratio” of the data and synthetics,

$$AR = (\mathbf{d} \cdot \mathbf{d}) / (\mathbf{s} \cdot \mathbf{s}) - 1. \quad (2.3)$$

It can be shown that when the data and synthetics are similar the waveform misfit is the square of the cross-correlation value. They start to differ when the waveform misfit is around 0.5. Both parameters measure the similarity of the waveforms. The amplitude ratio is measuring the overall similarity of the amplitude of the traces. We only retain measurements when the waveform misfit between the data and reconstructed synthetic is larger than 0.7 (or $CC_{max} > 0.84$). We discard data with amplitude ratios of 0.2 or larger. This procedure leads us to another estimate of the quality of a model. If the model is poor, many of the waveforms will be discarded. We therefore also track the number of stations with waveforms that are similar to the observed ones, according to the above criteria.

2.3.1 Combining measurements

Each multi-taper measurement gives us an estimate of the time shift, $\delta \tau_i(f)$, and the amplitude anomaly, $\delta \ln A_i(f)$, at station i and frequency f . This provides us with a large number of measurements for each model. In order to visualize the results we combine the

measurements, either integrating over all frequencies at a given station, monitoring the variation with receiver location or summing all the measurements at a given frequency over stations to see the variation with frequency. We define the average time shift at a given frequency as:

$$\overline{\delta\tau}(f) = \frac{1}{N} \sum_{i=1}^N \delta\tau_i(f), \quad (2.4)$$

and the average time-shift at station i :

$$\overline{\delta\tau}_i = \frac{1}{f_1 - f_0} \int_{f_0}^{f_1} \delta\tau_i(f) df; \quad (2.5)$$

finally, the average over all measurements is given by:

$$\overline{\delta\tau} = \frac{1}{N} \sum_{i=1}^N \frac{1}{f_1 - f_0} \int_{f_0}^{f_1} \delta\tau_i(f) df. \quad (2.6)$$

It can also be of interest to see how much the data vary around the average value. Since each measurement is not independent of the adjacent values, and is not normally distributed, these are not the standard deviations in the language of statistics, but the second moment of the measurements around the mean. We define the variations around the averages as:

$$\sigma^\tau(f) = \left\{ \frac{1}{N} \sum_{i=1}^N [\delta\tau_i(f) - \overline{\delta\tau}(f)]^2 \right\}^{\frac{1}{2}} \quad (2.7)$$

and the average time-shift at station i :

$$\sigma_i^\tau = \left\{ \frac{1}{f_1 - f_0} \int_{f_0}^{f_1} [\delta\tau_i(f) - \overline{\delta\tau}_i]^2 df \right\}^{\frac{1}{2}} \quad (2.8)$$

finally, the average over all measurements is given by:

$$\sigma^\tau = \left\{ \frac{1}{N} \sum_{i=1}^N \frac{1}{f_1 - f_0} \int_{f_0}^{f_1} [\delta\tau_i(f) - \overline{\delta\tau}]^2 df \right\}^{\frac{1}{2}} \quad (2.9)$$

For the amplitudes, we define $\overline{\delta \ln A}(f)$, $\overline{\delta \ln A}_i$, $\overline{\delta \ln A}$, $\sigma^{\ln A}(f)$, $\sigma_i^{\ln A}$, $\sigma^{\ln A}$ in the same manner.

2.4 Importance of the crust

Although we can compute waveforms for an Earth model which incorporates lateral variations in the crust and the mantle, it is of interest to see whether a simpler Earth model can produce similar fits to the data. Therefore, we calculate synthetic waveforms for the India event using three different Earth models: (1) 1D model PREM (*Dziewonski and Anderson, 1981*), (2) PREM combined with 3D crustal model Crust2.0 (*Bassin et al., 2000*), and (3) mantle model S20RTS (*Ritsema et al., 1999*) combined with Crust2.0.

We obtain multi-taper measurements of time shifts and amplitude ratios for the above mentioned models at 92 stations distributed globally. The data (black) are shown together with the synthetics (red) and the reconstructed synthetics (green) in figures 2.2–2.5, 2.6–2.9, 2.10–2.13 for the three respective Earth models. The data and synthetics are filtered between 50 and 500 seconds before applying the measurements. Together with each trace we show the four different misfit estimates between the data and the reconstructed synthetic, from left to right, top to bottom: WM , CC_{max}^2 , CC_{max} , and AR . Those parameters that are outside of the cutoff values are marked red. A total of 50, 46 and 73 traces pass the test for the three respective models. Notice that the traces that do not pass the test are those that are very different to start with, often those that have small amplitudes. Not surprisingly, the highest frequencies are the ones that are most poorly fit.

One could imagine that if a different low pass was applied, more traces would be retained. To examine this we repeat the exercise with different band passes, keeping the high pass at 500 seconds but varying the low pass from 40 to 200 seconds. The number of retained records is plotted as a function of frequency for the three models in figure 2.15. The number of records retained remains similar for periods between 50 and 200 seconds for the 3D model, but drops off more rapidly with frequency for the models with a 1D mantle. At 40 seconds only 50–70% of the records are retained.

We compare the amplitude anomalies and the time shifts for the records that are retained for all 3 models, for the band pass between 50 and 500 seconds (Fig. 2.15). The average amplitude anomalies, $\overline{\delta \ln A(f)}$ are similar for all models, indicating that the moment estimate would be similar for all three Earth models. The average time shifts, $\overline{\delta \tau(f)}$, however show a very different picture. The two models with a 1D mantle are on average faster than observed for the very long periods, but after that, they are significantly slower

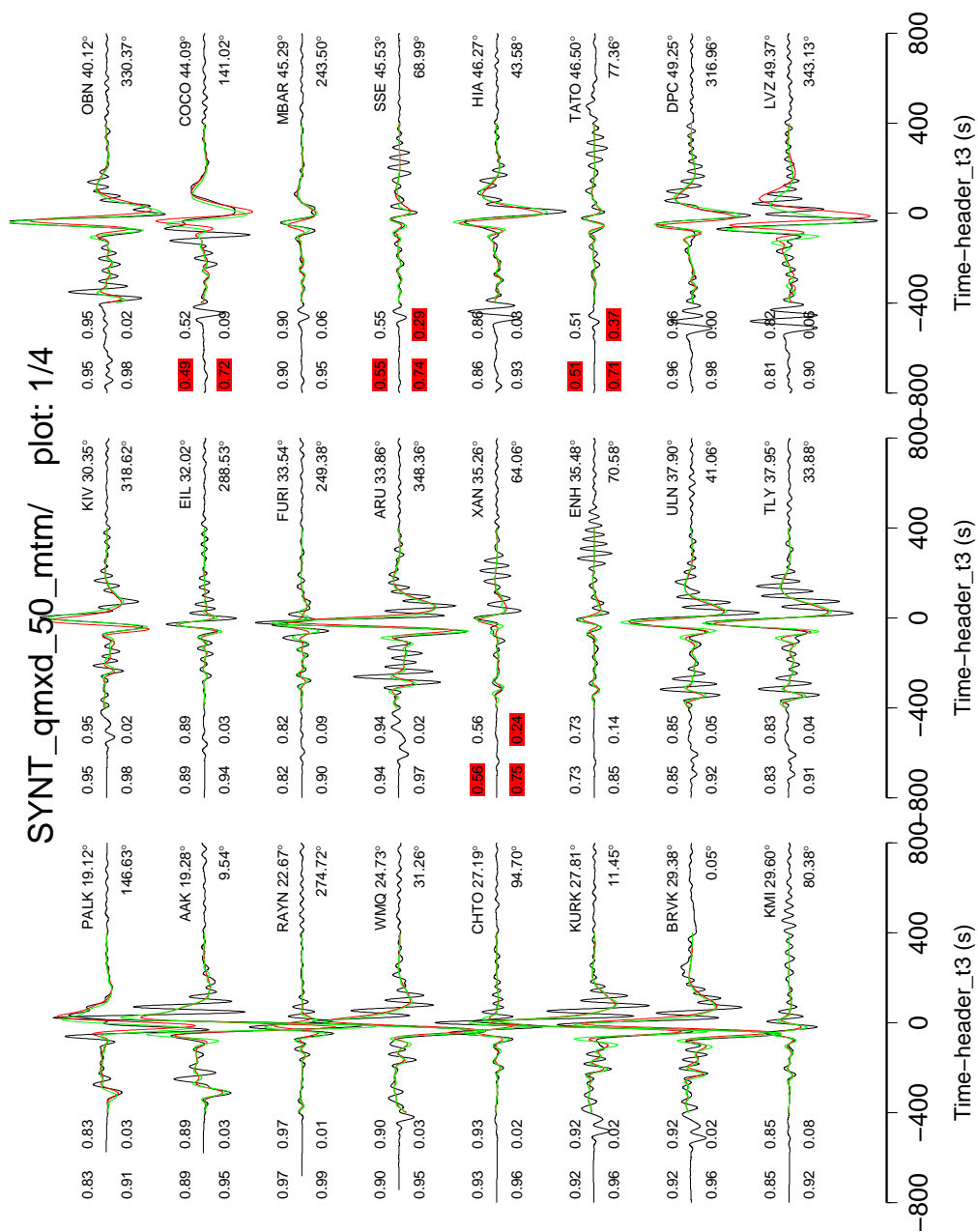


Figure 2.2: 1D synthetics (a). Data (black) are shown together with the synthetics (red) and the reconstructed synthetics (green). Data and synthetics are filtered between 50 and 500 seconds. Together with each trace we show the four different misfit estimates between the data and the reconstructed synthetic, from left to right, top to bottom: WM , CC_{max}^2 , CC_{max} , and AR . Those parameters that are outside of the cutoff values are marked red.

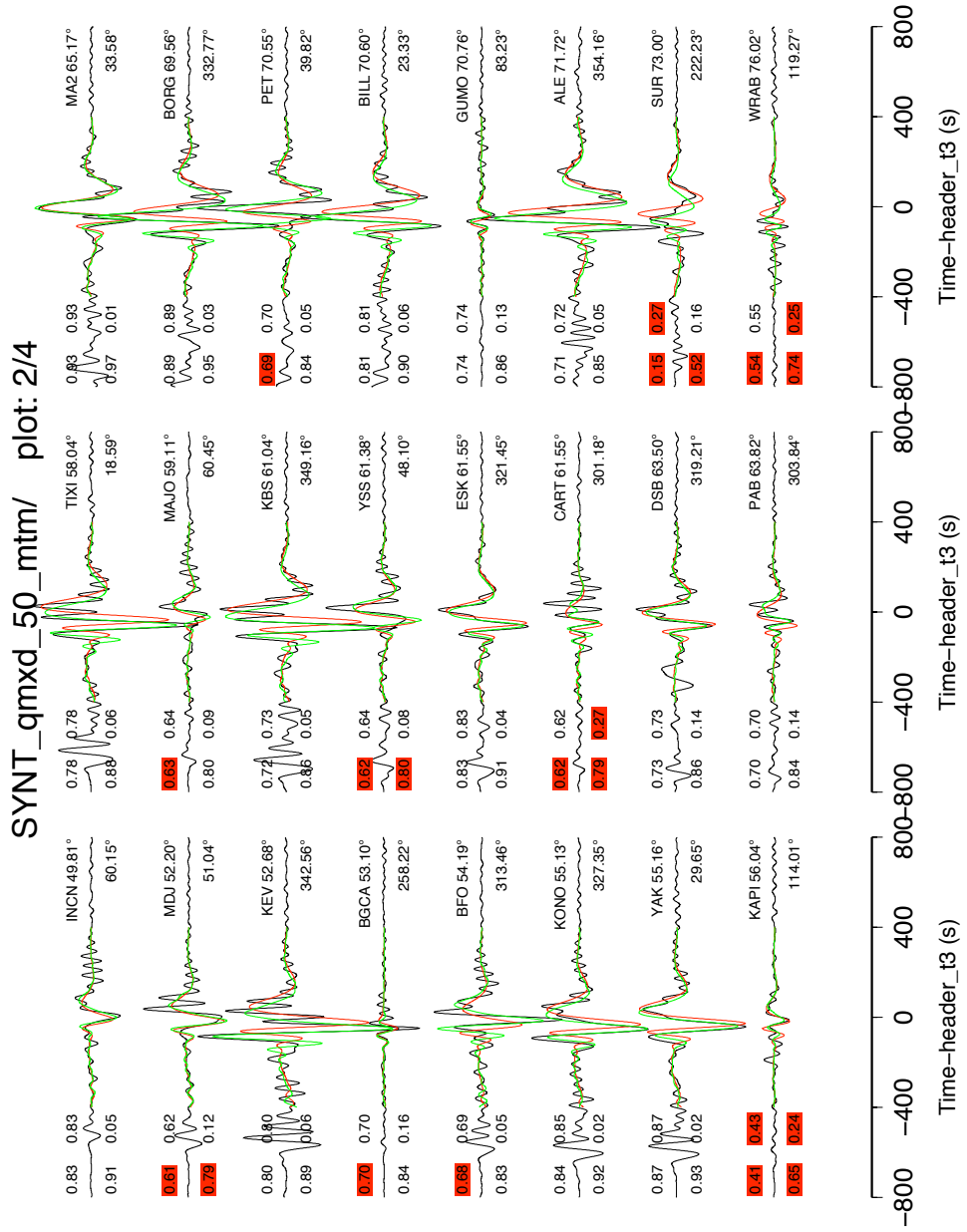


Figure 2.3: 1D synthetics (b). For description see Fig. 2.2.

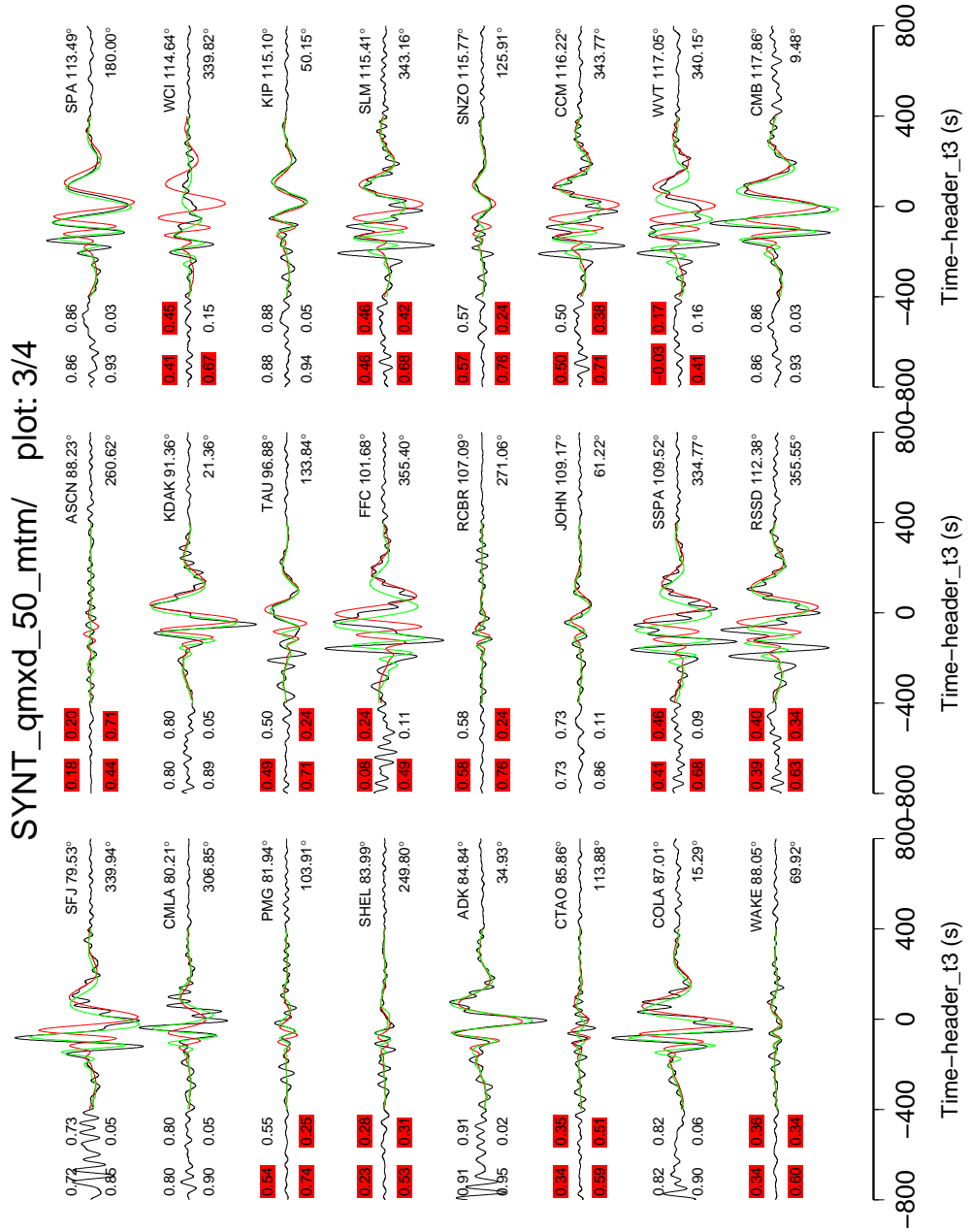


Figure 2.4: 1D synthetics (c). For description see Fig. 2.2.

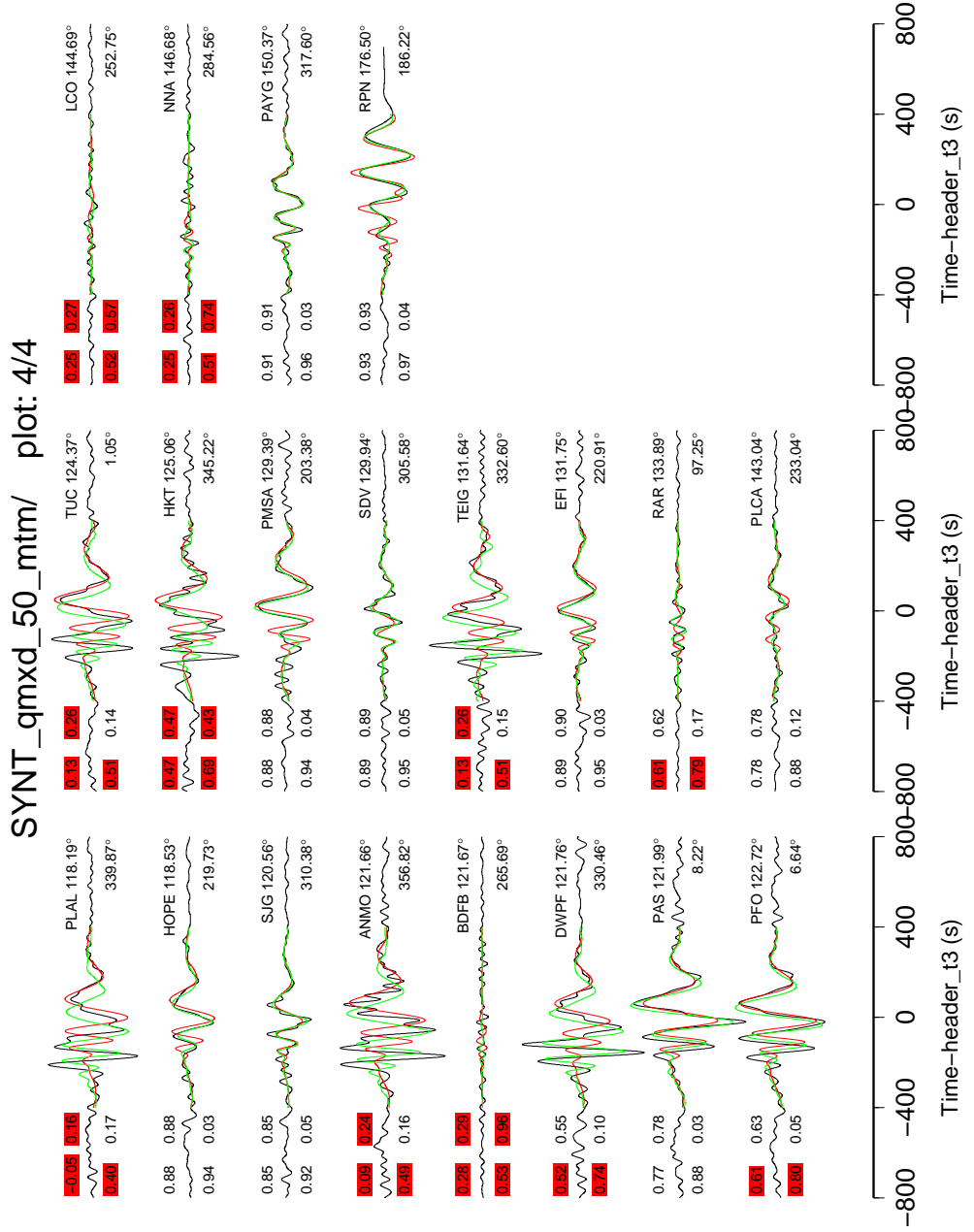


Figure 2.5: 1D synthetics (d). For description see Fig. 2.2.

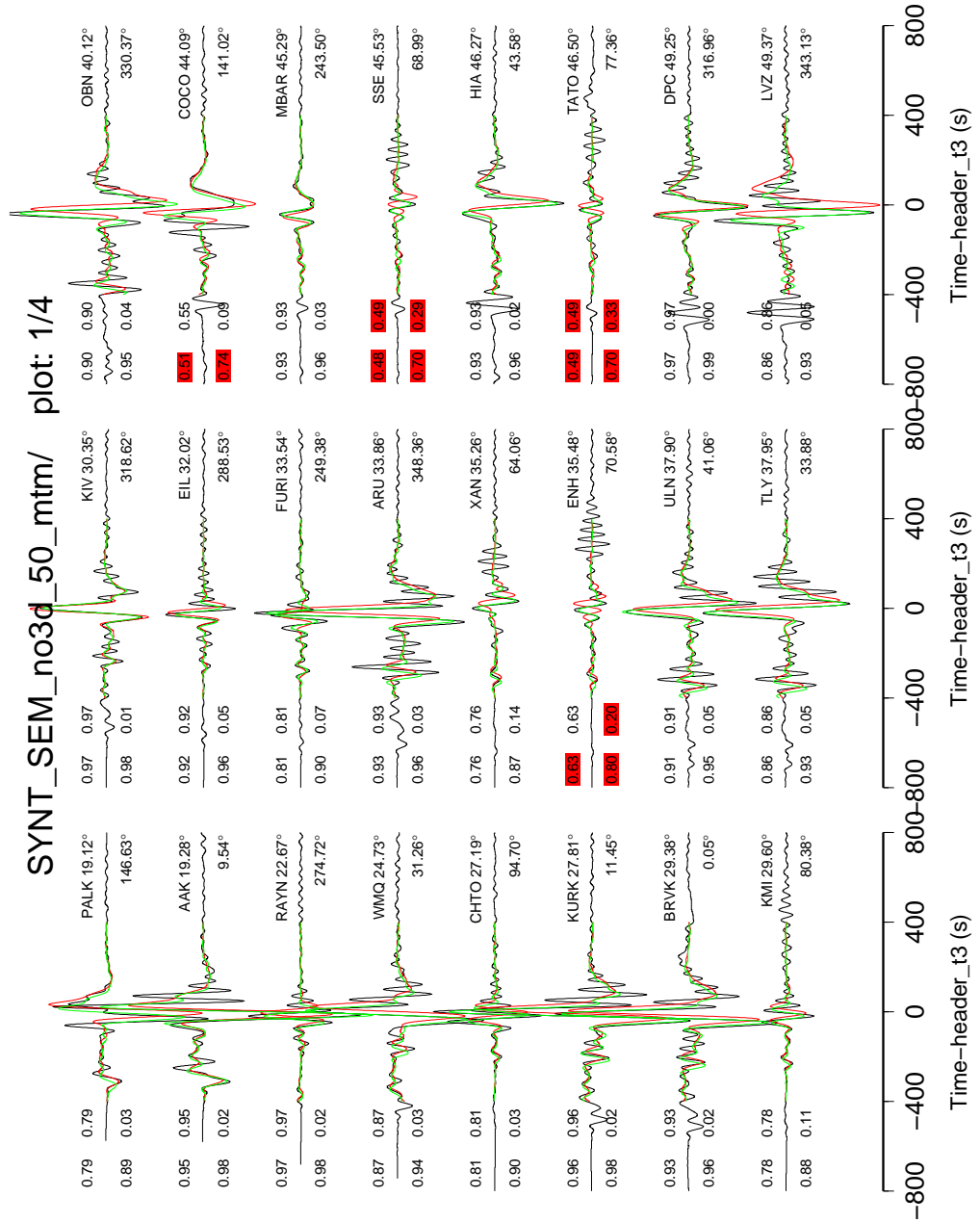


Figure 2.6: 3D crust, 1D mantle (a). For description see Fig. 2.2.

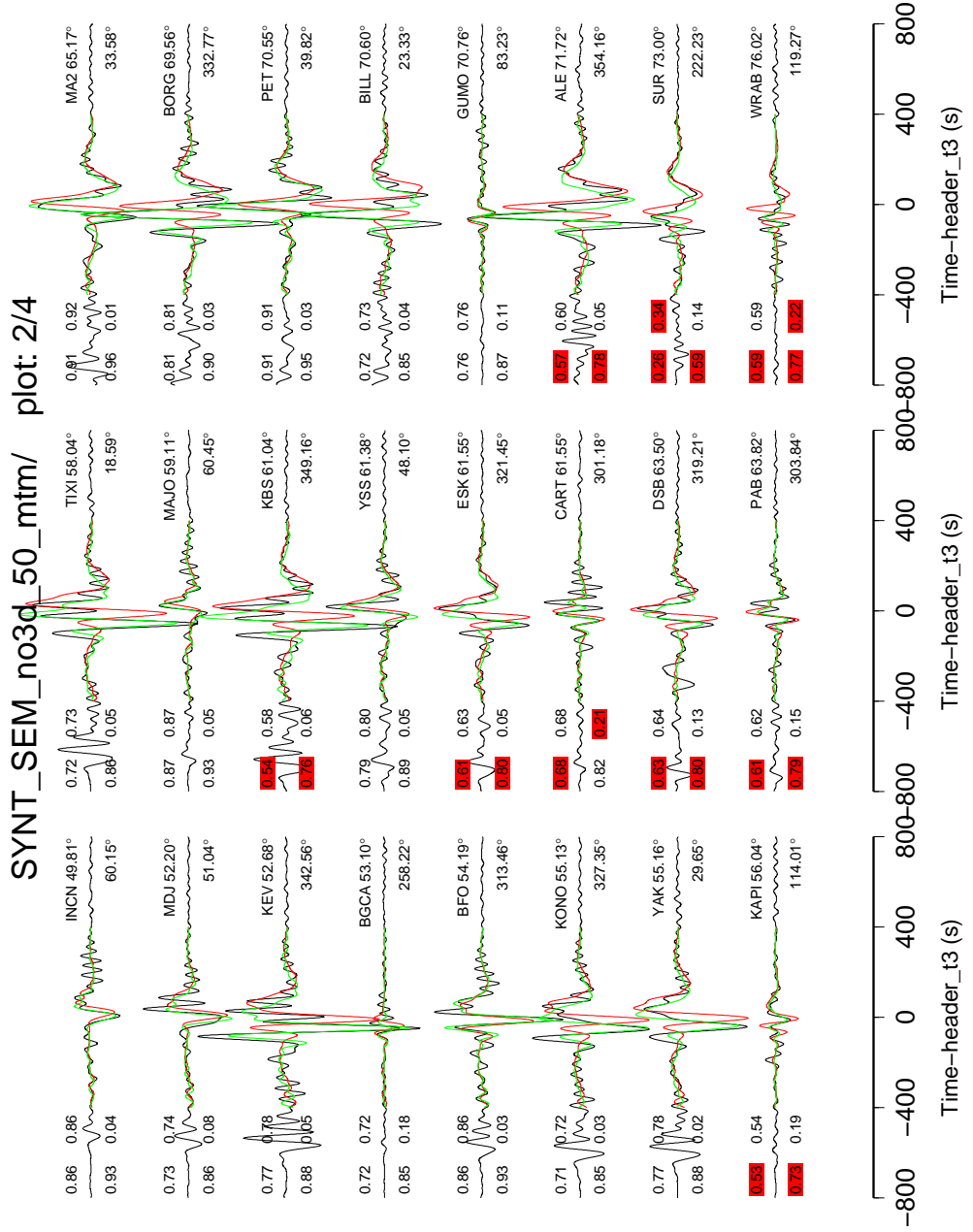


Figure 2.7: 3D crust, 1D mantle (b). For description see Fig. 2.2.

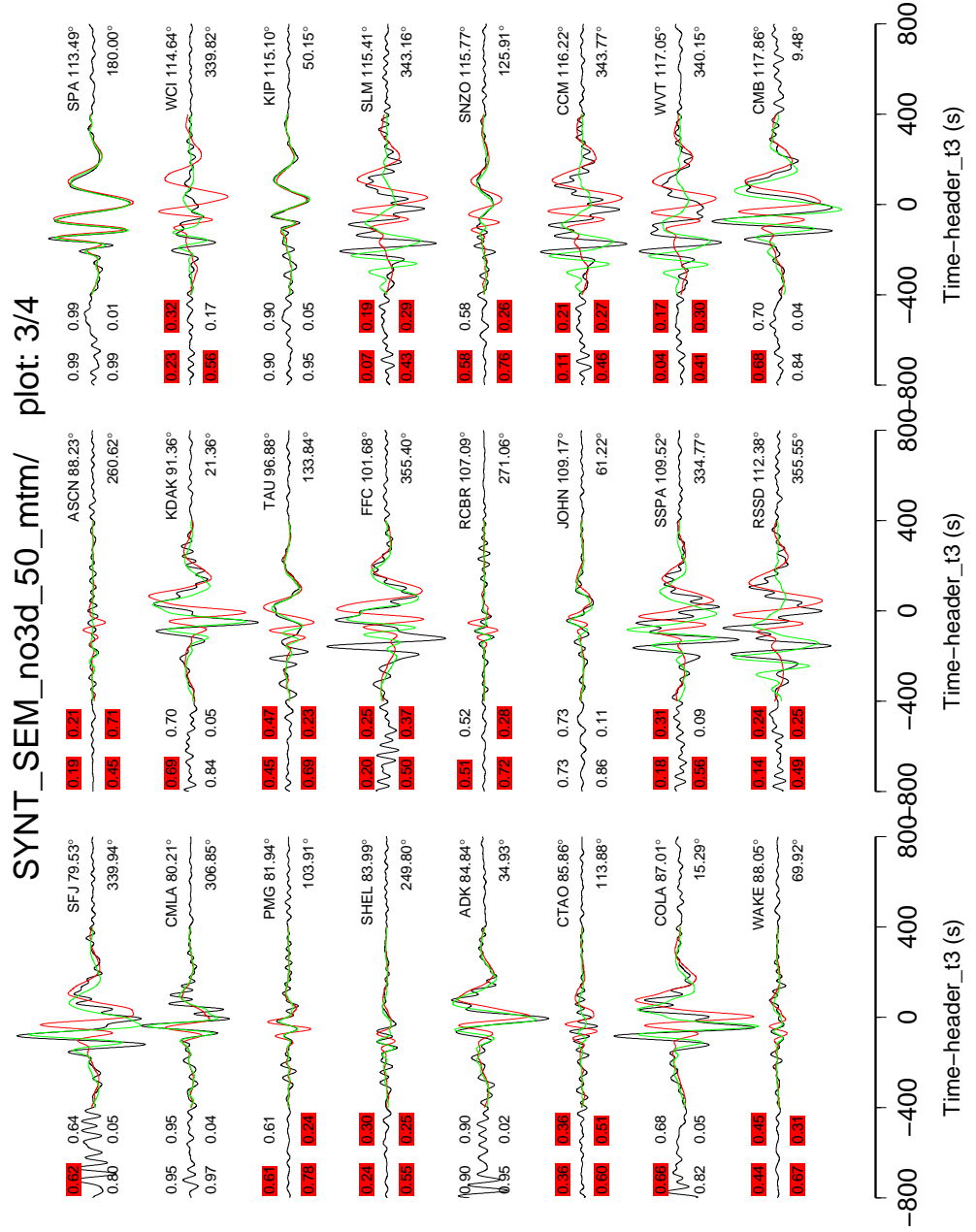


Figure 2.8: 3D crust, 1D mantle (c). For description see Fig. 2.2.

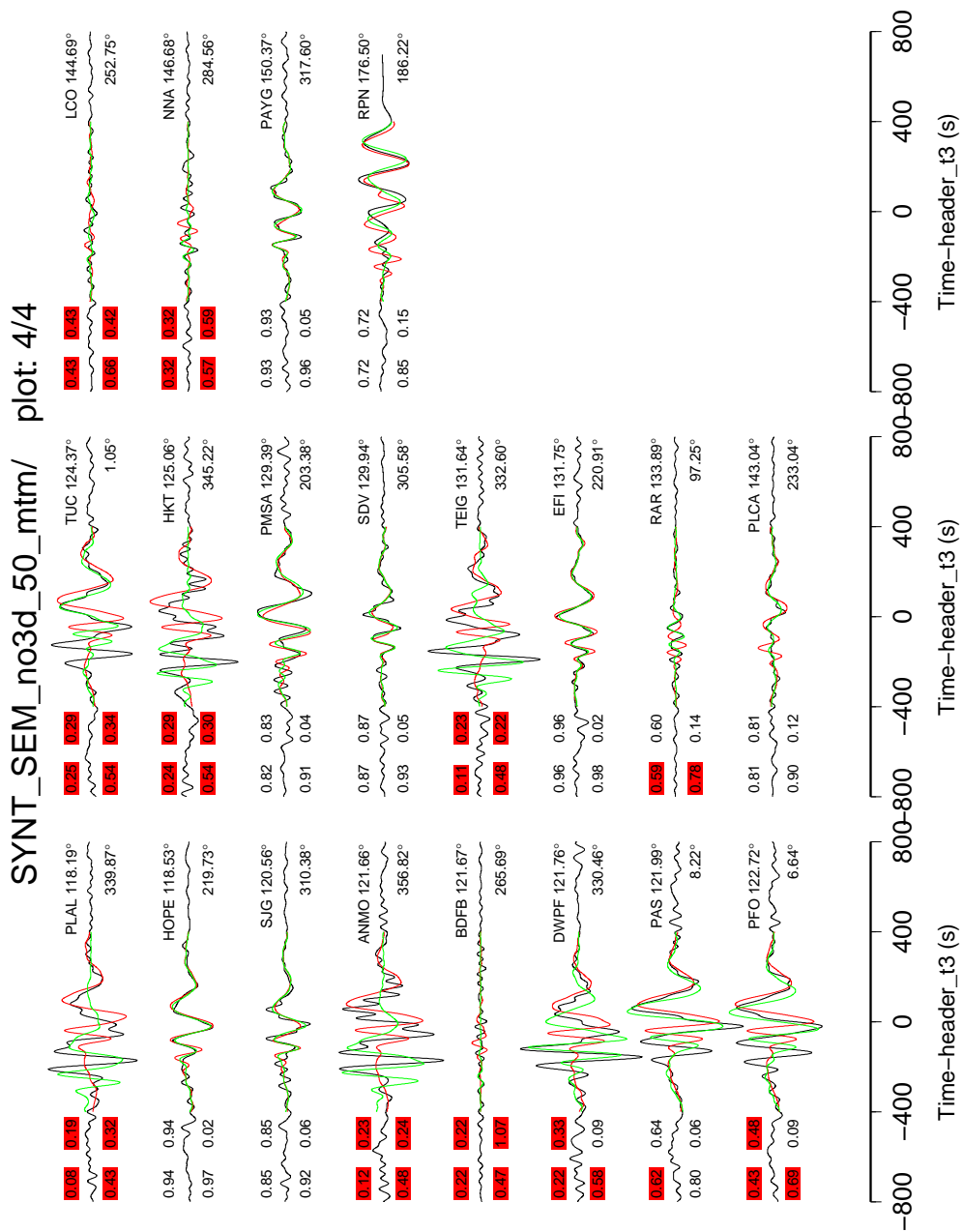


Figure 2.9: 3D crust, 1D mantle (d). For description see Fig. 2.2.

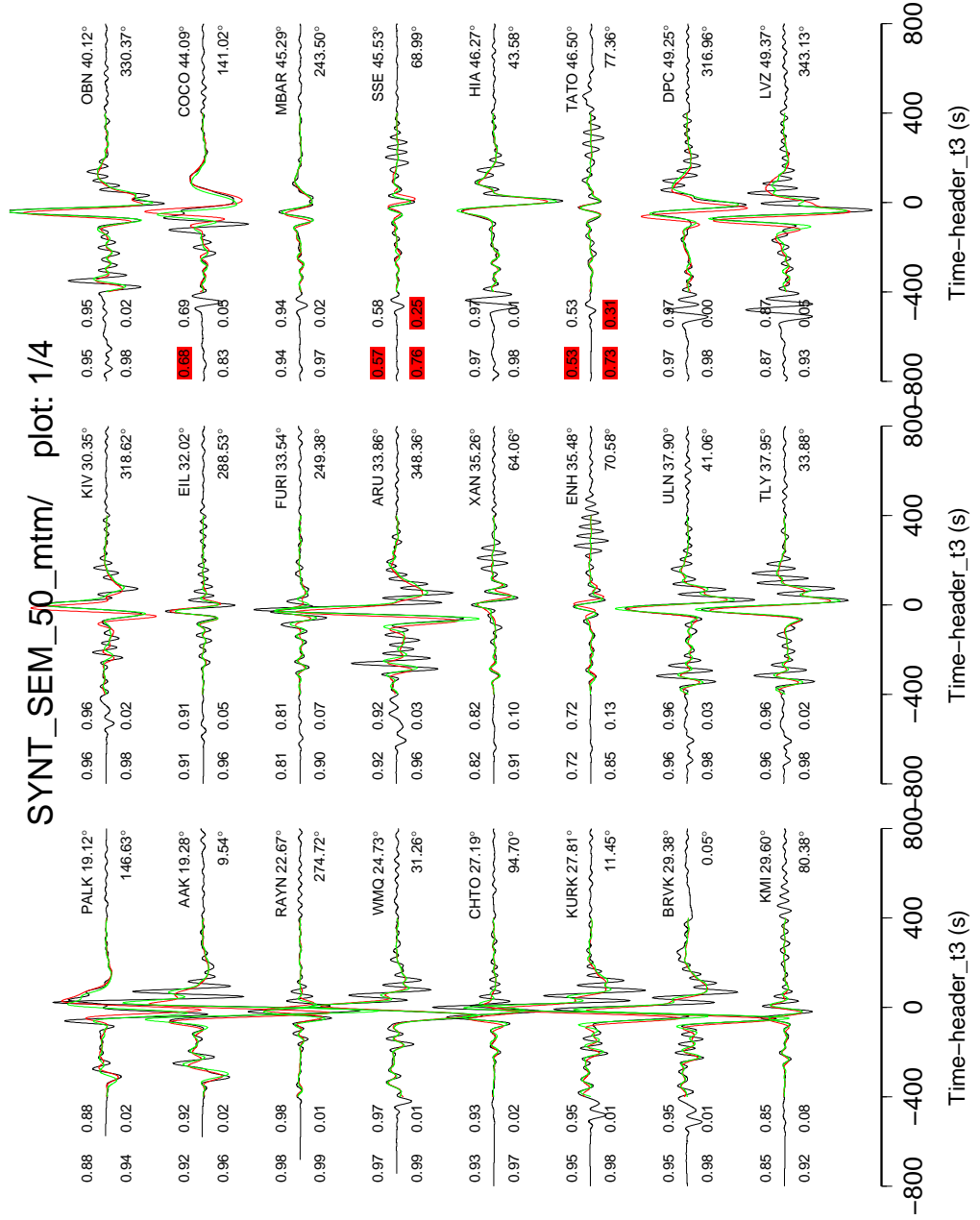


Figure 2.10: 3D crust, 3D mantle (a). For description see Fig. 2.2.

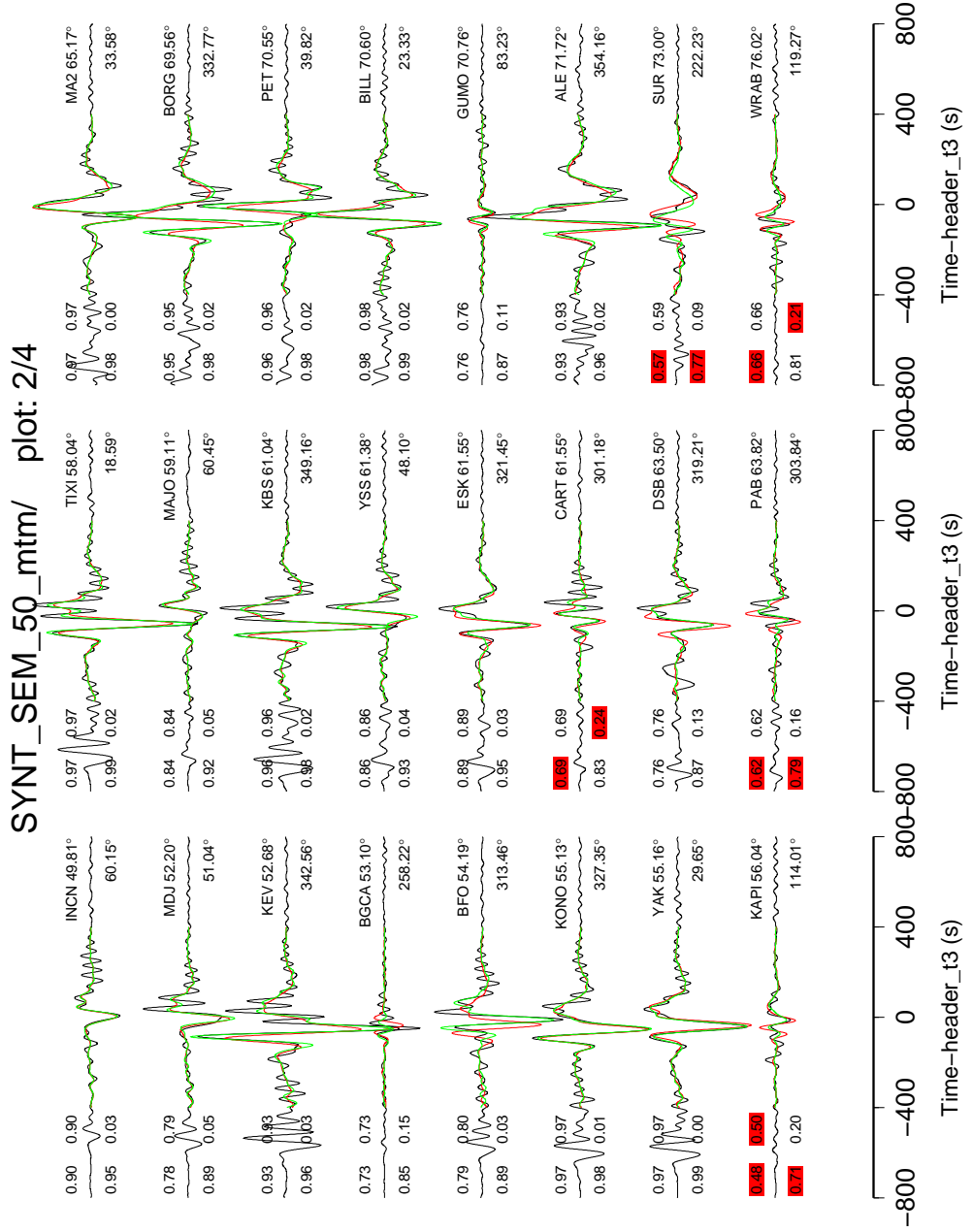


Figure 2.11: 3D crust, 3D mantle (b). For description see Fig. 2.2.

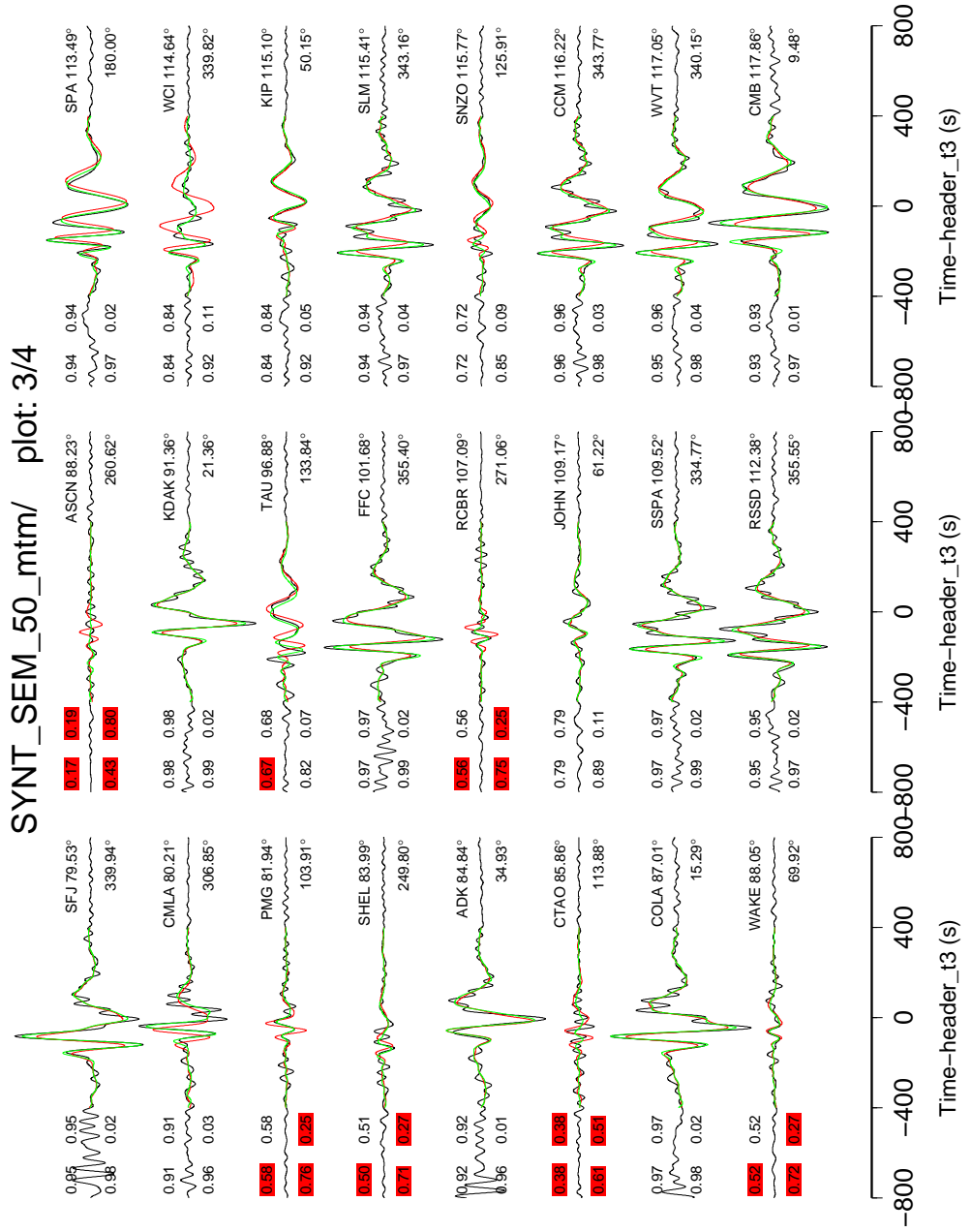


Figure 2.12: 3D crust, 3D mantle (c). For description see Fig. 2.2.

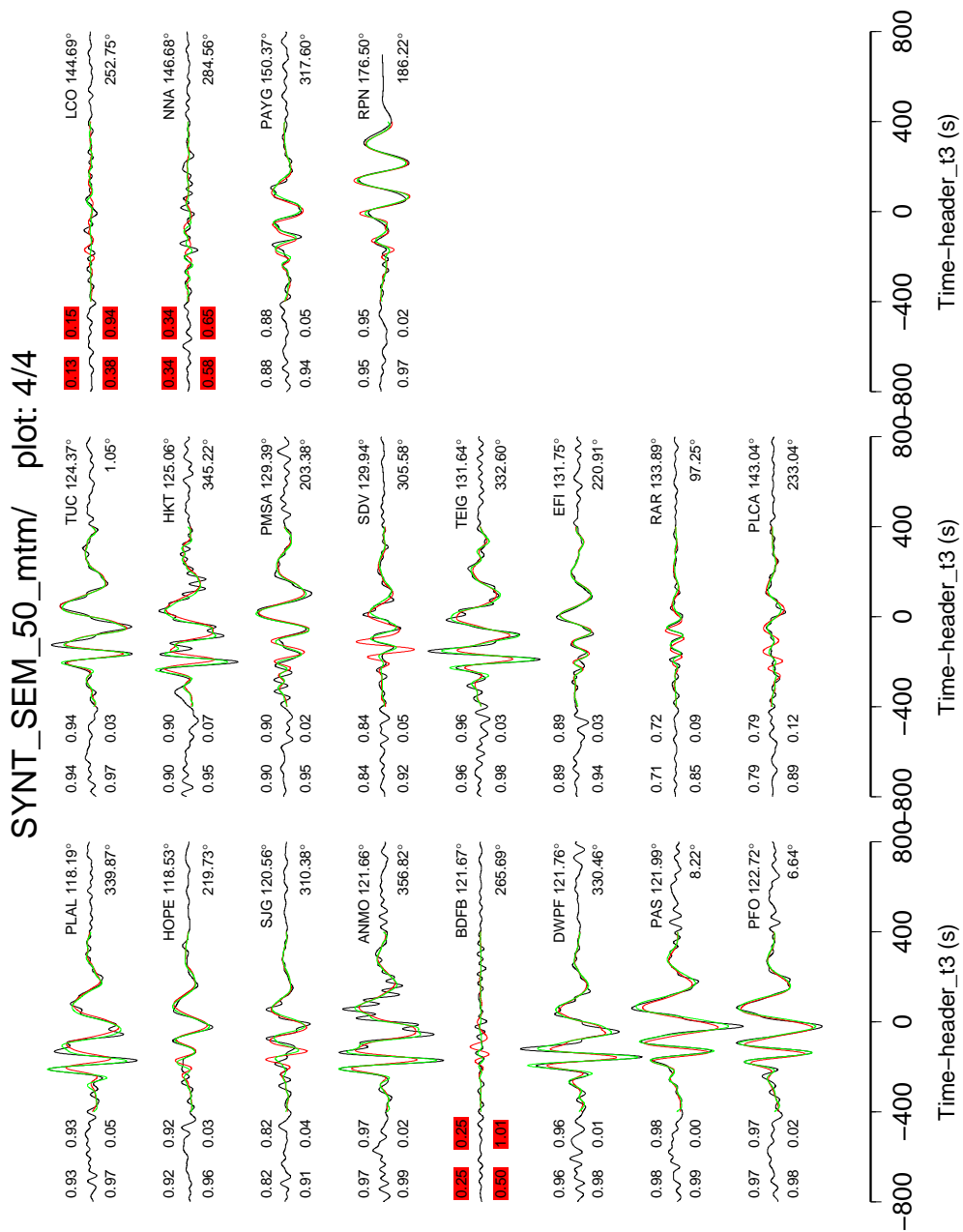


Figure 2.13: 3D crust, 3D mantle (d). For description see Fig. 2.2.

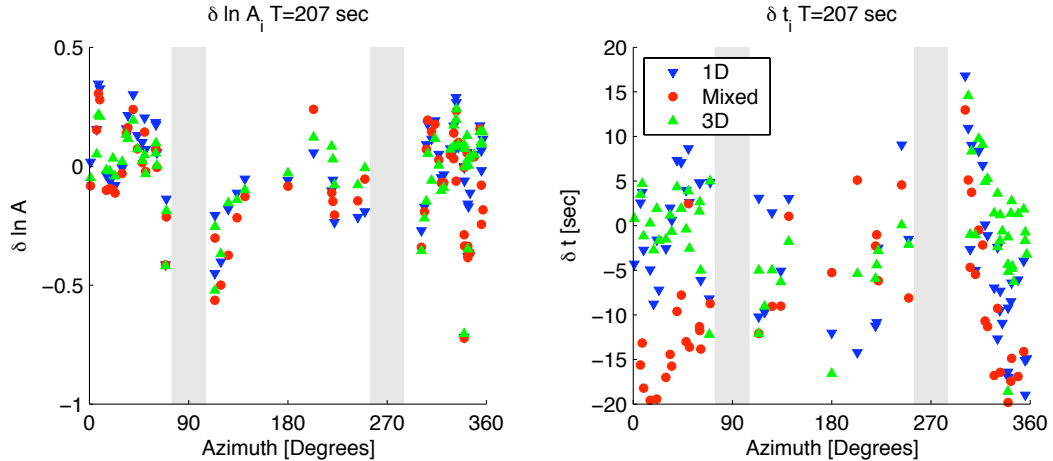


Figure 2.14: Multitaper measurements of time shift $\delta\tau$, and amplitude $\delta \ln A$, for all stations between distances of 40° and 140° , for a period of 207 seconds. The nodal regions are masked out.

than observed, the one with 3D crust more so than the PREM model. The average time shift for the 1D model is very close to zero at all the frequencies probed. The variability in the amplitude, $\sigma^{\ln A}(f)$ is similar for all the models, with the 3D model performing somewhat better at all frequencies. The variability in time shifts, $\sigma^\tau(f)$, is the smallest for the 3D model at all periods, except at 270 seconds, ranging from around 7 seconds at periods of 270 seconds to 16 seconds at periods of 50 seconds. The model with 3D crust and 1D mantle has the largest time shifts, with similar values as the 3D model at long periods, and up to 26 seconds at periods between 50 and 100 seconds. The final misfit values when integrated over the frequency range from 0 to 0.02 Hz are shown in table 2.1, and in table 2.2 for the frequency range from 0 to 0.01 Hz.

Table 2.1: Average amplitude anomalies and time shifts for the three models, averaged over all stations and frequencies from 0 to 0.02 Hz

Model	$\overline{\delta \ln A}$	$\overline{\delta \tau}$	$\sigma^{\ln A}$	σ^τ
1D mantle + 1D crust	0.01	-11.21	0.43	20.61
1D mantle + 3D crust	-0.02	-16.03	0.42	22.52
3D mantle + 3D crust	0.04	-1.00	0.38	11.30

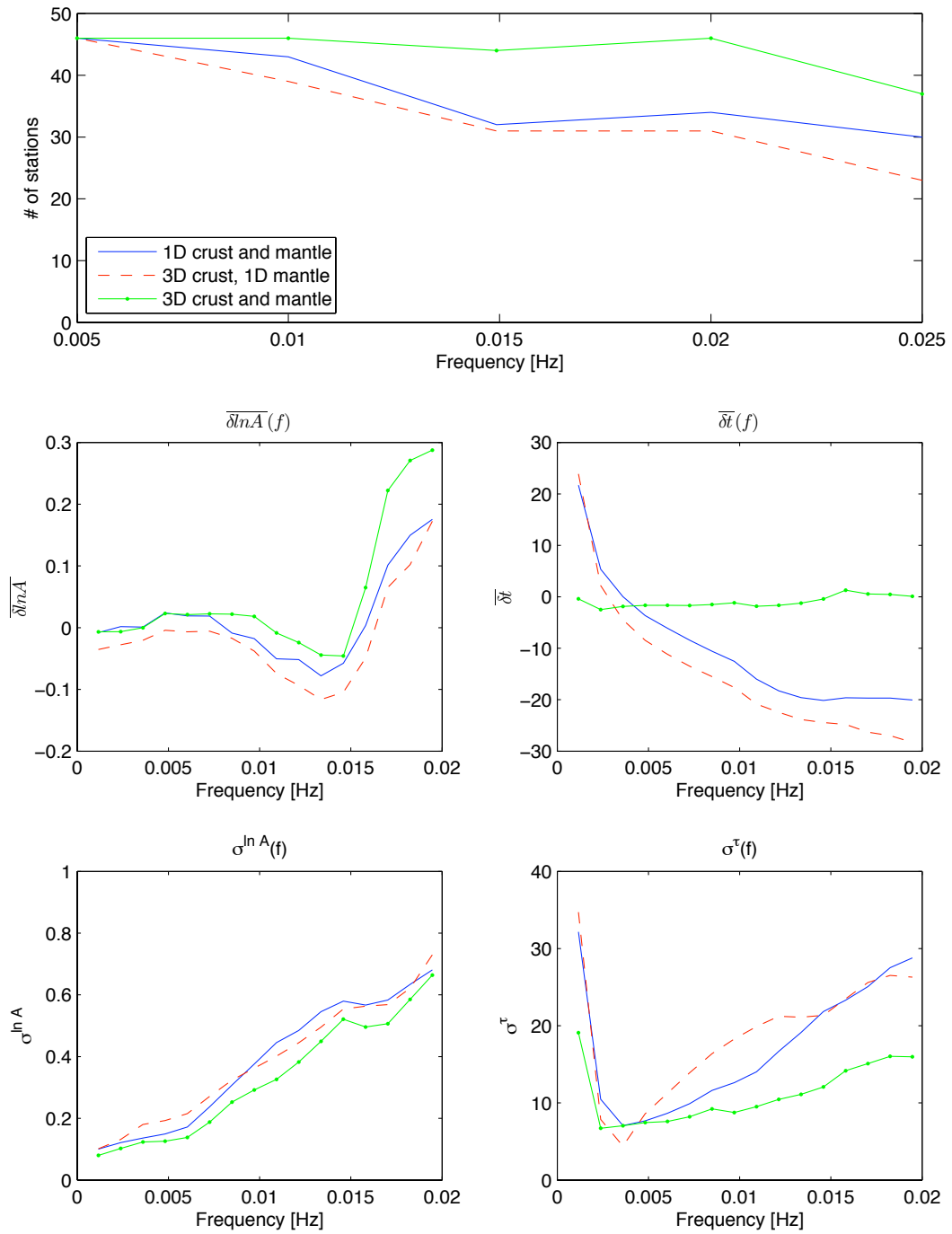


Figure 2.15: (a) Number of records that can be adequately reproduced when applying the multi-taper transfer function to the synthetic as a function of frequency for three different Earth models. (b) Average amplitude anomalies as a function of frequency for three different Earth models. (c) Average time-shifts as a function of frequency for three different Earth models. (e) Variation of amplitude anomalies around the mean as a function of frequency. (f) Variation of time shifts around the mean as a function of frequency.

Table 2.2: Average amplitude anomalies and time shifts for the three models, averaged over all stations and frequencies from 0 to 0.01 Hz

Model	$\overline{\delta \ln A}$	$\overline{\delta \tau}$	$\sigma^{\ln A}$	σ^τ
1D mantle + 1D crust	-0.02	-3.442	0.19	14.04
1D mantle + 3D crust	-0.05	-8.67	0.22	15.62
3D mantle + 3D crust	-0.01	-2.13	0.15	8.38

2.5 Discussion

The degradation of fit when adding the 3D crustal model to PREM (model 2) is observed for many stations. It seems somewhat counterintuitive that the waveforms are not as well fit when we use a model that includes 3D variations in the crust compared to when we use one that does not. This is because the average velocity in the upper layers of the Earth is well approximated by PREM. Removing the top of PREM and replacing it with a more realistic 3D crustal model without changing the mantle disturbs the balance between the crust and upper mantle velocities. By doing so we recover the observed dispersion of the surface waves, which is critically dependent on the distribution of velocities in the crust, but we change the group speed, which is more dependent on the average velocity with depth (hence the larger $\overline{\delta \tau}$). We recover both the dispersion and the arrival time when we incorporate 3D mantle model S20RTS in our simulations.

Earlier studies have shown that lateral heterogeneity can cause significant amplitude variations of long-period surface waves due to focusing and defocusing (*Lay and Kanamori, 1985*). For the paths studied here the 3D models shows smaller amplitude anomalies than the 1D model at periods of 200 seconds and shorter, indicating that they better reproduce the observed focusing.

We find that it is not sufficient to use a 3D crustal model in combination with a 1D mantle model to compute accurate synthetics for surface waves on a global scale at periods between 40 and 200 s. In fact, some stations show better fits for a strictly 1D model. To match the data, the 3D structure of both crust and mantle has to be incorporated. The good agreement between data and synthetics at periods of 50 s and longer indicates that, at least for these paths, the effects of 3D heterogeneity on the waveforms is mostly accounted for by the 3D model. In subsequent chapters we will repeatedly use the frequency dependent measurements introduced here.

Chapter 3

The 2001 Kunlun, China earthquake

3.1 Introduction

Macroscopic earthquake source parameters provide insight into the processes occurring on the fault plane during rupture. The dynamics of earthquake faulting are controlled by how much energy is dissipated as fracture energy during rupture propagation. The direct determination of fracture energy with seismological methods is extremely difficult. However, theories in fracture mechanics (*Mott*, 1948; *Kostrov*, 1966; *Eshelby*, 1969; *Freund*, 1972) show that the fracture energy can be estimated from the rupture speed. In general, a fast rupture speed (e.g., comparable to, or faster than, the Rayleigh- or shear-wave speed) indicates that the fracture energy is much smaller than the radiated energy, and the earthquake is considered very “brittle.” Unfortunately, the rupture speed of earthquakes is notoriously difficult to estimate. The distribution of slip in space and time on the fault plane is frequently determined from short-period body waves. Due to limited resolution, and trade-offs, the determination is easiest for long and narrow faults, generally long strike-slip faults. However, for most global stations, the take-off angle is close to vertical which is nodal for strike slip events. As a result the models can be sensitive to small changes in rake angle, as well as scattering near the source, and the inversions can produce models that show similar fit synthetics to the data, despite having different slip distributions.

Here we determine the rupture speed of the 2001 Kunlun, China earthquake, which ruptured unilaterally along a 400 km segment of the left-lateral strike-slip Kunlun fault (*Lin et al.*, 2002; *van der Woerd et al.*, 2002; *Xu et al.*, 2002). The event occurred in a remote and

mountainous region making direct observations of the rupture difficult. However, the large moment of the event and the separation between the epicenter (reported by the National Earthquake Information Center, NEIC) and the best-fit point source, as determined by the Harvard CMT project (*Ekström et al.*, 2003), indicated that the rupture was unusually long. Furthermore, the distribution of aftershocks extended over 350 km east of the epicenter (as reported by the NEIC). This length of rupture was supported by observations of surface breaks (*Lin et al.*, 2002; *Xu et al.*, 2002; *van der Woerd et al.*, 2002) and early body-wave models (*Lin et al.*, 2003). Subsequently several studies have focused on different aspects of the earthquake, including the surface break (*Lin et al.*, 2003; *Klinger et al.*, 2005; *Fu et al.*, 2005; *King et al.*, 2005; *Xu et al.*, 2006), the slip on the fault derived from optical images (*Klinger et al.*, 2006), InSAR images (*Lasserre et al.*, 2005) and seismology (*Lin et al.*, 2003; *Bouchon and Vallée*, 2003; *Ozacar and Beck*, 2004; *Antolik et al.*, 2004; *Robinson et al.*, 2006).

In this chapter we determine finite fault slip models, based on body-wave inversions, for several different rupture speeds. We then compute synthetic surface waves using a 3D Spectral Element Method (SEM) and compare the resulting seismograms to data, obtaining an independent estimate of the quality of the models. The trade-offs are dependent on the phase speed of the phase being looked at, making it advantageous to look at waves with very different phase speeds.

3.2 Body-wave modeling

3.2.1 Data

We retrieved data for the event from the IRIS data center (www.iris.edu) for most permanent global stations recording 20 sample-per-second broadband data. We use data from 26 stations at distances between 65° and 90° . The lower bound is determined by selecting only stations that do not have a PP arrival within a 120 second window after the arrival of the initial P-wave. This is assuming that the duration of rupture was less than 120 seconds. The upper bound is chosen to reduce the interference of the PcP phase, which has a high amplitude at distances larger than 90° . The P-arrivals are aligned on a predicted travel time computed for the NEIC epicentral location (90.54°E , 35.96°N). It is common practice in body-wave modeling to pick the first arrivals to align records, however, due to

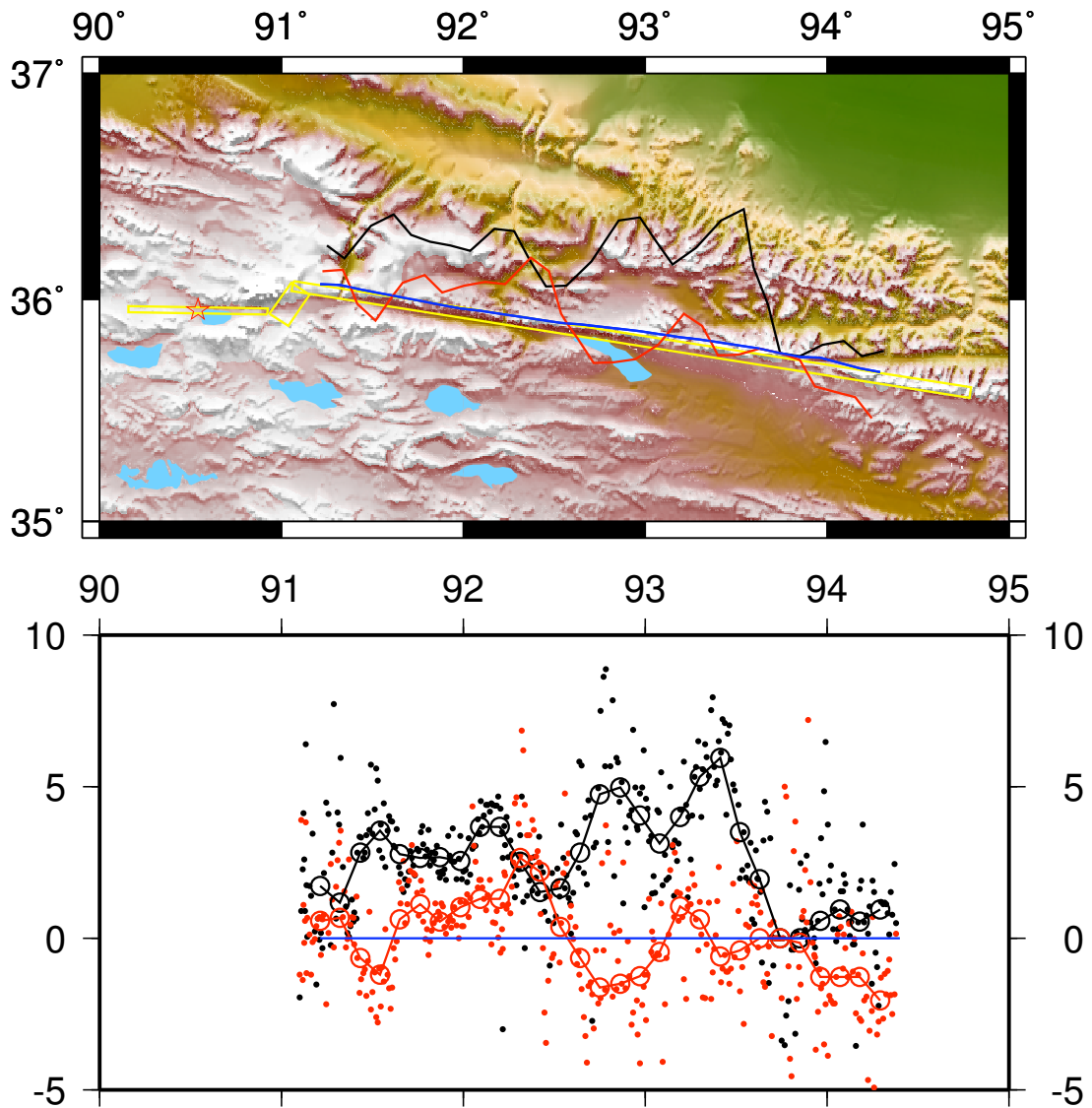


Figure 3.1: The M_w 7.9, November 11, 2001, Kunlun, China, earthquake broke a 400 km long section of the Kunlun fault. The black dots in the lower inset show left-lateral surface offset measurements from *Klinger et al.* (2006). The red dots show the horizontal, fault normal, component of motion (negative sign indicates thrust motion) from the same study. The corresponding solid lines show our smoothed versions of the surface slips that are used as a constraint to the body-wave inversions. The yellow lines indicate the surface projections of the fault planes used in our modeling.

the emergent nature of the onset of rupture for this event, the first arrival is not always clear, so we choose not to do so. We removed the instrument response from the records using deconvolution to obtain ground displacement and then band-pass filtered between 1.6 and 120 seconds. The records and their geographical distribution are shown in Fig. 3.2.



Figure 3.2: Data used for body-wave inversions. We use only data recorded at distances between 65° and 90° . Note the large amplitudes in the Pacific region, demonstrating the eastward directivity of rupture.

3.2.2 Inversion

We invert the data for magnitude, direction, timing and duration of slip, on each subfault of a prescribed fault plane. We constrain the slip of the top row of subfaults to be equal to

the observed surface slip, where available, and constrain the ends to have a small slip. The subfaults are 10 km along the surface, and 2 km in depth. We use a simulated annealing algorithm to fit the wavelet transform of the seismograms (*Ji et al.*, 2002). We impose both a moment constraint and a smoothness constraint, as well as a constraint on the rupture speed. There are many input parameters in this type of inversion, and the outcome can be quite dependent on the parameters chosen. Perhaps the most difficult parameter to choose is the geometry of the prescribed fault plane. However, as previous seismological studies have focused on determining the fault geometry (*Ozacar and Beck*, 2004; *Antolik et al.*, 2004; *Robinson et al.*, 2006), we wish not to repeat that exercise, but rather to use the values found in previous studies, and focus on obtaining a more robust estimate of the rupture speed.

Two seismological studies of this event use a one-fault parameterization (*Bouchon and Vallée*, 2003; *Lin et al.*, 2003). Other studies, however, all point out that the first 30 seconds of the body-wave train are not well explained by a one fault-plane model, and invoke one (*Robinson et al.*, 2006) or two (*Ozacar and Beck*, 2004; *Antolik et al.*, 2004) more fault planes to match the observed records. Although the surface waves that we will be studying in the following sections of this chapter are not very sensitive to the first 30 seconds of the rupture, due to the small slip at that time, we choose to use a three fault plane solution in order to remove that as a source of discrepancy. The surface projections of the faults used in this study are shown in Fig. 3.1

The first motions of the earthquake, indicate left-lateral slip on a steep fault plane, oriented roughly east–west (*Ozacar and Beck*, 2004; *Antolik et al.*, 2004). This is consistent with the westernmost surface breaks, west of Taiyang (Sun) Lake (*Xu et al.*, 2002; *Lin et al.*, 2003; *Klinger et al.*, 2005; *Fu et al.*, 2005; *Klinger et al.*, 2006; *Xu et al.*, 2006). We choose the first segment to align with surface breaks, striking 95° and dipping 85° .

The second segment is required to fit a sharp spike in the moment rate function that clearly does not have the same source mechanism as the remaining parts of the rupture (*Antolik et al.*, 2004). The evidence for surface slip between the first and third fault segments is small, and most likely the rupture did not reach the surface. The mechanism, however, is consistent with slip on a buried normal fault coincident with an extensional graben located south of Buka Daban Feng. We use strike 34° , dip 54° and rake -145° , as obtained by *Antolik et al.* (2004).

The main segment, is chosen to align with surface breaks, striking 99° , but extending slightly further to the south than the documented surface offsets. We use a dip of 74° , consistent with the Harvard CMT and *Antolik et al.* (2004) and close to the value of 70° obtained by *Ozacar and Beck* (2004). Large fault normal motions have been measured from satellite images (*Klinger et al.*, 2006), requiring a non-vertical fault plane along at least part of the fault. We constrain the top of the model to match the observed displacements at the surface, as measured using pixel tracking of optical images (*Klinger et al.*, 2006). We use a running average window of 30 km to average their values (see Fig. 3.1).

We use a crustal model in the source location extracted from Crust 2.0 (*Bassin et al.*, 2000). The values used are shown in Table 3.1.

Table 3.1: Crustal model used in body-wave source inversions

Depth [km]	v_p [km/s]	v_s [km/s]	ρ [kg/cm ³]
0–21	6.0	3.5	2.70
22–43	6.4	3.7	2.85
43–65	7.1	3.9	3.10
65–	8.0	4.6	3.45

3.2.3 Body-wave inversion results

We perform 9 inversions, each for fixed rupture speeds of $v_r = \{2.5, 3.0, 3.2, 3.4, 3.5, 3.6, 3.8, 4.0, 4.5\}$ km/s respectively, covering the reasonable range as determined by dividing the rough estimates of the length of rupture, 400–450 km, by the duration, 120 seconds. If a small moment constraint is applied, the moment becomes highly dependent on the rupture speed. This is in part an artifact, because if the rupture speed is very small, it will take a long time for the rupture to reach the end of the fault. The latter part of the rupture, especially after 120 seconds, is not well constrained by the seismograms, so spurious slip can be added after that time, without significant impact on the fit. The moment rate, though, is quite well constrained by the seismograms. The moment rate changes very little with rupture speed. The main difference is the timing of the end of the rupture, because that is controlled by the time when the rupture reaches the end of the fault. The moment goes from a value of $10.2 * 10^{20}$ Nm for a rupture speed of 2.5 km/s to a value of $4.7 * 10^{20}$ Nm for a rupture speed of 4.5 km/s. The waveform misfit function becomes close to flat for a range of rupture

speeds between 3.2 and 3.6 km/s (Fig. 3.7). As is to be expected, the surface waves are very sensitive to the moment, and, as will be shown in a later section, they clearly rule out models with very large or very small moments. The body waves, on the other hand, are not as sensitive to the moment, and we therefore constrain the moment of each of the inversions to a fixed value. We first constrain it to the value given by the Harvard moment tensor, $5.9 * 10^{20}$ Nm. This, however, turns out to be too low to match the surface waves (see section 3.3), and we finally constrain the moment to $6.75 * 10^{20}$ Nm which is consistent with the surface waves. The slip distributions for those inversions are shown in Figs. 3.3–3.4. The waveform fits are shown in Fig. 3.6–(b).

There are several noticeable features in the models. First, as the rupture speed increases, the largest slip patch moves further away from the epicenter. This is not surprising, as the strongest constraint from seismograms is on the timing of an event, resulting in a strong trade-off between rupture velocity and the location of the main slip patch. Another noteworthy feature is the continuity between slip at the surface and at depth. For the models with the smallest rupture speeds, the surface slip between 300 and 350 km is confined only to the top 2–4 km. This is clearly an artifact of the fault being too long compared to the duration of the rupture. Also, when the rupture speed gets very high, the rupture front reaches the end of the fault before the end of the prescribed rupture duration, 120 seconds. Thus, in a way, by constraining the slip at the surface, the length of the rupture, and the rupture duration, we are constraining the rupture velocity to roughly a value between 3 and 4 km/s. The duration of rupture is estimated to be around 120 seconds by previous studies.

The waveform misfit as a function of rupture speed is shown in Fig. 3.7 for the three sets of models. The unconstrained models have a slightly lower misfit than the constrained ones, and the higher moment models perform better at low rupture speeds, than the ones constrained to $M_0 = 5.9 * 10^{20}$ Nm. The minima for all suits of models are at 3.6 km/s, although the models rupture speeds between 3.2 and 3.8 km/s have similar misfits.

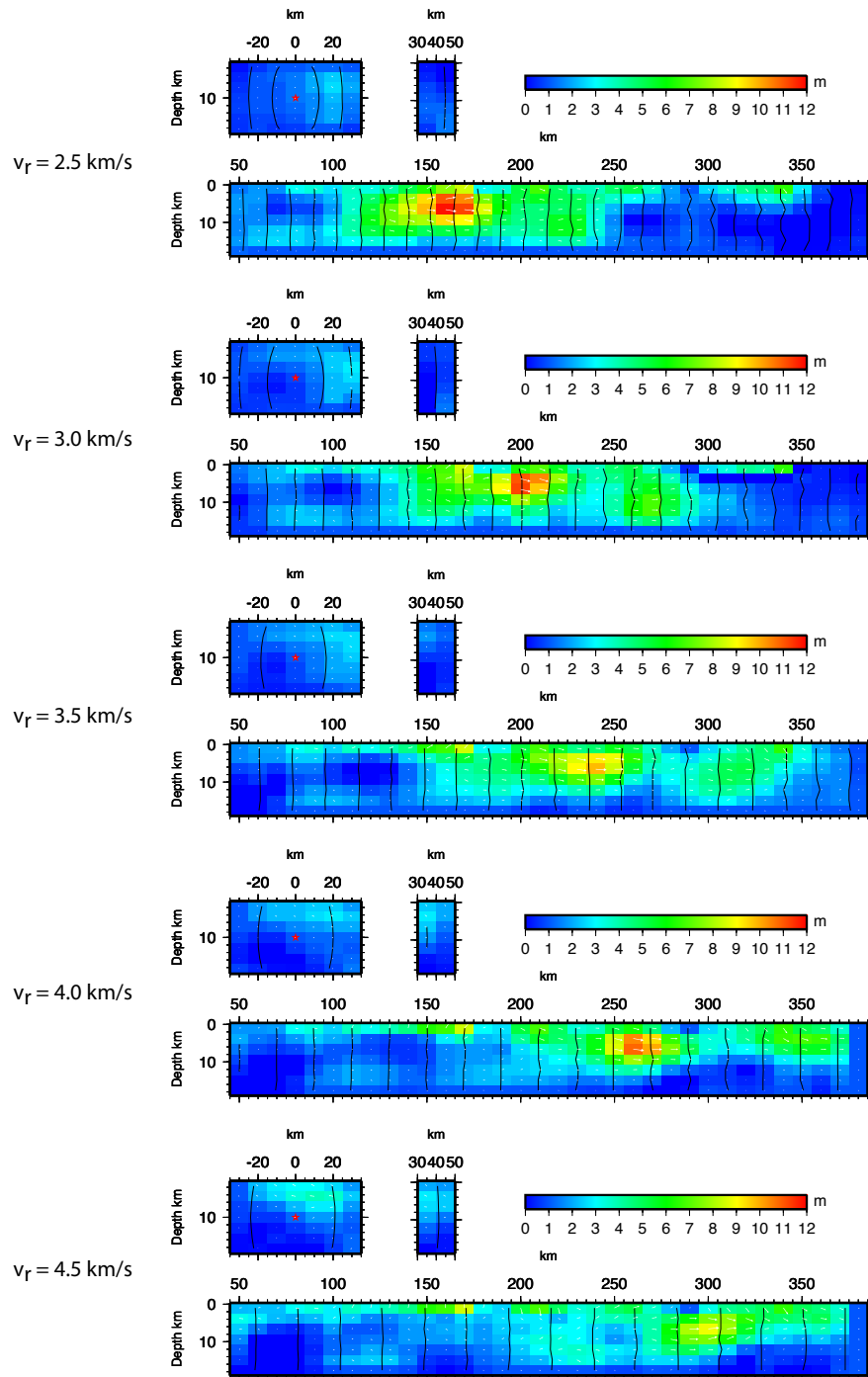


Figure 3.3: Slip distributions obtained with fixed rupture speeds and the moment constrained to values obtained by surface waves.

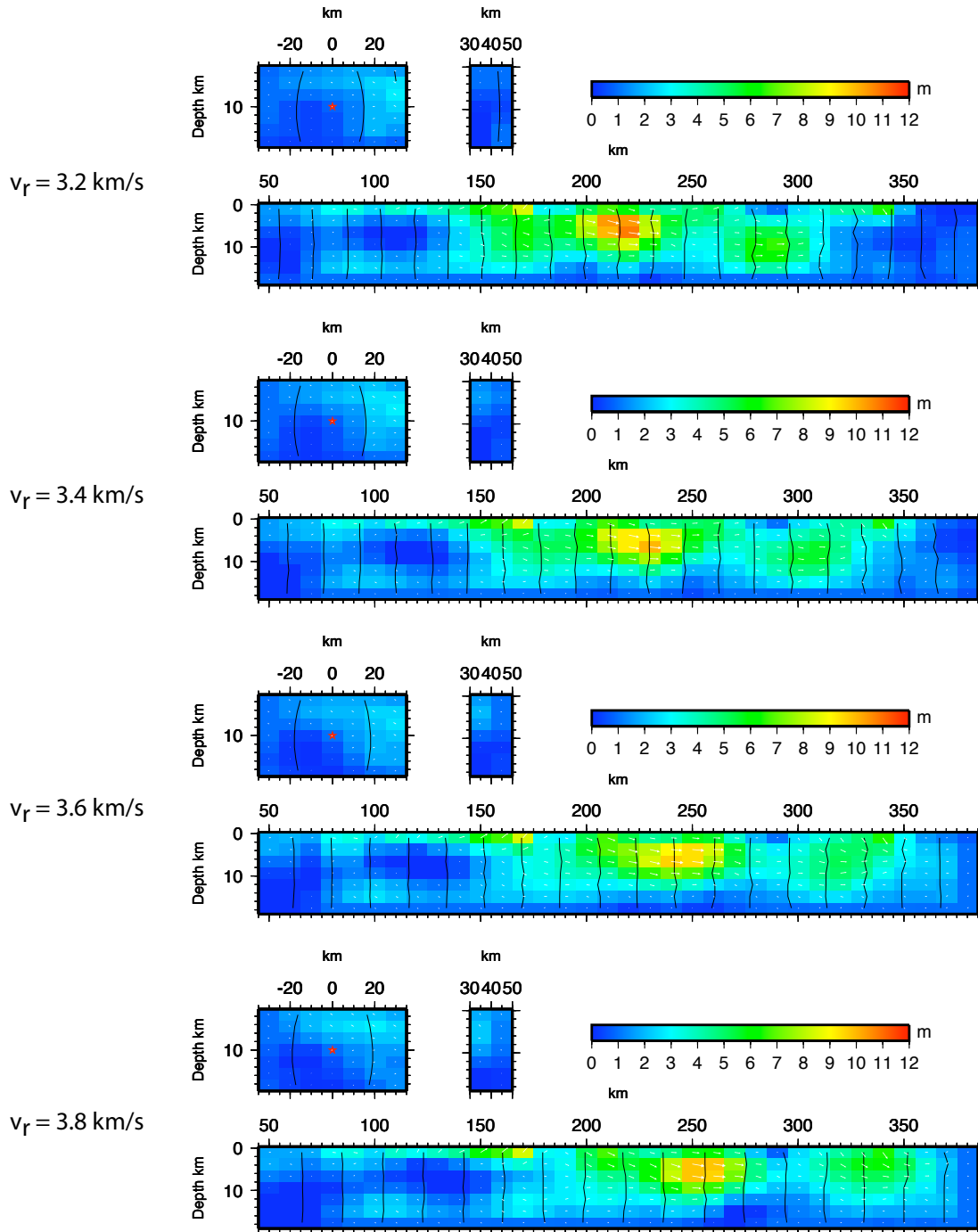


Figure 3.4: Slip distributions obtained with fixed rupture speeds and the moment constrained to values obtained from surface waves.

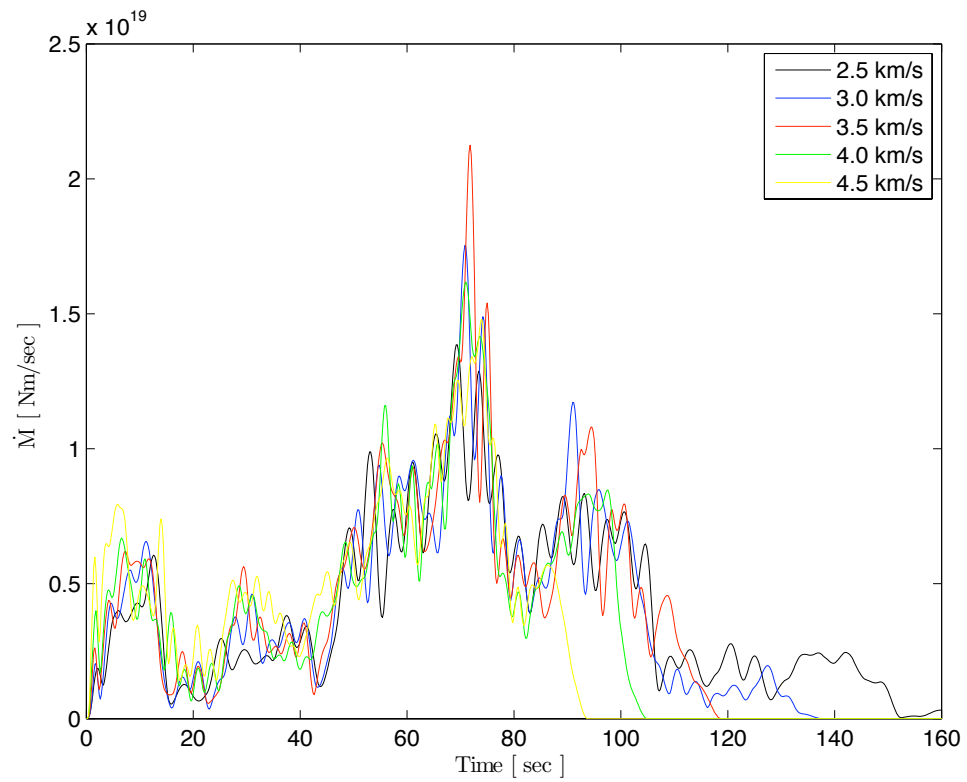
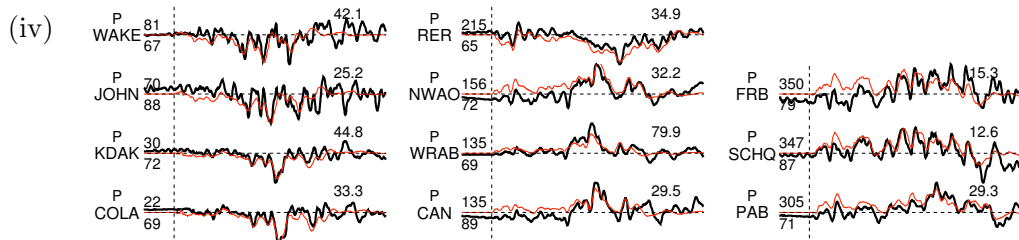
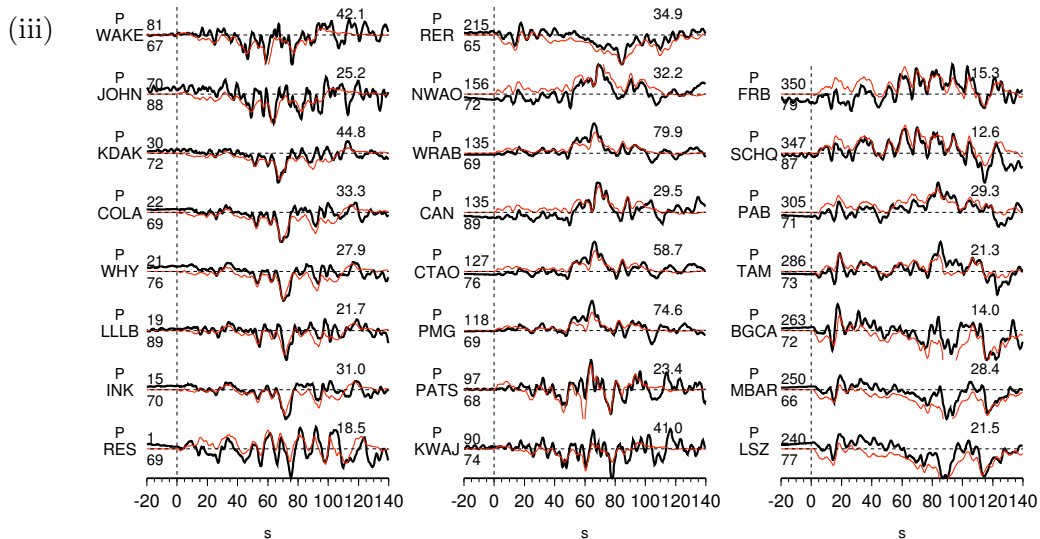
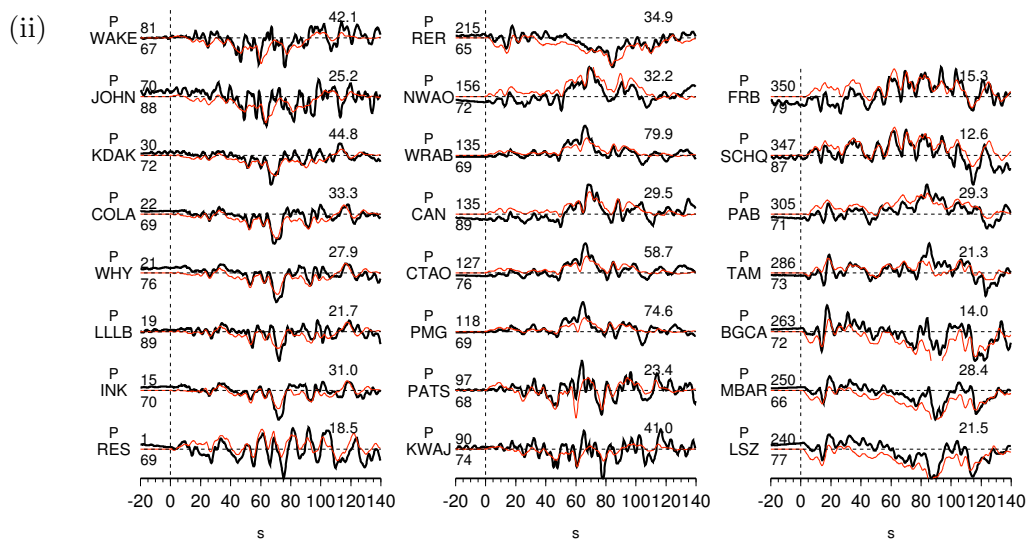
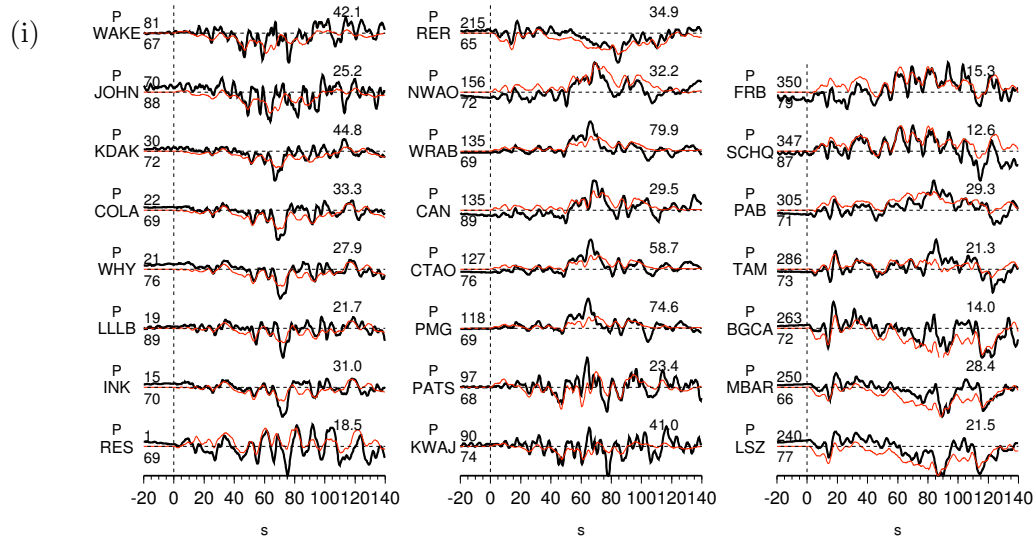


Figure 3.5: Moment-rate functions for models constrained to a moment of $M_0 = 6.75 \times 10^{20}$ Nm. Notice the similarity between the functions, except for the abrupt end of the fastest models. This is caused by the rupture reaching the end of the fault too early, thus being unable to match the end of the seismograms.



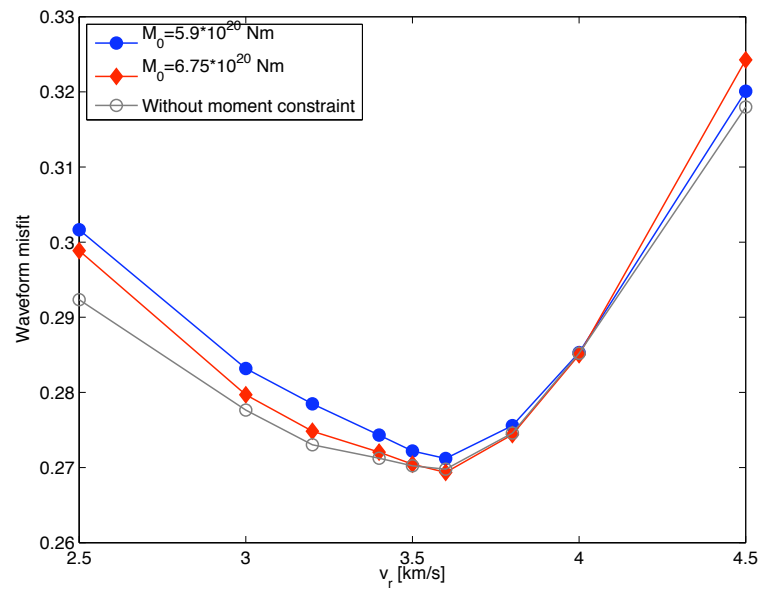


Figure 3.7: Waveform misfit as a function of rupture speed.

3.3 Surface-wave analysis

The body-wave analysis yielded a “best fit model,” defined as the model that produced waveforms that were most similar to the observed waveforms (had the smallest waveform misfit). However, as there is noise in the data (for example created by small changes in rake angles or scattering near the source), it is not a given that the model that produces the best fits is the one closest to the true slip distribution. As an independent evaluation we now compute surface waves for the slip distributions obtained in the previous section, and compare the resulting synthetic seismograms to observed surface-wave data.

3.3.1 Data and measurements

As in the previous chapter of this thesis, we use data for the event from the IRIS data center (www.iris.edu) for most permanent global stations recording 1 sample-per-second broadband data. We removed the instrument response from the records using deconvolution to obtain ground displacement. We compute synthetic waveforms, using a spectral element method (SEM), for 3D Earth models (*Komatitsch and Tromp, 2002a; 2002b*). We use a 3D Earth model that combines mantle model S20RTS (*Ritsema et al., 1999*) and crustal model Crust2.0 (*Bassin et al., 2000*). The 3D SEM synthetics incorporate the effects of gravity, rotation, topography and bathymetry, the oceans, and attenuation. We limit our attention to the period range between 40 and 500 seconds.

We use multi-taper measurements (see section 2.3) to quantify the time shifts and amplitude ratios between the synthetics and the observed data. We can both compare the measurements obtained for each station i at a fixed frequency f , $\delta\tau_i(f)$ and $\delta \ln A_i(f)$, or the combined measurements at a fixed frequency, averaged over stations; $\overline{\delta\tau}(f)$, $\overline{\delta \ln A}(f)$, or at a given station, averaged over frequencies; $\overline{\delta\tau}_i$ and $\overline{\delta \ln A}_i$. Also of interest is the variation of the measurements relative to these values; $\sigma^\tau(f)$, $\sigma^{\ln A}(f)$, σ_i^τ and $\sigma_i^{\ln A}$.

3.3.2 Results

In order to better understand how the average measurements are varying, we look at the original measurements, at a fixed frequency, and their variation with azimuth $\delta\tau_i(f)$, $\delta \ln A_i(f)$ (Fig. 3.8). At a period of 207 seconds there is still a slight effect of the directivity in the amplitude measurements. Note how the low rupture speeds have higher $\delta \ln A_i$'s than

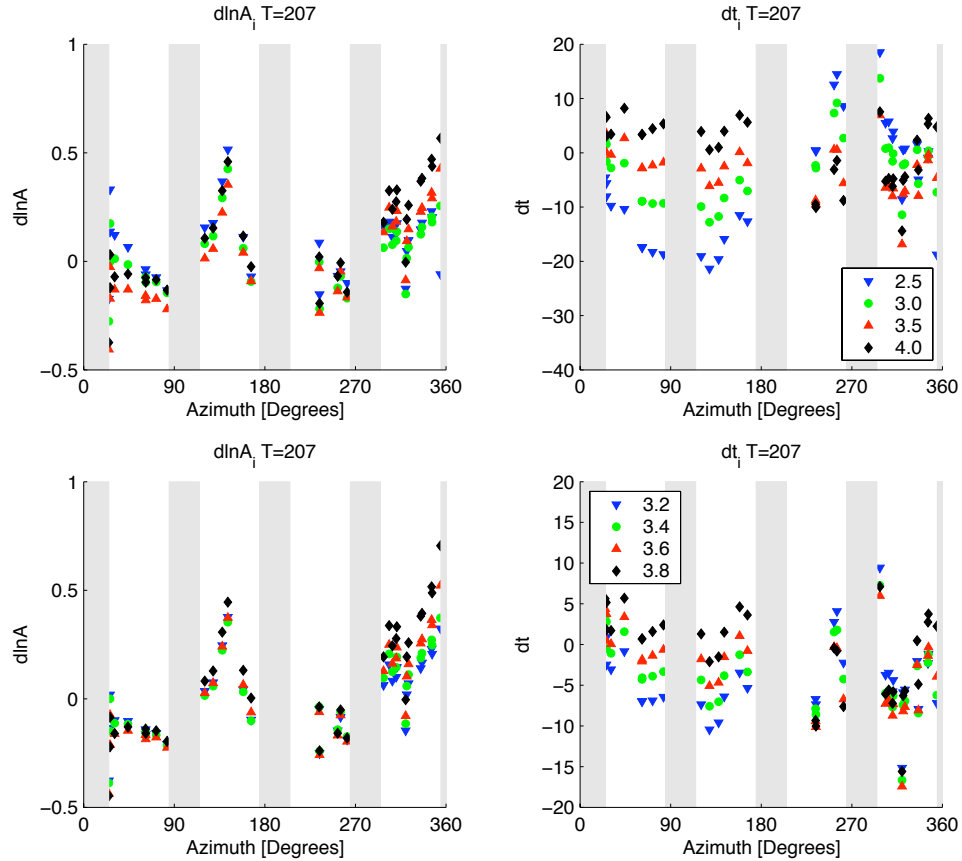


Figure 3.8: Amplitude ratios ($\delta \ln A$) and time shifts (δt) as measured at each station, for a frequency of 4.8 mHz (period of 207 seconds). The top panel shows the models for $v_r = 2.5, 3.0, 3.5, 4.0$ km/s. and the lower panel for $v_r = 3.2, 3.4, 3.6, 3.8$ km/s.

the other models in the direction of rupture, and vice versa. The time shifts have a very different pattern. Focusing for instance on those measured from a model with $v_r = 2.5$ km/s, we can see that the time shifts are most negative (the synthetics are late) in the direction of rupture, at an azimuth of 100° . In the opposite direction, however, the time shifts are not nearly as negative. The measurements for $v_r = 3.0$ km/s show a similar pattern. The measurements for $v_r = 4.0$ km/s show the opposite pattern, with synthetics in the rupture direction arriving earlier than observed, and those in the anti-rupture direction arriving later than observed. This can be understood in terms of the centroid location of the slip distributions. If the model centroid is closer to the epicenter than the observed centroid (when the rupture speed is too small) the synthetics will be late in the rupture direction, and vice versa. The opposite will happen when the rupture speed is too fast. From the above analysis we can therefore conclude that $v_r = 3.0$ km/s is too slow, and $v_r = 4.0$ km/s

is too fast. Note that we have masked out the measurements near the nodes of the radiation pattern, because the measurements become difficult when the amplitudes are small.

Next we look at the measurements as a function of frequency, averaged over all stations. The results are shown in Figs. 3.9 and 3.10. The average amplitude ratio, $\overline{\delta \ln A}(f)$, at long periods reflects the ratio of the moment of the synthetics and the data. When the moment is not constrained, the ratio varies as a function of frequency. As seen in Fig. 3.9 (a) the moment of the model is too large for rupture speeds of 2.5–3.5 km/s. The moment for rupture speed 4.0 km/s is slightly small. This illustrates the need to fix the moment in the body-wave inversions. We therefore proceeded to constrain the moment to the value predicted by the best-fitting point source (the Harvard CMT), $M_0 = 5.9 \cdot 10^{20}$ Nm. However, as seen in Figs. 3.9 (b) and 3.10 (b), this moment is slightly smaller than needed to match the surface waves. We therefore fix the moment in the third sets of inversions to $M_0 = 6.75 \cdot 10^{20}$ Nm. The amplitude ratios $\overline{\delta \ln A}(f)$ are a filtered estimate of the spectral ratios of the moment rate functions. Thus, a constant line corresponds to a difference in moment between the two models. A sloping line however, indicates a difference in the shape of the spectral ratios, or the shape of the moment rate function. We observe that the models with rupture speeds between 3 and 3.5 km/s all have near zero amplitude ratios for a wide frequency range. The average time shifts, at long periods, are related to the centroid time of the model. A zero time shift at long periods indicates the model has the same centroid time as the real earthquake. Varying time shifts with frequency indicate a difference in the shape of the moment rate function. We note that all the models have a somewhat small average time shift, but the flattest curves are those with rupture speed 3–3.5 km/s. The variation around the mean of both the amplitude ratios, and the time shifts are the variables that tell us how the measurements change with azimuth, and therefore are the ones that contain the most information of the directivity. We expect the ratios to go up somewhat with frequency, since our ability to account for the 3D effects diminishes with frequency, as observed in chapter 2. The smallest variation in amplitude ratios are observed for models with rupture velocities of 3–3.5 km/s, although the difference is not large between models. The difference between rupture speeds is more evident for the variation in time shifts, as can be expected from examining Fig. 3.8. The smallest time shifts over all are observed for the model with rupture speed of 3.2 km/s, although rupture speeds of 3.4–3.5 km/s produce similar results. The model with rupture speed 3.0 km/s predicts the largest time shifts for long periods

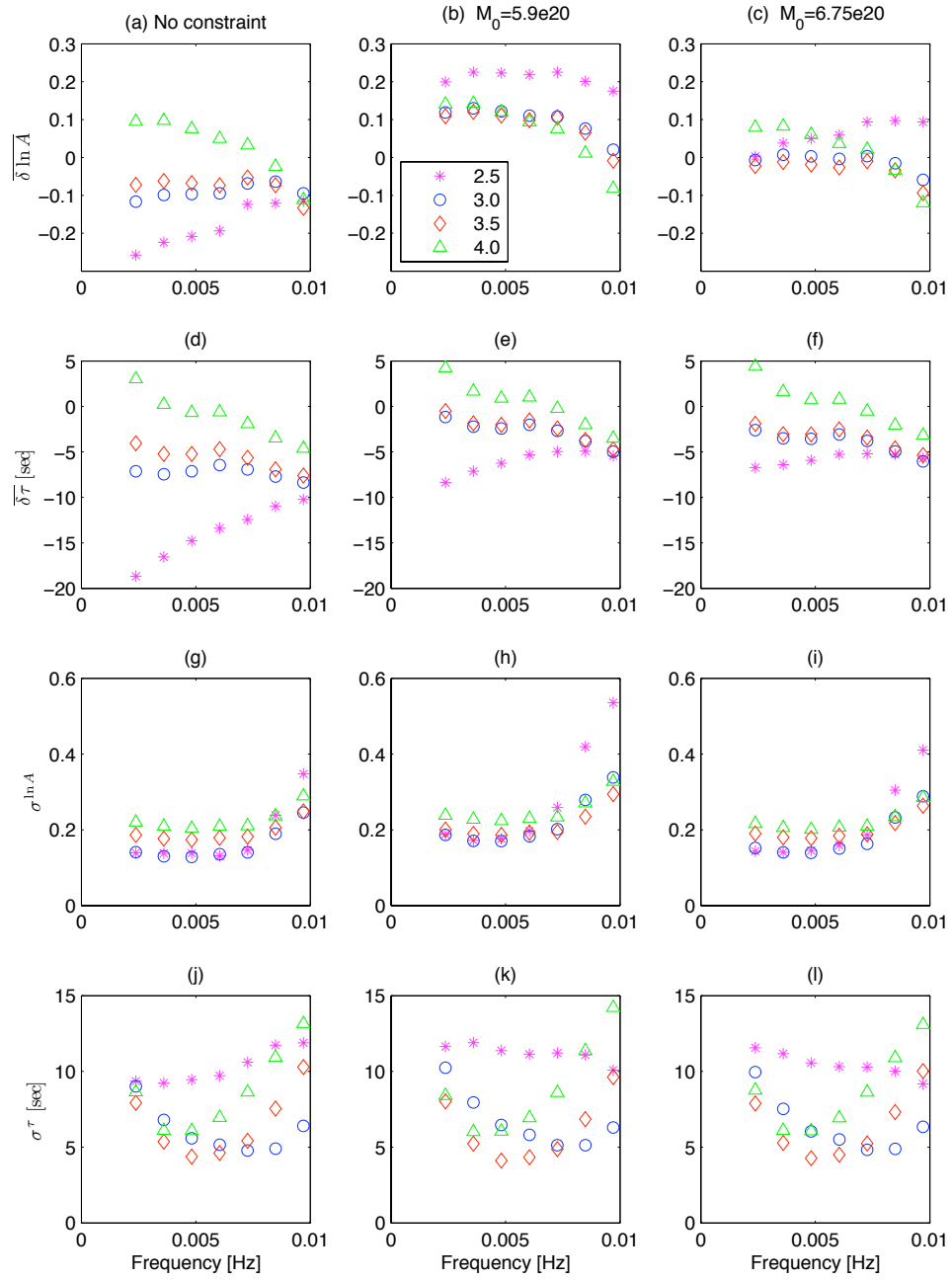


Figure 3.9: Multitaper measurements for the 3 different suites of models, for rupture speeds of 2.5, 3.0, 3.5, 4.0 km/s. The columns show the measurements for (left to right) models with no moment constraint, M_0 constrained to 5.9×10^{20} Nm and M_0 constrained to 6.75×10^{20} Nm. The rows show (top to bottom) $\delta \ln \bar{A}(f)$, $\delta \tau(f)$, $\sigma^{\ln A}$ and $\sigma^\tau(f)$.

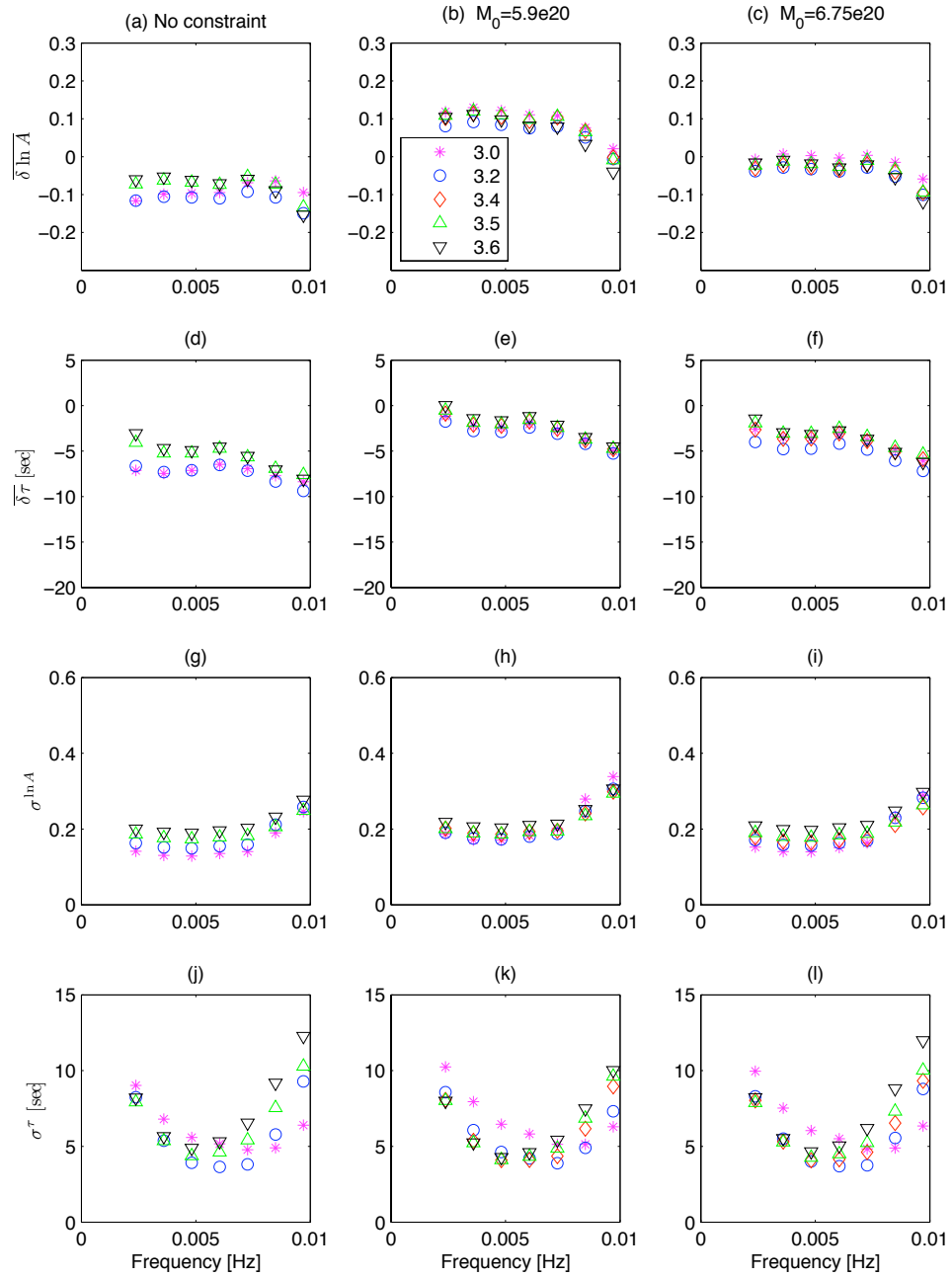


Figure 3.10: Same as Fig. 3.9, for rupture speeds $v_r=3.0, 3.2, 3.4, 3.6$ km/s.

(above 160 seconds), but the smallest time shifts observed for shorter periods (around 100 seconds).

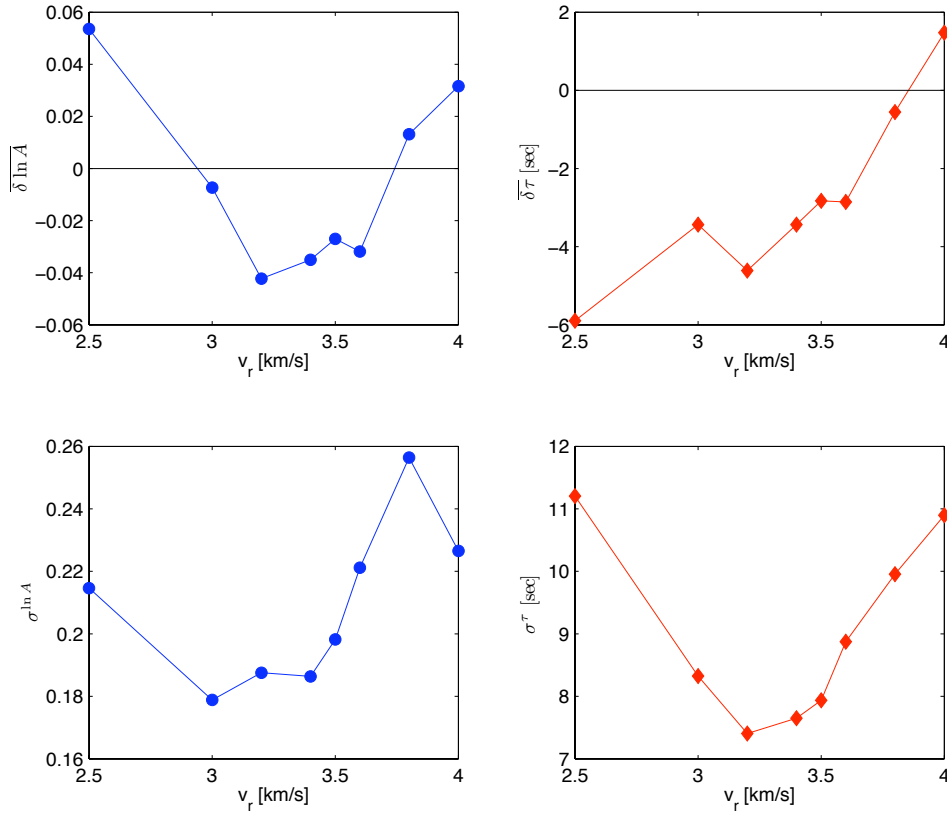


Figure 3.11: Measurements of $\overline{\delta \ln A}$, $\overline{\delta \tau}$, $\sigma^{\ln A}$ and σ^τ (left to right, top to bottom).

The overall averaged values of amplitude ratios and time shifts, and the variations therein are shown in Fig. 3.11. The average amplitude variation is mainly related to the moment of the event, which we fixed, and therefore does not provide much information on which rupture speed can best predict the data. The average time shifts can be influenced by a timing error of the hypocenter. Therefore we choose the model with the “flattest” curve as a function of frequency to be the “best fit” models for $\overline{\delta \ln A}$, $\overline{\delta \tau}$. These are models with rupture speeds of 3–3.5 km/s. The models with smallest $\sigma^{\ln A}$ and σ^τ are the ones with rupture speeds of 3.0–3.5 km/s and 3.2–3.5 km/s, with the lowest values at 3.0 and 3.2 km/s, respectively. Note that $\sigma^{\ln A}$ is only slightly higher than the value of 0.15 obtained for the Bhuj, India, earthquake 2 and σ^τ for rupture speeds of 3–3.5 km/s is smaller the value of 8.38 seconds observed for the Bhuj earthquake. This indicates that the models fit the data as well as can be expected given the accuracy of the 3D structure.

3.4 Relationship between surface offsets and the moment-rate function

An interesting aspect of the Kunlun earthquake is the mismatch between the shapes of the moment-rate function and the observed surface slip distribution. The moment rate was very small during the first 45 s of the event in comparison to next 45 seconds (Fig. 3.5), but the surface slip as reported by *Xu et al. (2002)*, *Lin et al. (2003)*, *van der Woerd et al. (2002)* and *Klinger et al. (2005)* is more uniform along the fault.

We wish to explore the relationship between the moment-rate and slip along the fault. In finite-fault inversions, the moment rate, $\dot{\mathbf{M}}(t)$ is well constrained, at least up to a long-period component. The moment rate, can be written as follows:

$$\dot{\mathbf{M}}(t) = \frac{d}{dt} \int_{\Sigma} \mathbf{m}(\mathbf{x}, t) d\Sigma \quad (3.1)$$

where the integral is over the faultplane Σ . The moment density tensor, is given by

$$\mathbf{m}(\mathbf{x}, t) = \mu(\mathbf{x}) \Delta s(\mathbf{x}, t) [\hat{\boldsymbol{\nu}}(\mathbf{x}) \hat{\boldsymbol{\sigma}}(\mathbf{x}) + \hat{\boldsymbol{\sigma}}(\mathbf{x}) \hat{\boldsymbol{\nu}}(\mathbf{x})] \quad (3.2)$$

where μ is the shear modulus Δs is the magnitude of slip, $\hat{\boldsymbol{\sigma}}$ is the slip direction and $\hat{\boldsymbol{\nu}}$ is the fault normal. In order to easily compare the moment rate and the surface slip, we have to make some simplifying assumption. First we assume that the slip direction and the fault normal do not change along the fault plane. Then:

$$\dot{\mathbf{M}}(t) = [\hat{\boldsymbol{\nu}} \hat{\boldsymbol{\sigma}} + \hat{\boldsymbol{\sigma}} \hat{\boldsymbol{\nu}}] \frac{d}{dt} \int_{\Sigma} \mu(\mathbf{x}) \Delta s(\mathbf{x}, t) d\Sigma = \sqrt{2} \hat{\mathbf{M}} \dot{M}(t) \quad (3.3)$$

where $\hat{\mathbf{M}}$, the unit source-mechanism tensor, is defined such that, such that $\hat{\mathbf{M}} : \hat{\mathbf{M}} = 1$ (*Dahlen and Tromp (1998)*, p 167). The slip along the surface of the fault is, in general, thought to be quite complicated. Here we will assume that neither μ or Δs change along dip, and only look at the changes in properties along strike:

$$\dot{M}(t) = \frac{d}{dt} \int_0^{x_f} \int_0^{w(x)} \mu(x) \Delta s(x, t) dy dx = \frac{d}{dt} \int_0^{x_f} w(x) \mu(x) \Delta s(x, t) dx \quad (3.4)$$

If we now further assume that once the rupture front reaches each point along the fault at

time $t_s(x)$, they have the same slip-time history, such that $\Delta s(x, t) = D(t - t_s(x))\Delta s(x)$ we get:

$$\dot{M}(t) = \int_0^{x_f} w(x)\mu(x)\dot{D}(t - t_s(x))\Delta s(x)dx \quad (3.5)$$

In order to proceed, we need the the form of $t_s(x)$. In general, for a unilateral rupture, propagating at speed v we have:

$$t_s(x) = \int_0^x \frac{1}{v(x)}dx \quad (3.6)$$

For a constant rupture speed, therefore $t_s(x) = x/v$ and using a change of variables $\xi = x/v$ we get:

$$\dot{M}(t) = \int_0^{x_f/v} w(\xi v)\mu(\xi v)\dot{D}(t - \xi)\Delta s(\xi v)v d\xi \quad (3.7)$$

Now we can rewrite the moment rate as a convolution:

$$\dot{M}(t) = \dot{D}(t) * v[w(vt)\mu(vt)\Delta s(vt)] \quad (3.8)$$

The slip rate at a point is often viewed as a boxcar, where the length of the boxcar is the duration of slip. For a long fault, this is small in relation to the time it takes to rupture the whole fault, and the moment rate function can therefor be seen as a slightly filtered version of the function $[w(x)\mu(x)\Delta s(x)]$. It is also of interest to understand how the relationship between the moment rate and the surface slip changes if the rupture speed changes. For simplification we will then assume that the slip rate is a delta function, $\delta(t - t_s(x))$. In a model where the rupture speed jumps from one fixed value v_1 to another fixed value of v_2 at time t_1 we would have:

$$\dot{D}(t) = \begin{cases} \delta(t - x/v_1) & : t < t_1 \\ \delta(t - t_0 - x/v_2) & : t > t_1 \end{cases} \quad (3.9)$$

where $t_0 = t_1(v_2 - v_1)/v_2$

$$\dot{M}(t) = \begin{cases} v_1 w(v_1 t)\mu(v_1 t)\Delta s(v_1 t) & : t < t_1 \\ v_2 w(v_2 t + x_0)\mu(v_2 t + x_0)\Delta s(v_2 t + x_0) & : t > t_1 \end{cases} \quad (3.10)$$

where $x_0 = t_1(v_1 - v_2)$. Now we can conclude that if the earthquake propagated unilaterally

at a fixed rupture speed, the rake angle remained constant along strike, if the slip averaged over depth is the same as the observed surface slip distribution, and if the shear modulus in the medium around the fault zone does not vary laterally, then the moment-rate function should have the same shape as the observed surface slip distribution. However, as can be seen by comparing Fig. 3.1 and Fig. 3.5 these quantities are quite different. From the above analysis, we can conclude that either the depth of the fault or the shear modulus varies significantly along strike, the surface slip is not a good indicator of the slip averaged over depth, the rupture speed varies along strike or a combination thereof. Constraining the slip at depth to match the surface slip, assuming a constant fault width and shear modulus, and inverting the surface waves (which are highly sensitive to the moment-rate function) *Bouchon and Vallée* (2003) attribute this disparity to a variation in rupture speed. In this study we have fixed the rupture speed in each inversion, assumed a constant shear modulus along the fault and attributed the disparity between surface slip and the moment rate function to variation in slip with depth. This works very poorly when the rupture speed is out of the reasonable range (as for $v_r=2.5$ and 4.5 km/s), and the disconnect between slip at the surface and at depth seems unreasonable. However, the models with rupture speeds between 3.2 and 3.8 km/s show a better continuity between the surface slip and the slip at depth. It is probably reasonable to assume that the variation in shear modulus along the fault is not substantial. It is however conceivable that both the variation in rupture speed along strike and the variation in slip with depth are significant.

3.5 Conclusions

Incorporation of 3D wave-speed structure in the SEM allows us to accurately model surface waves with periods longer than 100 s. Using the resulting synthetics, we estimate that the average rupture speed of the 2001, Kunlun, China, earthquake is 3.0–3.5 km/s. This is to be compared to the local shear wave speed, that is 3.5 km/s, or the Rayleigh speed which is $0.92v_s = 3.15$ km/s. The range unfortunately is too large to conclude whether the rupture speed exceeded the shear-wave speed or not. The average value is similar to, or somewhat lower, than the values of 3.4 km/s obtained by *Ozacar and Beck* (2004) and 3.6 km/s by *Antolik et al.* (2004) from body-wave modeling. This value is significantly lower than the 3.7–3.9 km/s obtained by *Bouchon and Vallée* (2003) from modeling surface waves recorded

at regional distances. The aforementioned studies indicate a low rupture speed during the initial stages of rupture. In order to keep the average rupture speed at the estimated value, this would suggest larger rupture speeds, perhaps supershear, during the later stages of rupture, as suggested by *Bouchon and Vallée (2003)*. A transition from low rupture speed at early stages of rupture, to higher rupture speed at the later stages, could explain in part the difference in shape between the moment-rate function and the surface-slip distribution, although it is not advisable to attribute the whole difference to this effect as there are other effects that can produce the same result.

Chapter 4

The 1998 Balleny Islands earthquake

4.1 Introduction

The M_w 8.1, March 25, 1998 event in the Antarctic plate, near the Balleny Islands, occurred on a fault about 300 km from the nearest plate boundary (Fig. 4.1). This event has been studied extensively by many authors as it exhibits many peculiarities. The tectonic setting is somewhat puzzling both due to the distance to the nearest plate boundary and because most fault models prescribe slip on a fault plane perpendicular to the fracture zones in this region. Due to sparse instrumentation in the southern hemisphere, source inversions are difficult; still, many slip models have been obtained from body waves for this earthquake (*Kuge et al.*, 1999; *Nettles et al.*, 1999; *Antolik et al.*, 2000; *Henry et al.*, 2000; *Tsuboi et al.*, 2000). The Harvard CMT solution has a large non-double couple component that *Kuge et al.* (1999) explain in terms of slow normal fault slip during the event and *Antolik et al.* (2000) interpret as a compound rupture of a normal fault and a strike slip fault. One of the more detailed body-wave source models (*Henry et al.*, 2000) has a 100 km stretch of no slip between two distinct slipping fault patches (Fig. 4.5), and therefore the fault propagation is difficult to explain with the standard rupture model in which rupture propagation is controlled by a stress concentration at the crack tip. By using surface waves (with periods of 135 seconds and longer) *Henry et al.* (2000) conclude that the non double-couple part of the moment tensor is ill constrained. They present two purely double-couple solutions that give near equal fits to the surface-wave data (we will refer to these as HenryC and HenryD) and similar fits as the Harvard CMT, thereby eliminating the need for a non double-couple

component of the moment tensor. They then invert body waves for a source model which yields a new double-couple focal mechanism, HenryF, similar to HenryD.

Here we first compare the radiation patterns for the different focal mechanism, to investigate whether we could distinguish between them by looking at long period (100–500 second) surface waves. We then compute surface waves for the finite source model based on body waves, presented by *Henry et al. (2000)*, to see whether this model, without a non double-couple component, can explain the observed surface waves.

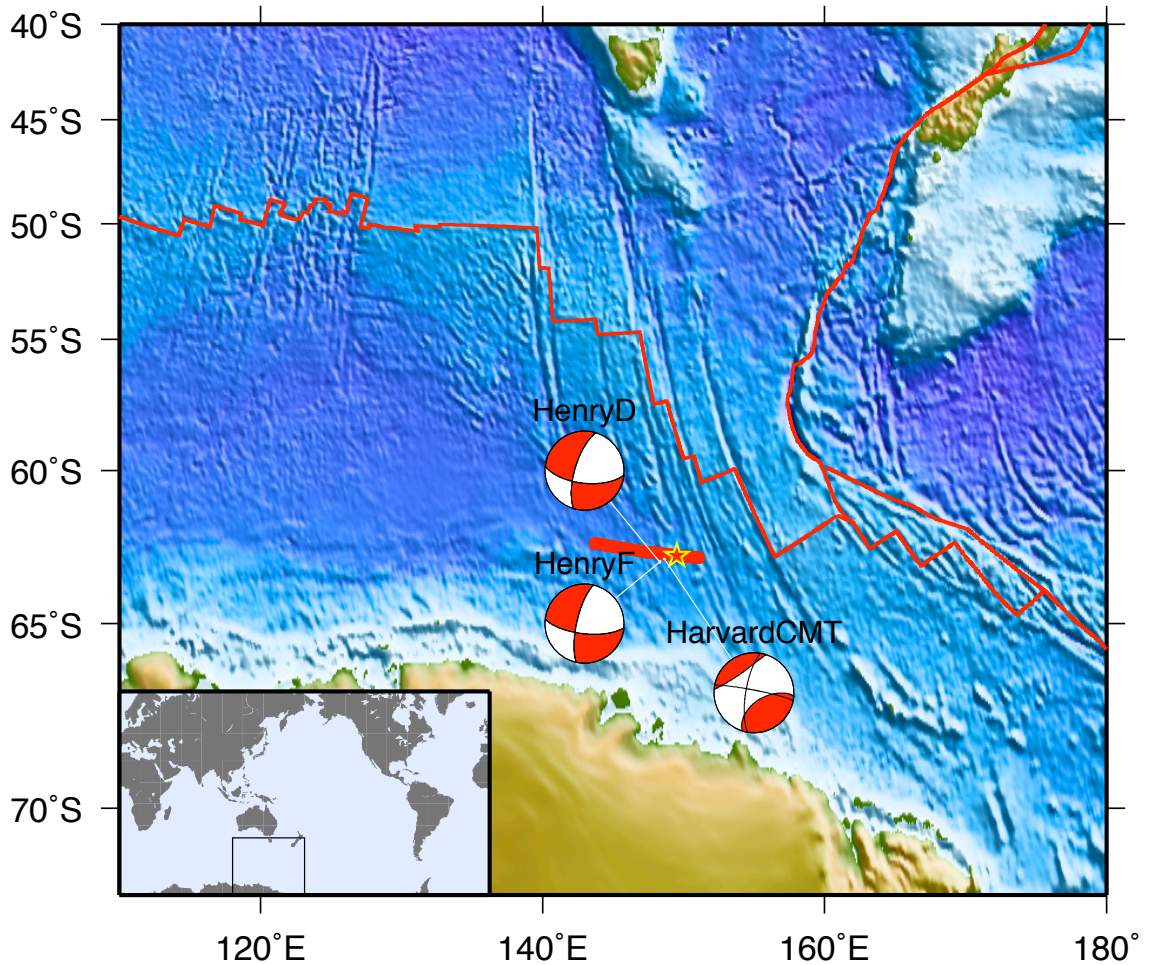


Figure 4.1: The Balleny Island earthquake occurred relatively far from plate boundaries (thin red lines), and most researchers agree that the fault plane is close to perpendicular to the plate fabric. We use the source model from *Henry et al. (2000)* to calculate 3D synthetic seismograms. The moment tensor shown is that favored by *Henry et al. (2000)*, and the source-time function is a modified version of the source-time function from the same study.

4.2 Point sources

We compute the radiation pattern as described by *Ben-Menahem and Harkrider (1964)* and *Kanamori and Given (1981)* for three unit point sources: the Harvard CMT, HenryD and HenryF (Fig. 4.1). The source parameters are given in table 4.1. The moment tensor elements are normalized such that the full moment tensor is given by $\mathbf{M} = M_0 \mathbf{m}$, the scalar moment is given by $M_0^2 = (\mathbf{M} : \mathbf{M})/2$ and the centroid time is given by t_0 . The radiation patterns are shown in Fig. 4.2. The difference between HenryF and the others is evident for the smaller lobes of the radiation pattern, between 20° – 90° and 200° – 270° , but solutions HarvardCMT and HenryD are very similar, and it would be very difficult to distinguish between them if there was a little bit of noise in the data. We therefore conclude that with our data set we would not be able to distinguish between the two models.

Table 4.1: Comparison of focal mechanisms used to model the Balleny Island earthquake

Model	M_0	m_{rr}	$m_{\theta\theta}$	$m_{\phi\phi}$	$m_{r\theta}$	$m_{r\phi}$	$m_{\theta\phi}$	t_0
HarvardCMT	$1.86 * 10^{21}$	-0.3557	0.4959	-0.1401	0.3718	-0.2156	0.7869	37.4
HenryD	$1.30 * 10^{21}$	-0.3079	0.4766	-0.1687	-0.1971	0.4265	0.7773	36.6
HenryF	$1.40 * 10^{21}$	-0.2068	0.3891	-0.1823	-0.1928	0.3630	0.8470	36.8

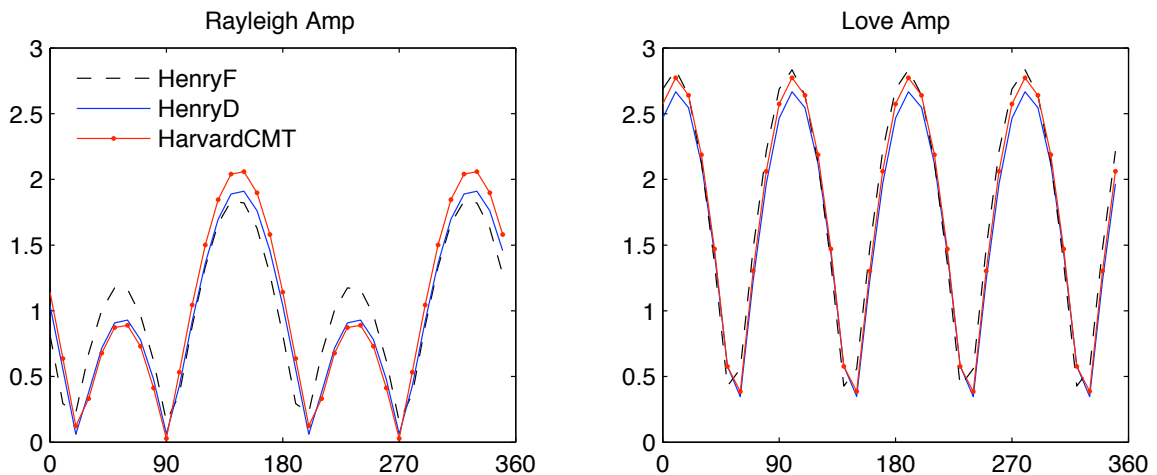


Figure 4.2: Radiation patterns for three different unit point sources, computed at 256 seconds. Notice that models HenryD and HarvardCMT are near indistinguishable, whereas HenryF has larger amplitude Rayleigh waves between 20° – 90° and 200° – 270° .

The waveforms computed for the Harvard CMT are shown in Fig. 4.3. At a first glance they seem to match the data remarkably well. However, when scrutinizing, the synthetics to the west are generally smaller than the data and vice versa. For comparison with later sections we compute multi-taper estimates of time shifts and amplitude anomalies between data and synthetics, in a similar fashion as in previous chapters. The results are shown in Fig. 4.4 for periods of 207 and 420 seconds, for both Rayleigh and Love waves.

The amplitude anomalies $\delta \ln A_i$ resemble a fairly smooth sine-wave pattern, positive to the west and negative to the east, that can be explained by west-ward propagating rupture (*Ben-Menahem, 1961*). The time shifts $\delta \tau_i$ are near zero for all azimuths at 207 seconds, for both Rayleigh and Love waves. At 420 seconds they are also near zero for westward azimuths, for both wave types, although significantly different from zero in eastward azimuths. The synthetics arrive as much as 20 seconds earlier than the data in east-ward azimuths for Rayleigh waves, and 40 seconds for Love waves. This general shape of the sinusoidal pattern of time shifts can be explained by a mislocation of the source. The baseline of the sinusoid is then indicative of the source delay relative to the estimated one, here around 15 seconds. The amplitude of the sinusoid is related to the mislocation of the source. This results show that the 400 seconds waves are consistent with a point source that occurs later and further west than the point source consistent with the 200 seconds waves. From this we can immediately expect some sort of asymmetric triangular source time function, with a rapid rise in slip near the epicenter, slowly falling off in time and towards the west. The Harvard CMT was constructed to fit mantle waves of 135 seconds and longer and does a very good job of matching the data at 207 seconds. It is interesting, however, that there is such a discrepancy for the longer period data, indicating that the source is not well matched by a point source at 135 seconds and longer.

4.3 Body-wave source model

As the point source modeling indicates that a non double-couple component is not needed to match the data, although allowable, it is of interest to see whether a purely double-couple body-wave model can fit the surface waves. We use the source-time history from *Henry et al. (2000)* to calculate 3D synthetics for the Balleny Islands event (Fig. 4.5). The model was obtained by inverting body waves for the slip on two fault planes. The slip is mainly

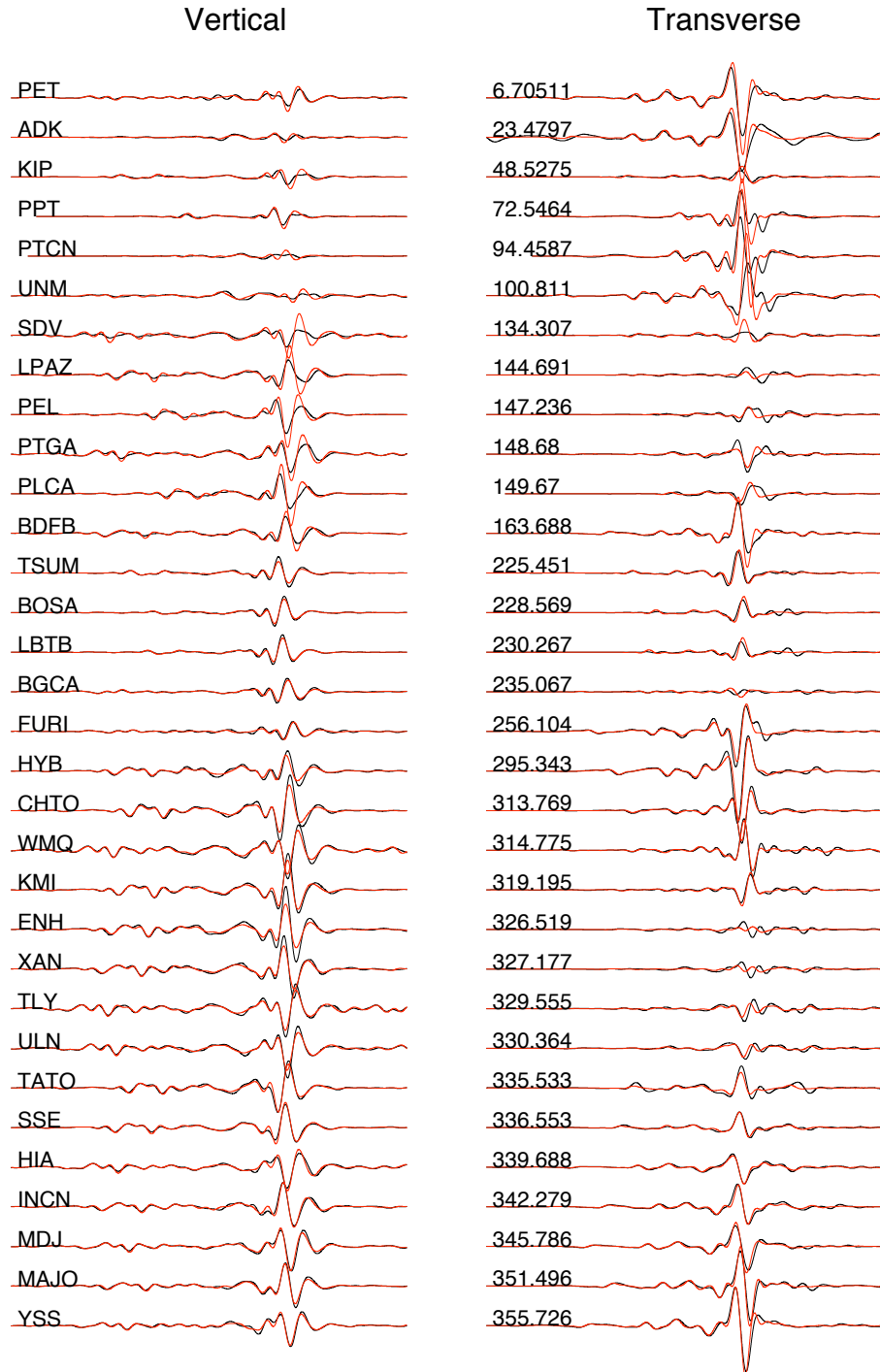


Figure 4.3: Waveforms at stations between 60 and 120 degrees computed for the Harvard CMT. Data are shown in black and the 3D synthetics in red. All traces have been band-pass filtered between 100 and 500 seconds. The vertical component is shown on the left and the transverse component on the right. Shown are 3000 seconds, aligned on the arrival of the Rayleigh and Love waves for the vertical and transverse components respectively. Station names are shown on the left and azimuths in the middle. Notice that the amplitudes of the data are generally overestimated to the east and underestimated to the west.

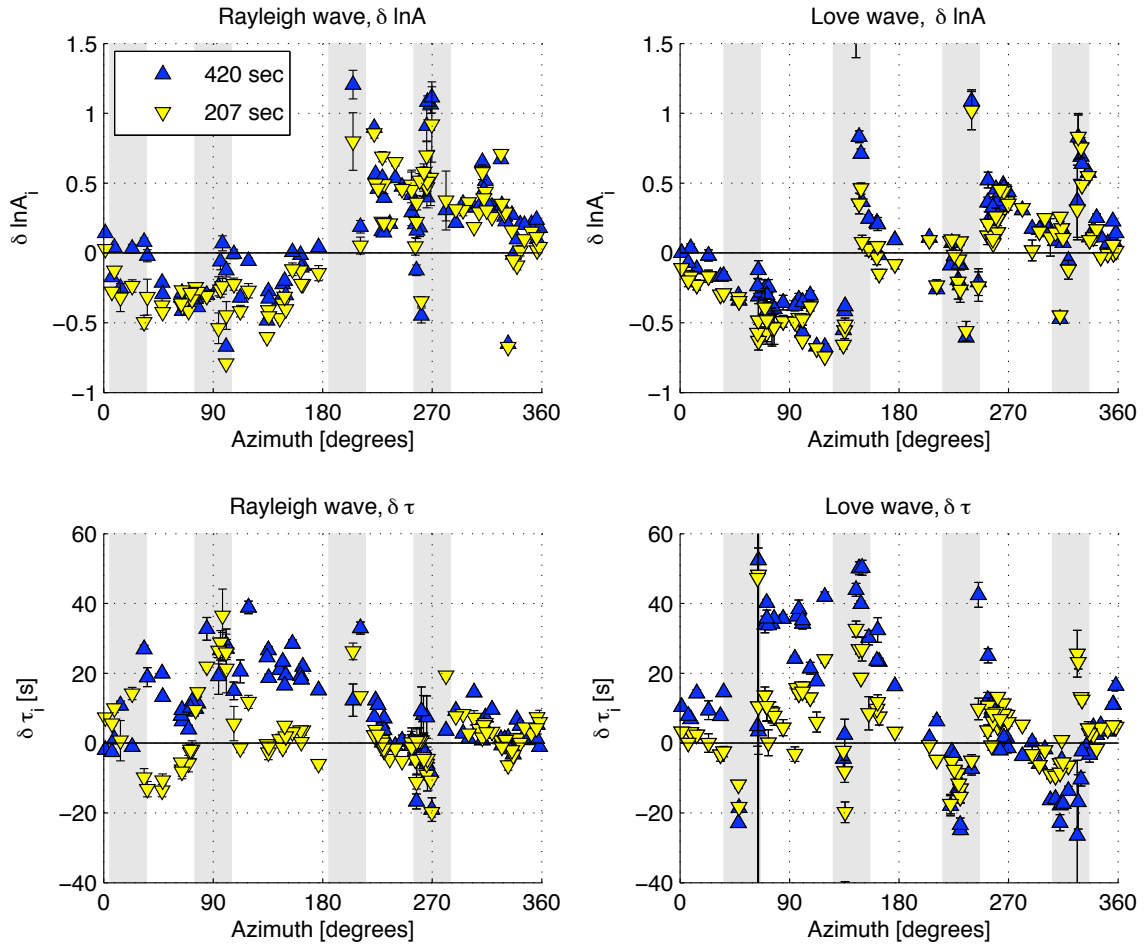


Figure 4.4: Multitaper measurements of amplitude anomalies and time shifts between data and synthetics computed for the Harvard best-fit point source. As expected for a point source, there is an amplitude anomaly associated with the directivity. Positive amplitudes denote larger data than synthetics. Positive time shifts indicate earlier arrivals in the synthetics than data. Both the amplitude and the time-shift patterns show clearly that the main propagation of rupture was to the west. Near-nodal azimuths are shown as shaded areas.

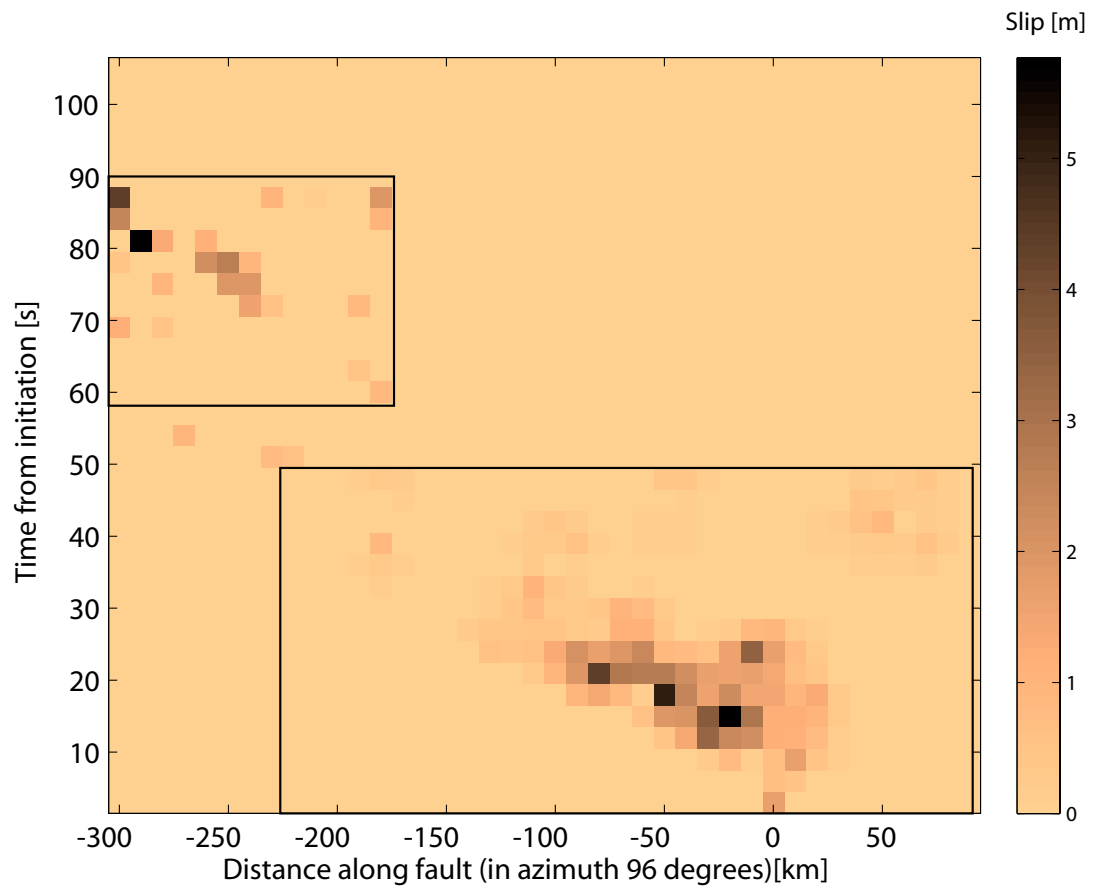


Figure 4.5: Source model from *Henry et al.* (2000) used in our simulations. The authors emphasize that the well-constrained parts of the solution are those in the rectangular boxes marked on the plots, which they refer to as subevents 1 and 2.

concentrated in a region within 100 km away from the hypocenter, rupturing mainly to the west. In addition there is slip around 80 seconds after the first event, 250 km to the west. The regions, in space and time, where the authors are confident in their slip models are shown with white boxes on Fig. 4.5.

At first glance (Fig. 4.6), the waveforms are very well predicted by the synthetics. However, upon closer inspection of the long-period waves in front of the main arrival of the surface waves it becomes clear that the very long-period part of the data is not matched by the synthetics. The observed amplitude discrepancies between east and west are similar as those for the Harvard CMT, indicating that the source does not produce the required amount of directivity. To quantify the differences we again turn to the multi-taper measurements of amplitude differences and time shifts (Fig. 4.7). As observed in the waveforms, the amplitudes towards the west are under predicted, both in the Rayleigh and Love waves. However, the amplitude ratios for the Rayleigh waves do not form a simple sinusoid as a function of azimuth as for the Harvard CMT. Instead, the amplitude ratios are slightly smaller, or similar, to the southwest than to the southeast, close to zero in the northeast and very large in the northwest. By comparing the amplitude anomalies for model HenryD (Fig.4.7) with the radiation patterns for the point sources (Fig. 4.2) we can guess that this is a result of using the focal mechanism HenryF. This focal mechanism was obtained from body waves and although *Henry et al.* (2000) state that the difference in misfit to the surface data between HenryD and HenryF is negligible at 135 seconds, this indicates that, in fact, HenryD can predict the longer-period surface waves better. We therefore repeat the simulation using the same slip model but using the surface-wave focal mechanism HenryD. The waveforms for this model are shown in Fig. 4.8 and the amplitude anomalies and time shifts are shown in Fig. 4.9.

The pattern of amplitude ratios for the Rayleigh wave is now showing a similar pattern as that for the Harvard CMT, although offset by a constant, with smaller amplitudes than observed in the eastward direction, but similar to observed to the west. A similar pattern can be seen for the Love wave, although the data around the nodes (in the shaded regions) show significant variations. Notice that almost all the amplitude ratios are positive, indicating that the model has a moment that is smaller than needed to explain the data. The time shifts for both the Rayleigh wave and the Love wave indicate an earlier arrival than observed in all directions, and more so in the west than in the east. This indicates that there is significant

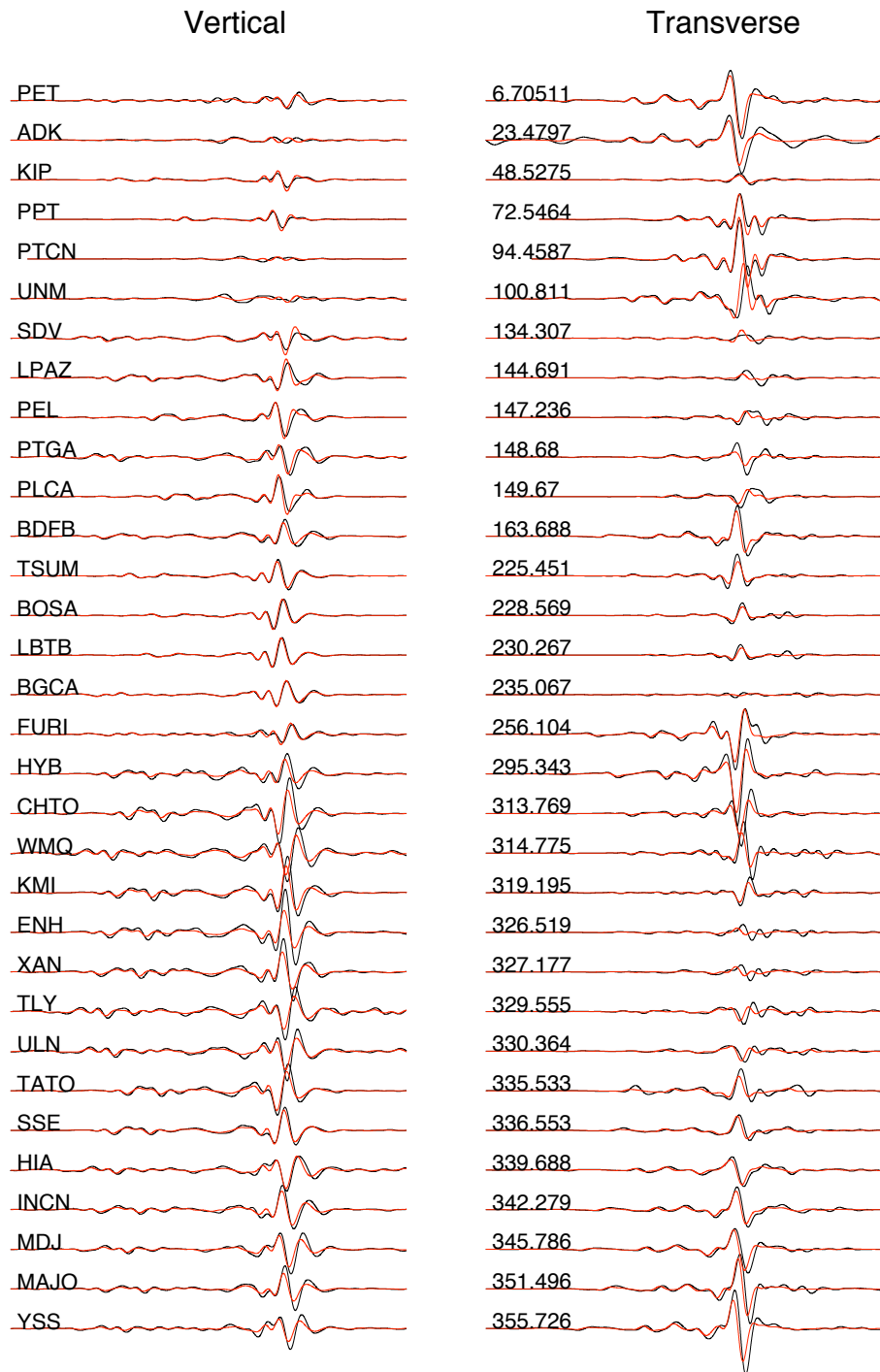


Figure 4.6: Waveforms computed for model HenryF. Data are shown in black and the 3D synthetics in red. All traces have been band-pass filtered between 100 and 500 seconds. The vertical component is shown on the left and the transverse component on the right. Shown are 3000 seconds, aligned on the arrival of the Rayleigh and Love waves for the vertical and transverse components respectively. Station names are shown on the left and azimuths in the middle. Same as Fig. 4.3, except for the synthetics used. Notice that the synthetics to the west are generally small compared to the data, and that over all the synthetics are slightly shifted forward relative to the data. These differences are quantified at fixed periods in Fig. 4.7.

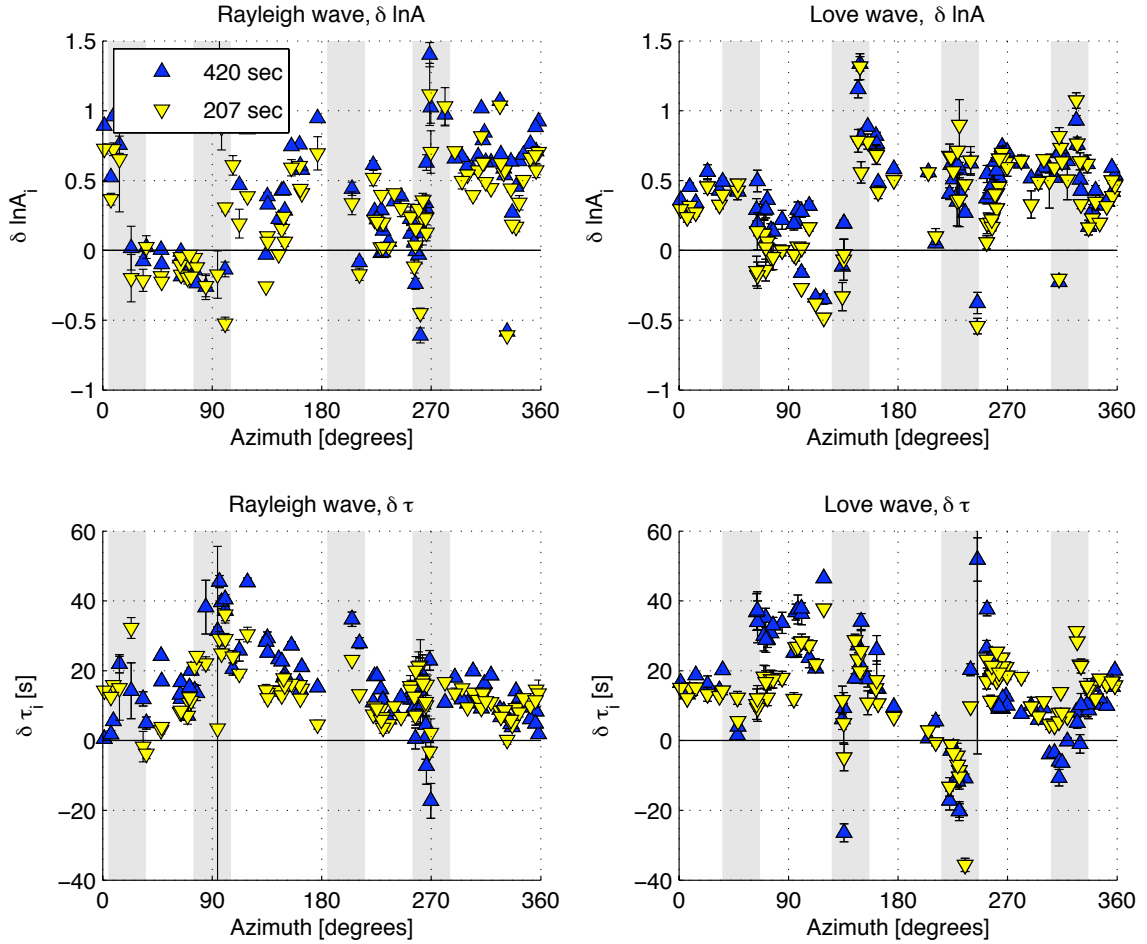


Figure 4.7: Multitaper measurements of amplitude anomalies and time-shifts between data and synthetics computed for the *Henry et al.* (2000) source model (Fig. 4.5), with focal mechanism HenryF. Note that almost all the amplitude measurements are positive, indicating that the amplitudes of the long-period seismic waves are underestimated by this model. Note that the directivity is underestimated as well (the amplitude ratios are azimuthally dependent).

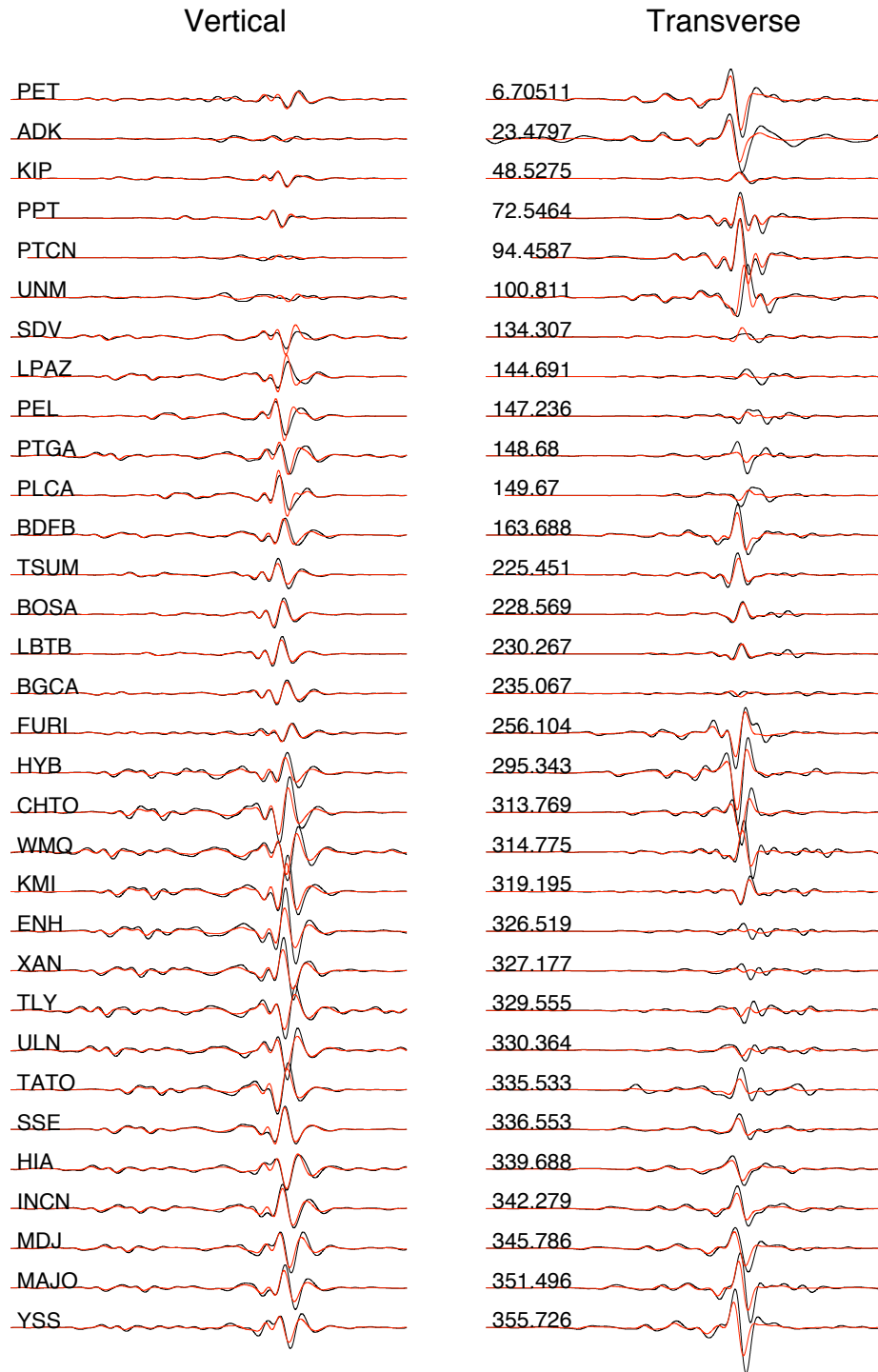


Figure 4.8: Waveforms computed for model HenryD. Data are shown in black and the 3D synthetics in red. All traces have been band-pass filtered between 100 and 500 seconds. The vertical component is shown on the left and the transverse component on the right. Shown are 3000 seconds, aligned on the arrival of the Rayleigh and Love waves for the vertical and transverse components respectively. Station names are shown on the left and azimuths in the middle. The differences in the synthetics for mechanisms HenryD and HenryF are not readily discerned by eye, but are extracted by the amplitude ratio and time-shift measurements (Fig. 4.9).

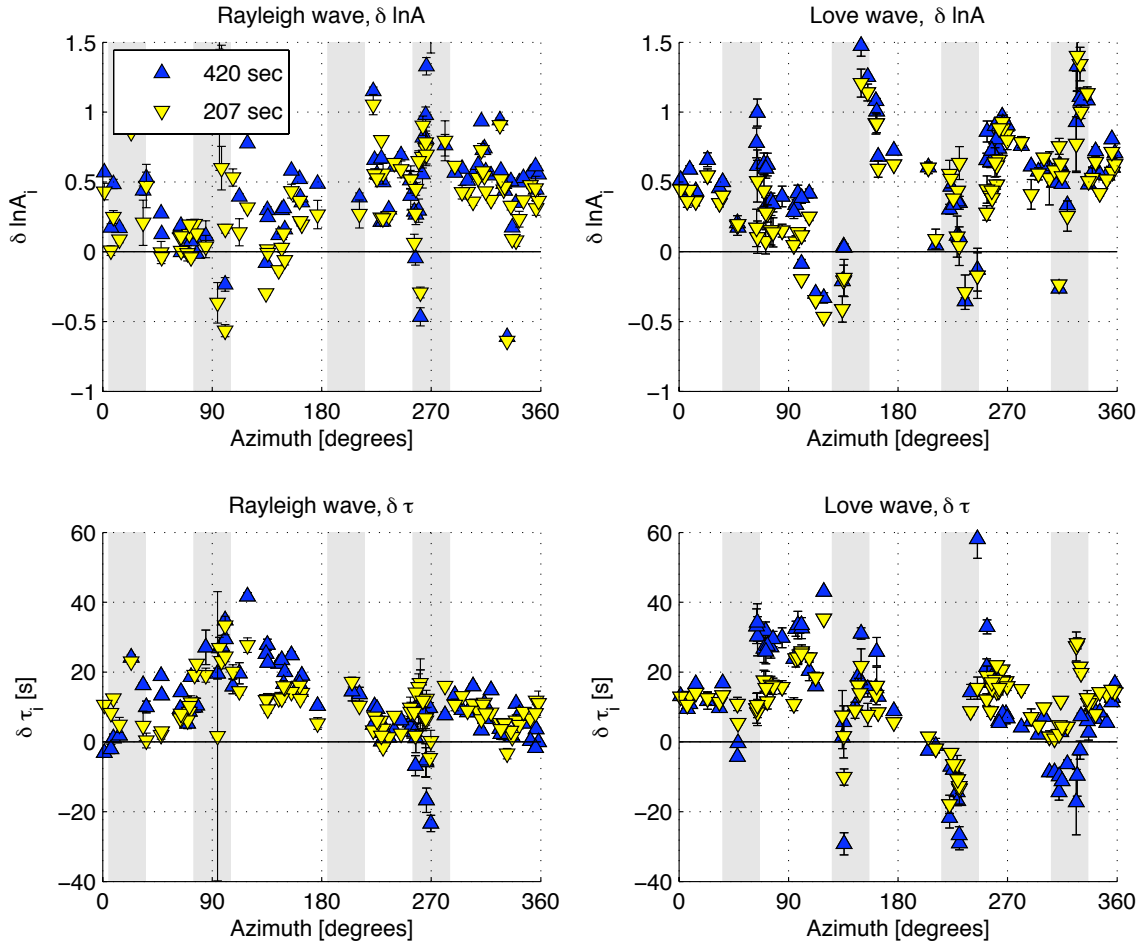


Figure 4.9: Multitaper measurements of amplitude anomalies and time shifts between data and synthetics computed for the *Henry et al. (2000)* source model (Fig. 4.5), with focal mechanism HenryD. The main differences between using focal mechanisms HenryD and HenryF are seen in the amplitude ratios of in the Rayleigh wave. The amplitude ratio is now more similar to a simple sinusoid, indicating that the remaining discrepancy is due to how the rupture propagates along the fault plane, not the geometry thereof.

slip at later times than predicted by the body-wave model.

4.4 Modification of the body-wave model

Since the overall amplitudes of the synthetics for the finite source model with focal mechanism HenryD match the records at shorter periods (Fig. 4.8) but not at long periods (Fig. 4.9), we can exclude the possibility that the source time function should be scaled by a constant. Furthermore, the observed time shifts indicate that the missing slip occurs at a later time than the main slip prescribed by the body-wave model.

The lack of long-period energy is not surprising when we consider that the data used for the body-wave inversion were band passed between 2 and 120 s, and thus the very long-period energy in the body waves was filtered out. Furthermore, body-wave inversions are known to be insensitive to the long period components of slip and therefore to the moment of an earthquake (*Ekström, 1989*). We would like to find a model that can explain the data over the entire frequency range. Consequently, we need to add a component that augments the amplitude of the signal at long periods, but does not affect the shorter periods. One way of doing this is to assume that the two subevents described by *Henry et al. (2000)* are on a single fault plane and modify their model by adding slip between the two events. We accomplish this by adding slip to the fault with a moment rate function of the form: $\dot{M}(t) = \Delta M_0 \sin(\pi t/T), t \in [0, T]$ sec, where ΔM_0 is the total moment of the added slip and T is the duration of the rupture. The slip is assumed to propagate along the entire fault with a fixed rupture speed of $300/T$ km/s (Fig. 4.10). Adding long period slip to body-wave source inversion was common practice in the late 80's (e.g. *Kikuchi and Fukao 1987* and *Beck and Ruff 1987*) when interpreting body waves recorded by the WWSSN network that had a limited bandwidth. Due to the insensitivity of body waves to the long-period components of slip, however, this is still a useful practice in the age of modern digital seismology.

Notice that here there are two free parameters, the added moment, ΔM_0 and the duration of rupture, T . We experimented with both, using trial and error, to obtain good fits to the long-period radiation pattern. We found that $\Delta M_0 = 8 * 10^{20}$ Nm and $T = 100$ seconds give the best fits. The duration of rupture in the original model is $T = 90$ seconds, but that gives a slightly worse fit to the time shifts. The waveforms for this new model are shown

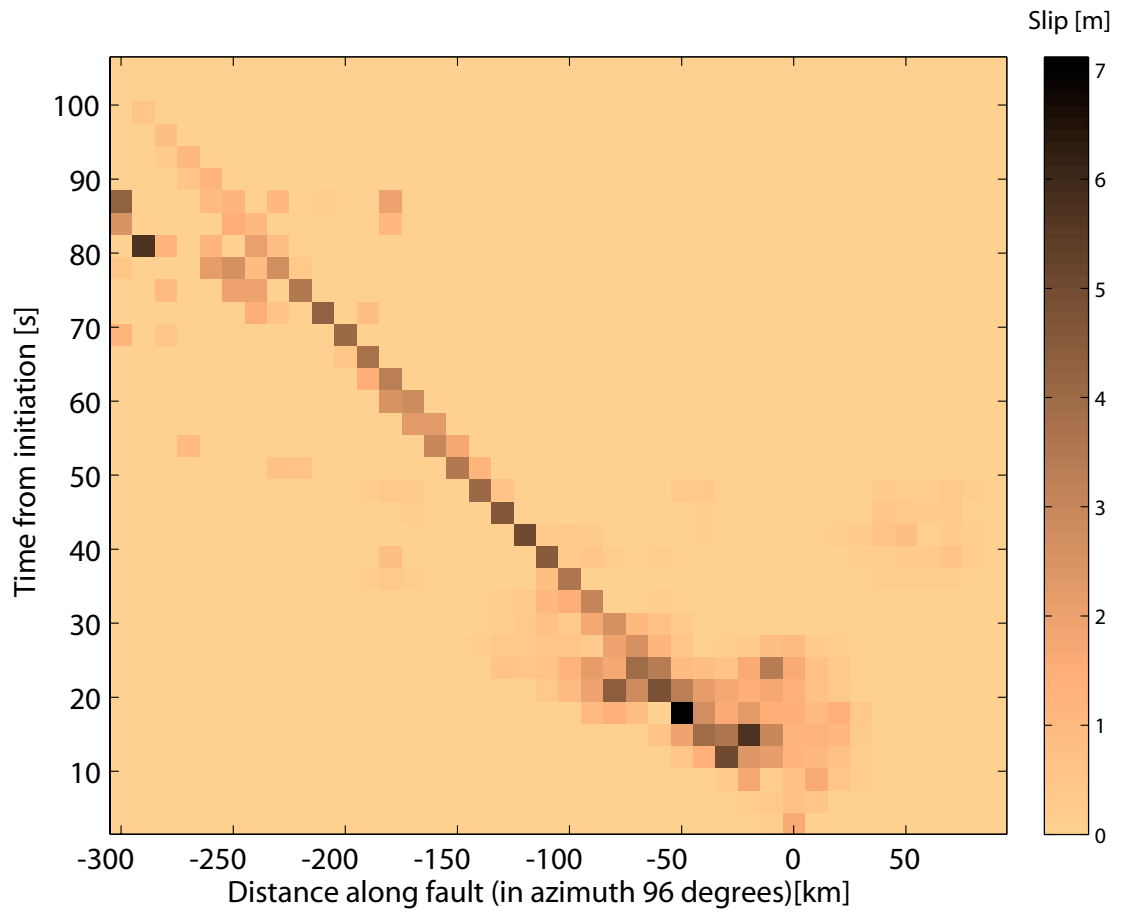


Figure 4.10: The slip model modified from *Henry et al.* (2000) to better fit the long-period radiation pattern. Point sources are added along the line representing a constant rupture speed of 3.0 km/s in a smooth manner as described in the text.

in Fig. 4.11 and the multi-taper measurements in Fig. 4.12

On average the time shifts and amplitudes of both Rayleigh and Love waves are close to zero. There are significant variations in the nodal regions, indicating that perhaps we could obtain better fits by a slight rotation of the strike of the event. Comparing to Fig. 4.4 and Fig. 4.9 we see that the model with an added component of smooth slip has smaller amplitude anomalies and time shifts than the other finite fault models.

4.5 Discussion

We computed long-period synthetics for a body-wave source model of the Balleny Island event (*Henry et al.*, 2000), but find that the model predicts much smaller amplitudes at long periods than observed. We present a modification of the *Henry et al.* (2000) source model that incorporates long-period slip across the whole fault plane. The need for this added slip can be understood by looking at the moment-rate functions for the different models (Fig. 4.13). The Harvard CMT is the point source that best fits the long-period data, in this case surface waves low-pass filtered at 135 seconds. The source has a triangle source time function (here represented by the Gaussian that best fits the triangle) with a half duration that is scaled from the moment (Fig. 4.13). In an ideal case, the center of the triangle coincides with the first moment of the moment rate function of the earthquake. Comparing the moment rate function of the Harvard CMT and the one from *Henry et al.* (2000) we can immediately see that the centroid of the second model is too early. Comparing the source spectra, we can see that the difference between the original finite model and the modified model only appears at 80 seconds and longer. We can also see that at 200 seconds we are not yet at the flat part of the spectra for the finite models.

We have compared the models visually at 207 seconds and 420 seconds. We can give a more quantitative measure of the quality of fit of the models by using the definitions of $\overline{\delta \ln A}$ and $\overline{\delta \tau}$. These values, averaging over all azimuths and periods between 100 and 500 seconds are given in Fig. 4.14. The average amplitude ratios are close to zero for both the Harvard CMT and the modified finite model. However, the finite models with both focal mechanisms have large average time shifts and amplitude anomalies. The variations around the averages are largest for the Harvard CMT and smallest for the modified finite model. We also note that the averages for this frequency band are similar to those obtained for

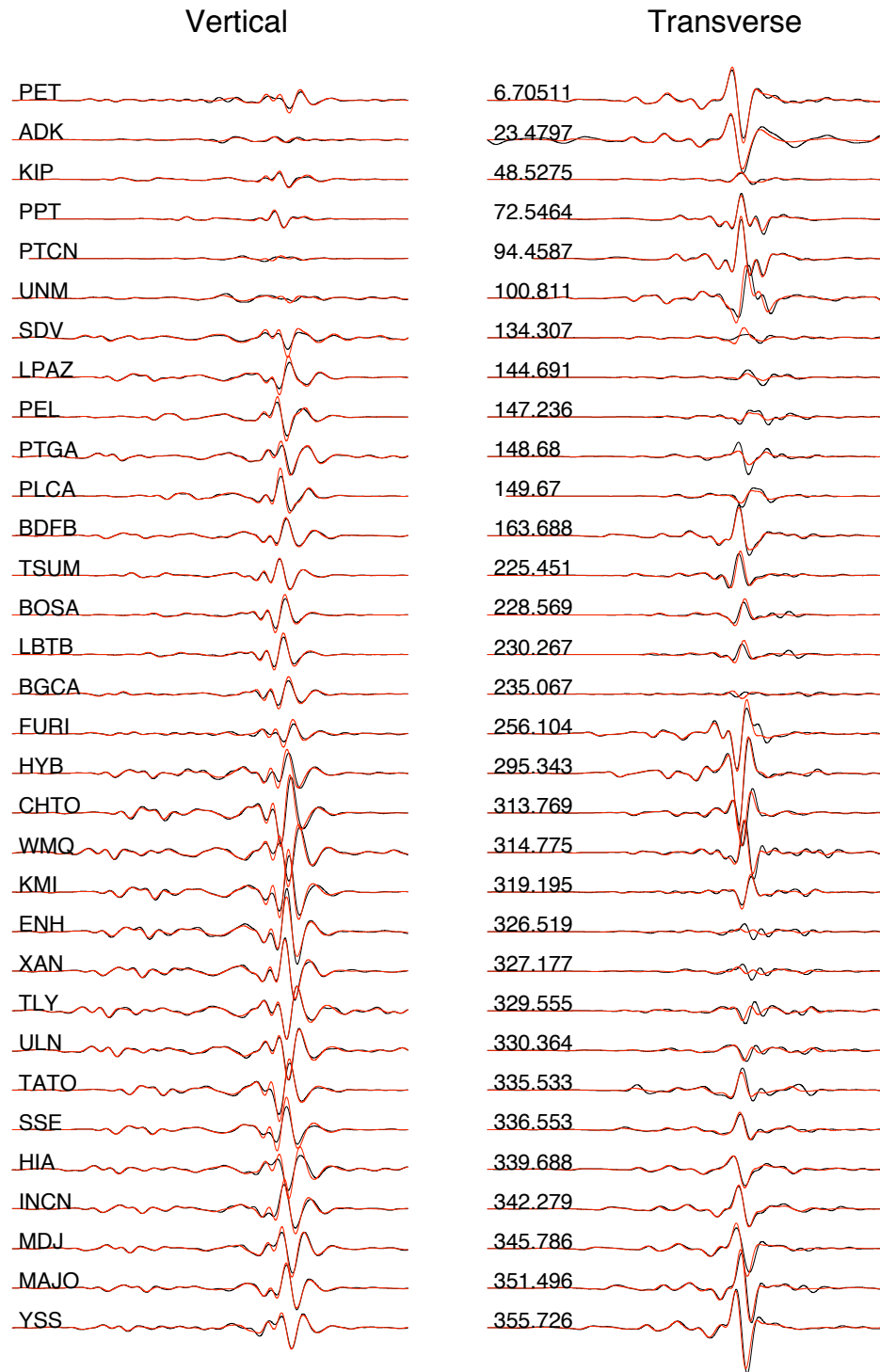


Figure 4.11: Same as Fig. 4.8 except with synthetics computed for the modified source model. Now the amplitude and phase of the surface waves match the data better. Furthermore, it is interesting to note that even the earlier phases, that were not used to constrain the model, are also better matched.

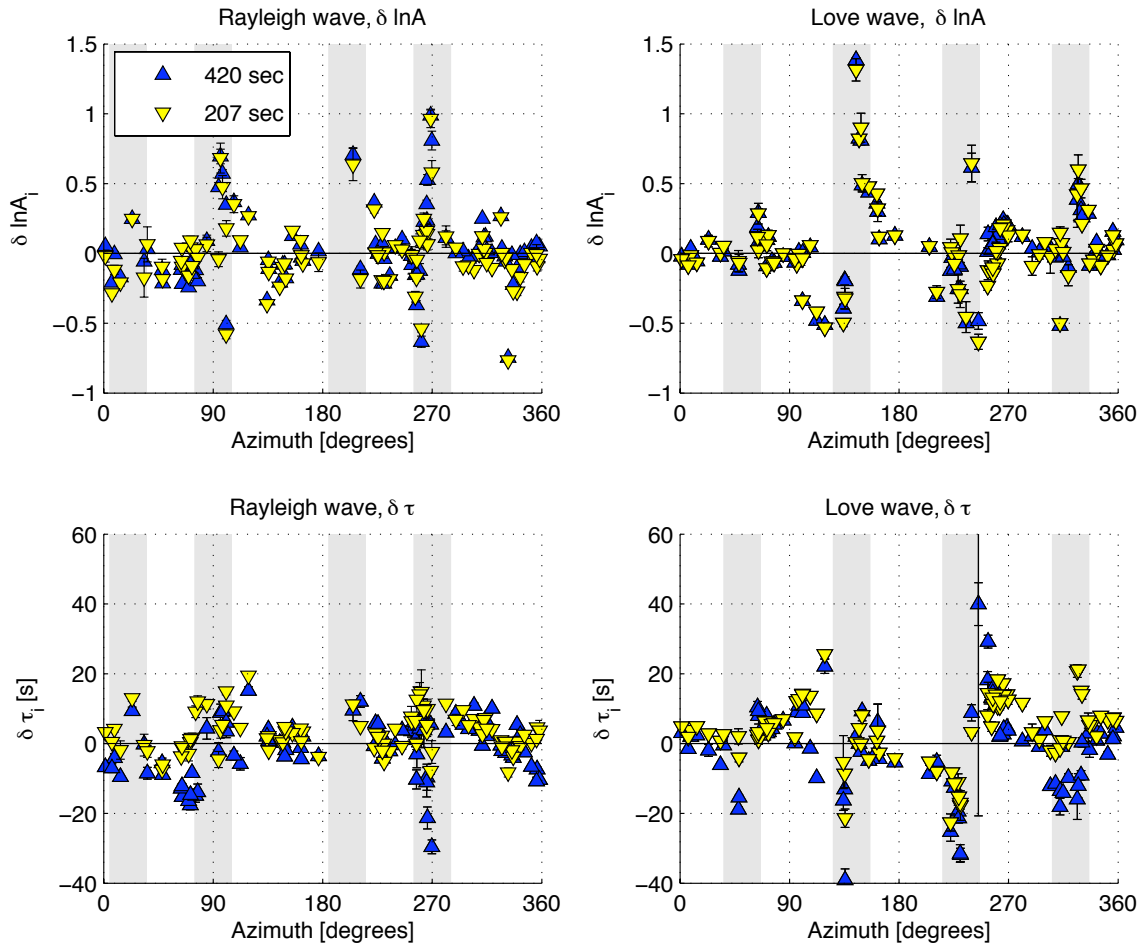


Figure 4.12: Multitaper measurements of amplitude anomalies and time shifts for the modified *Henry et al.* (2000) source model (Fig. 4.10). Notice that on average now all the measurements are close to zero, for both Rayleigh and Love waves, at both periods of 207 and 420 seconds.

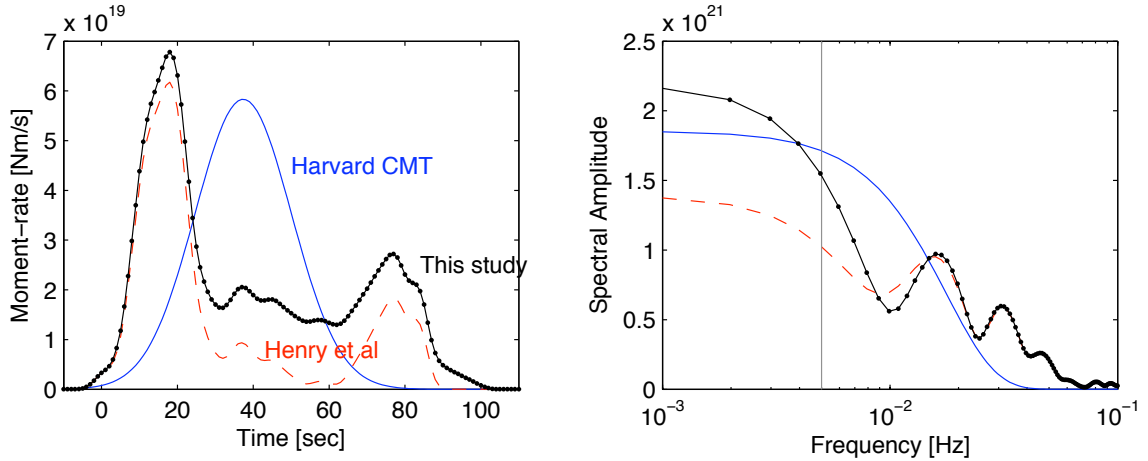


Figure 4.13: Moment-rate functions for the models presented, both in time domain and frequency domain. The vertical gray line is at 200 seconds, indicating that at that period we are still not at the flat part of the spectrum.

the India earthquake (see chapter 2), indicating that we cannot expect much improvement relative to this model at periods between 100 and 500 seconds.

As the modified source model has continuous slip on one fault plane, it is by some measure the simplest model that has been shown to fit both the body waves and the long-period surface waves. The model by *Kuge et al.* (1999) is composed of five nearly pure strike-slip events, the first three corresponding to the first subevent in this study, and the last two corresponding to the second subevent. In order to fit the non double-couple component they add three normal faulting subevents, with long rupture duration, at the ends of the strike-slip events. The long duration is needed to reduce the body-wave radiation from the normal subevents, as they are much more efficient at radiating far-field P-waves than strike-slip subevents. In this model there is a 60 km gap between the two clusters of subevents. This setting is explained in terms of a series of en echelon strike-slip faults connected by normal faulting events. Other researchers (*Nettles et al.*, 1999) also model the event as five nearly pure strikes-slip events, but point out that the second two have a $10 \pm 5^\circ$ counterclockwise rotation in strike, going from 281° to 271° , relative to the first three. They suggest this could indicate a curved fault or two faults slightly offset from each other. They make no attempt at explaining the non double-couple component, and by comparison to the study of *Kuge et al.* (1999) and *Henry et al.* (2000) it is unlikely that this purely strike-slip solution would explain the long-period data. By using finite fault modeling of

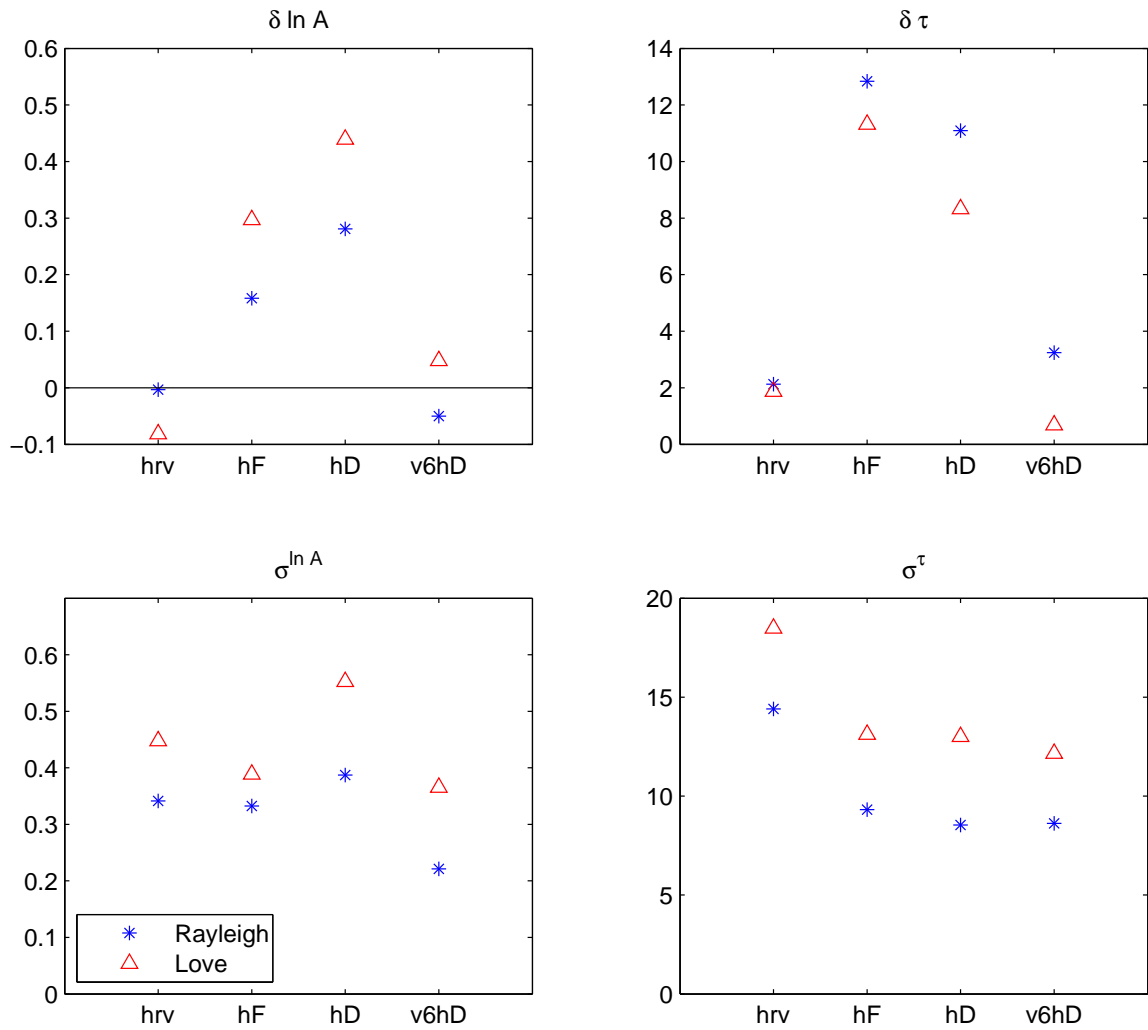


Figure 4.14: Multitaper measurements averaged over all azimuths and over a band between 100 and 500 seconds. The models are the Havard CMT (hrv), the finite source model with focal mechanism HenryF (hF), the finite source model with focal mechanism HenryD (hD) and the modified finite model with focal mechanism HenryD (v6hD).

body waves, *Antolik et al.* (2000) suggest that the non double-couple component of the Harvard CMT can be explained by compound rupture on two faults: one nearly pure strike slip fault, consistent with the first motions, and the other an oblique normal fault rotated $\sim 25^\circ$ relative to the first. Both *Antolik et al.* (2000) and *Henry et al.* (2000) point out that the first motions of the P-wave require that the rupture started as nearly pure strike-slip.

It may seem somewhat puzzling, tectonically, that a 300 km narrow intraplate fault could have a dip and rake as large as suggested by the surface wave modeling. As described above, other studies have suggested a combination of normal faulting and strike-slip faulting to explain the surface-wave radiation, although those have been aimed at explaining the non double-couple component of the Harvard CMT which we find consistent with the surface-wave data, albeit not necessary.

4.6 Conclusions

We have compared the observed surface waves for the Balleny Islands event to those computed for four different source models: one surface-wave point-source model (HarvardCMT), one finite fault model with two different fault orientations (HenryD and HenryF) and one finite model combining model HenryD and a smooth component of slip extending over the whole fault in space and time, propagating unilaterally along the fault. We have shown that by adding this component of slip we can significantly improve the fits to the amplitude and phase of surface waves. The modified body-wave model provides reasonable fits to the long-period surface waves, as well as the body waves, without invoking slip on multiple fault planes, or on unconnected fault patches. The continuity of slip indicates that this event can be explained by standard fracture mechanics models where the rupture is driven by the stress concentration at the crack tip. We have only proven the existence of such a model, not its uniqueness. We present this as the simplest model that gives a reasonable match to a wide range of data sets, although a more segmented rupture cannot be ruled out.

This study emphasizes the importance of including long-period waves in finite fault modeling. The most basic approach is to constrain the models to have the correct moment, centroid time and location. Here we further match the azimuthal amplitude pattern due to the directivity of the rupture. Care has to be taken to use waves that have periods several times longer than the duration of the source to estimate the point-source parameters. By

combining the body-wave modeling with the surface-wave modeling we retain both the robustness of the surface waves and the detail of the body waves.

Chapter 5

The 2004 Sumatra, Indonesia earthquake

5.1 Introduction

The December 26th, 2004 Sumatra, Indonesia earthquake is the largest event occurring in the last 40 years, and it caused immeasurable death and destruction. It is also the largest event to be recorded on modern broadband instruments. However, there has been a debate as to how big the event is and as to the duration of slip. Here we detail some of the modeling that took place early on, and show how by looking at different parts of the spectrum one can get a different estimate of the size and duration.

5.2 Constraints from long-period surface waves

5.2.1 Data and processing

We obtain 6 hours of data from from the IRIS data center (<http://www.iris.edu>), recorded on instruments with corner period above 300 seconds We have taken care to discard data from stations showing non-linear response due to the large amplitudes involved. We computed long-period seismograms for several available source models. We perform two sets of simulations for each source model, one using the SEM method as in previous chapters (*Komatitsch and Tromp, 2002a*), and one using normal mode summation. This is necessary since the SEM method uses an approximate method for incorporating self-gravitation, the Cowling approximation, and that causes significant errors, particularly in phase, at periods above 800 seconds. We compare vertical component data and synthetics in several pass-

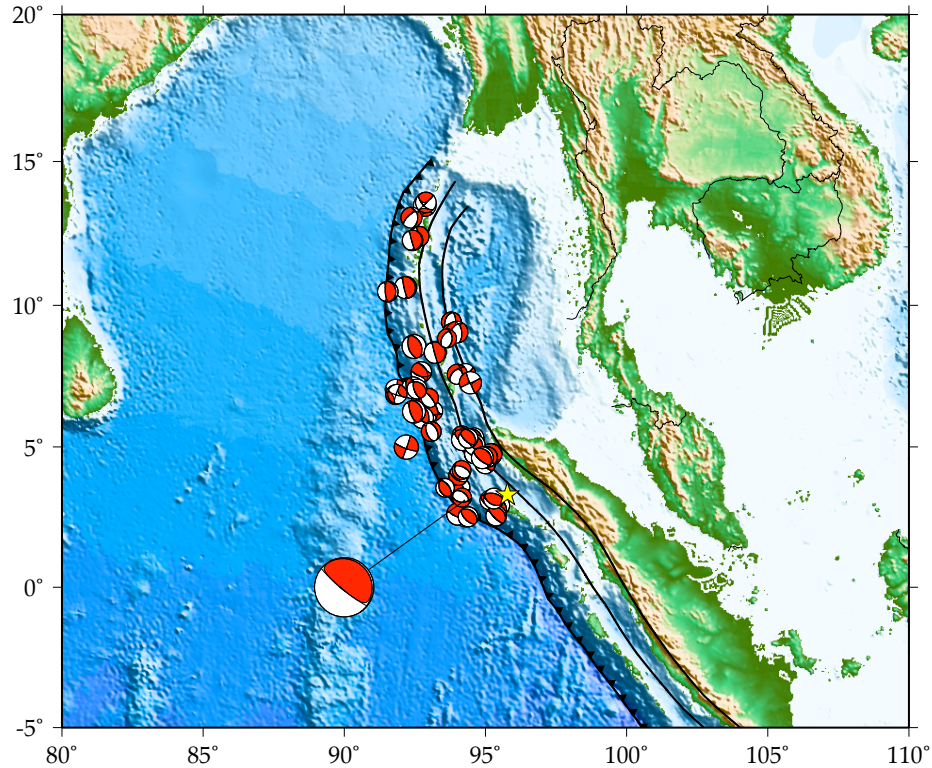


Figure 5.1: Topography/Bathymetry in the region of the great 2004 Sumatra earthquake. Shown are the Harvard CMT estimates in the first month after the earthquake. The CMT for the main event is shown with the large beach ball. Note that the aftershocks extend almost to 15°North. Also note that the centroid is located very close to the southern end of the aftershock zone, and the hypocenter. The black lines are 50 and 100 km depth slab contours (*Gudmundsson and Sambridge, 1998*).

bands to estimate how well the different source models reproduce the observations. In each passband we take the envelope of the traces (data and synthetics), select a window around the surface wave, pick the maximum amplitude of the envelope within that window, and measure the ratio of the amplitude of data and synthetics. We also measure the time shift between data and synthetics using cross-correlation, for each passband.

5.2.2 Harvard CMT and preliminary finite-fault model

The Harvard CMT solution was published very shortly after the event. This point source solution is close to the epicenter (within 1.5°). About a week after the event a preliminary finite fault model, based on modeling of P- and S-waves, was published (*Ji, 2005*). The finite fault model (Fig. 5.2) has a similar moment and location of maximum slip as the Harvard

CMT and prescribes slip on a 400 km long fault. The model suggests nearly unilateral propagation to the north and up dip.

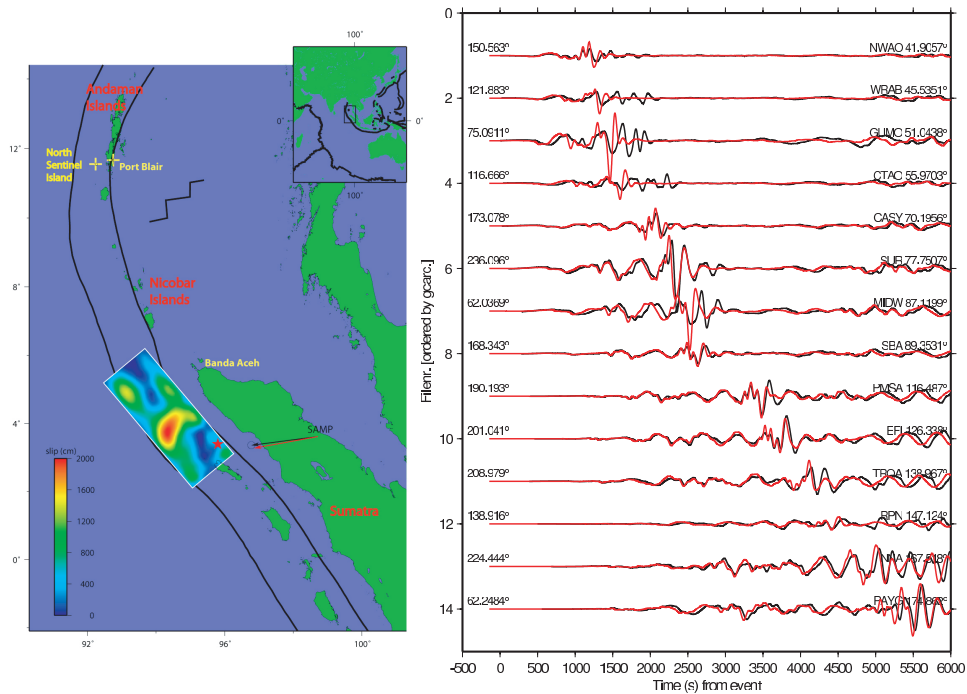


Figure 5.2: Left: Slip distribution (*Ji*, 2005) for a preliminary finite fault model. Right: Observed (black) and computed (red) waveforms for the preliminary source model. Shown are waveforms in southward azimuths, which are the most difficult azimuths to fit. The waveforms are normalized by $\sqrt{\sin \Delta}$, where Δ is the great circle arc distance between data and stations, to correct for the geometrical spreading of the surface waves. The azimuth is shown with numbers on the left and Δ is shown next to the station name on the right.

We compute synthetics for both the Harvard CMT and the preliminary slip model. The preliminary slip model shows reasonably good fits to the surface waves in the passband 200–500 seconds (Fig. 5.2). Although the synthetic waveforms in some azimuths have significantly shorter duration than observed, for example GUMO (Guam) and WRAB (Western Australia) others have not, for example EFI (Falkland Islands) and NNA (Peru). The spatial extent of the fault plane for the preliminary slip model is substantially smaller than the aftershock area (see f.ex. Fig. 5.1). Furthermore, we received reports on significant uplift at Port Blair in the Andaman Islands, about 600 km north of the end of the preliminary slip mode (from various websites, collected by Roger Bilham and later published in *Bilham et al.* (2005)). These observations, in particular the observations of uplift in the Andaman Islands, seem contradictory to the preliminary slip model (*Ji*, 2005). This model is based

on the first 200 seconds of the P-wave train. After that time other phases (e.g., PP) arrive, and modeling using just body waves becomes difficult (see for example *Ammon et al.* (2005), Model I), unless the other phases are accurately accounted for. Since the north bound of the fault is selected based on the length of the time window between the arrivals of the P-wave and the PP-wave there is no reason to believe that there is no slip further north. However, as the finite fault model does a relatively good job of explaining the overall amplitude and phase of the 200–500 seconds surface waves, one could conclude that there was not significant slip further north, exciting waves at these periods.

In order to see if the preliminary slip model, and the Harvard CMT, can predict the waveforms in other period bands, we compare the amplitude ratios of data and synthetics and the time shifts between them at different periods (as detailed in section 5.2.1). The results are shown in Fig. 5.3.

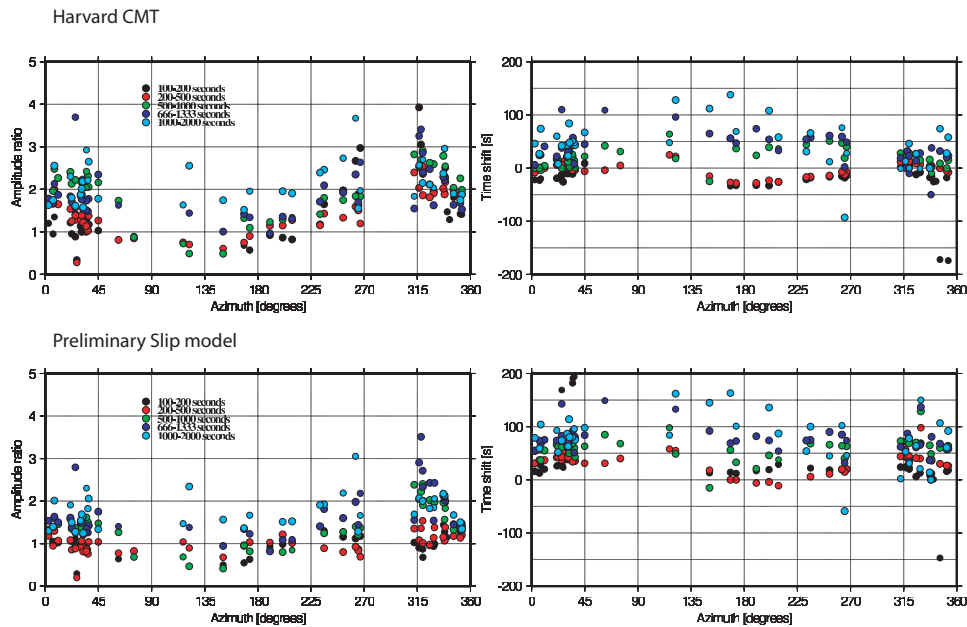


Figure 5.3: Amplitude ratios (left) and time shifts (right) for the Harvard CMT (top) and the preliminary slip model (bottom). A model that can accurately describe the data will have amplitude ratios of unity and zero time shifts. Amplitude anomalies larger than unity indicate larger data than synthetics, and positive indicate earlier arrivals in synthetics than data. Shown are measurements for data and synthetics filtered in different band-passes. It can be seen that both models predict the shorter periods better than the longer periods.

Focusing first on the results from the Harvard CMT, we can see that the overall amplitude of the surface waves are well matched at periods of 100–500 seconds, although there

is a large amount of directivity, such that data in northwestward azimuths is larger than synthetics, and smaller in southeastward azimuths. The overall amplitude ratio at 1000–2000 seconds is close to two. The time shifts at 100–500 seconds are close to zero, as to be expected since that is the period band that is used to estimate the Harvard CMT. For longer period data there are time shifts of up to 50–100 seconds observed.

The preliminary finite-fault model has overall amplitude ratios of data and synthetics close to unity for periods of 100–1000 seconds. The amplitude ratios at longer periods are larger, in the range of 1.5 to 2. The time shifts show a similar pattern as those measured for the Harvard CMT, although a little larger on average. This shows that in order to obtain an accurate slip model for this earthquake, we need to look at the very long-period data, those with periods of 1000 seconds and longer.

The discrepancy between the fault area of the model, and the fault area suggested by aftershocks and subsidence in the Andamans, in addition to the “frequency dependence” of the moment as interpreted from figures similar to Fig. 5.6 led to the idea that the slip in the northern part was somehow slow, either with a small rupture speed or long rise time. Slow slip could accommodate slip on a larger area without exciting seismic waves in the period band of 200-500 seconds.

5.2.3 Final slip models

The very long duration of the earthquake makes traditional body-wave modeling difficult. In order to match the long period slip during the earthquake, surface waves have to be included in the inversion. Two models based on surface waves are published in *Ammon et al.* (2005). The first (Model II, from Hong-Kie Thio) is based entirely on surface waves, and the second (Model III, from Chen Ji) is based on body waves, short-period surface waves from four nearby stations and long-period surface waves from the global network. Model III is a later iteration of the preliminary model presented in the last section, and changed over time as successive iterations were shown not to match the long-period surface waves (this study) and/or the excitation of the Earth’s normal modes (work by Alex Song, published in part in *Park et al.* (2005)). Since the surface waves are now being used to construct the models, it is not a surprise that the resulting synthetics fit the data very well. The slip models, and their corresponding waveforms, are shown in Fig. 5.4 and Fig. 5.5.

The frequency dependent amplitude ratios and time shifts for both models are shown

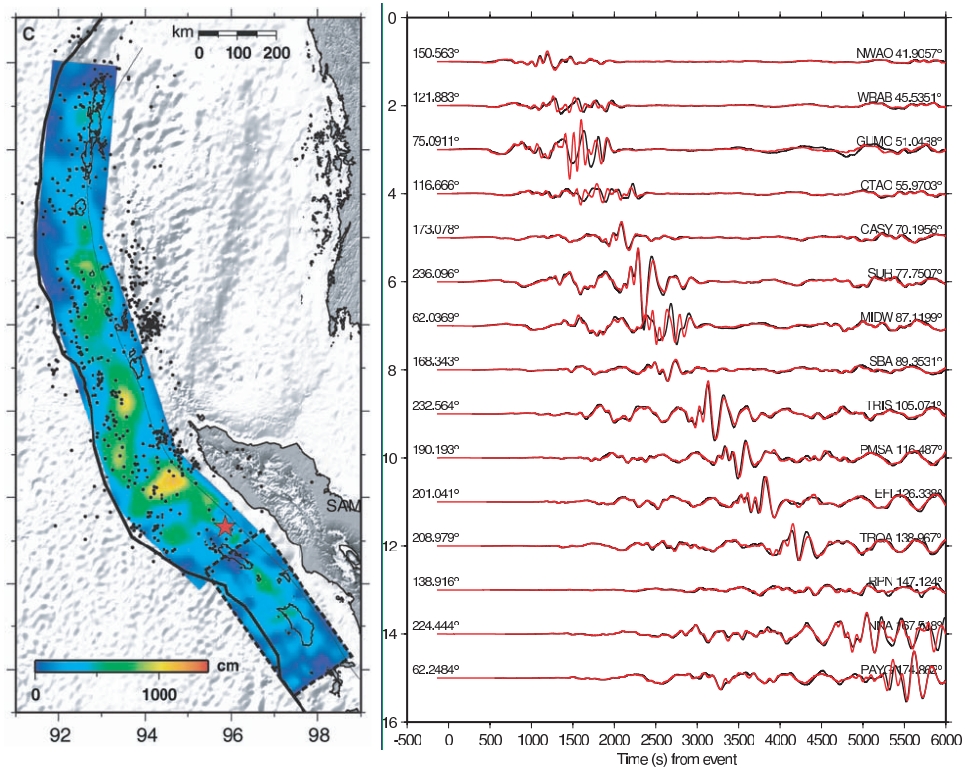


Figure 5.4: Slip distribution obtained from body-waves and surface waves (*Ammon et al.* (2005), Model III), and predicted waveforms. Compare to Fig. 5.2.

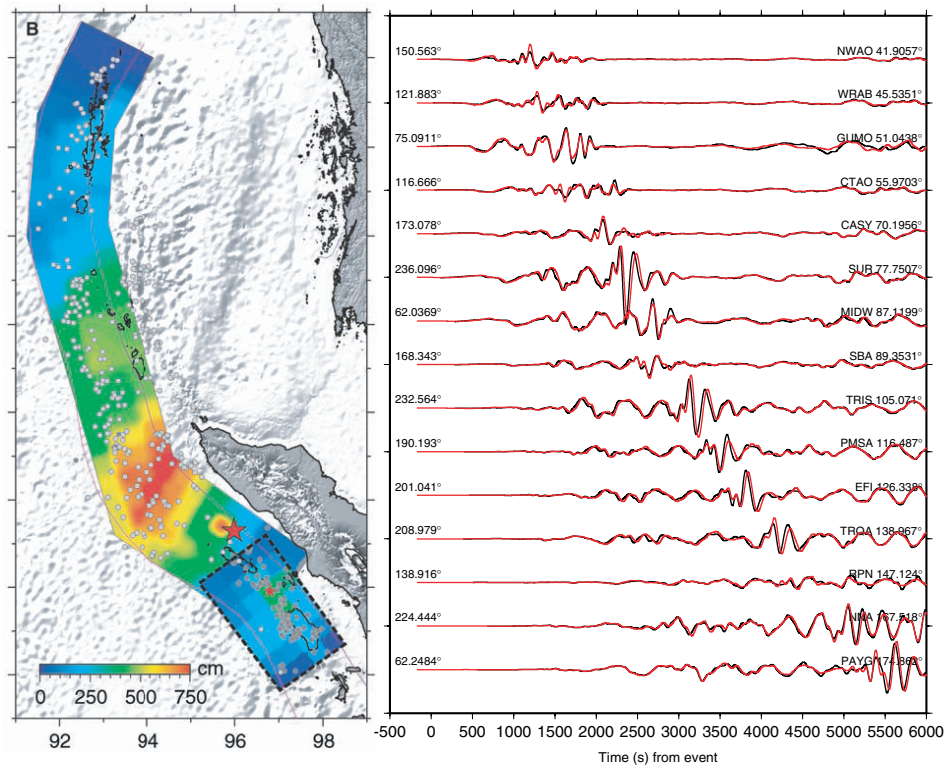


Figure 5.5: Slip distribution obtained from surface waves (*Ammon et al.* (2005), model II) and predicted waveforms. Compare to Fig. 5.2 and Fig. 5.4.

in Fig. 5.3. Both models provide good matches to the observed data. The two surface

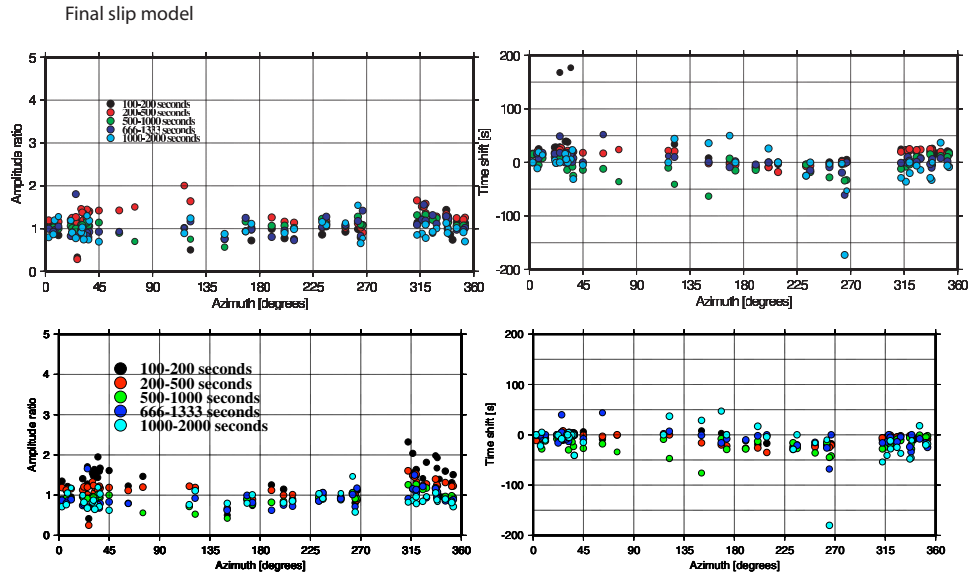


Figure 5.6: Amplitude ratios and time shifts for the final source models, *Ammon et al.* (2005), Model III (top) and Model II (bottom). Compare to Fig. 5.3.

wave models have been shown to match the excitation of the Earth’s normal modes (*Park et al.*, 2005). As shown in previous chapters of this thesis, we have to look at periods that are significantly longer than the duration of the earthquake to estimate if all the slip is accounted for in the models. The moment-rate function for Model III and its spectra are shown in Fig. 5.7. By comparing the synthetic wave-form and the moment-rate function, we see that multiple phases other than the direct P-wave arrive within the duration of the source. As a result of this, traditional body-wave modeling can not be used reliably. We also see that the flat portion of the spectra is at periods of 1000 seconds or longer for this model.

5.3 Constraints from GPS measurements

In the last section we showed how the source models changed as we successively looked at longer and longer periods. The ultimate long-period part of the spectrum is the static field. For this giant earthquake static offsets were recorded on GPS receivers at very large distances, up to thousands of kilometers away (*Banerjee et al.*, 2005). The long-period surface waves were used to obtain the source models, and therefore the comparison of

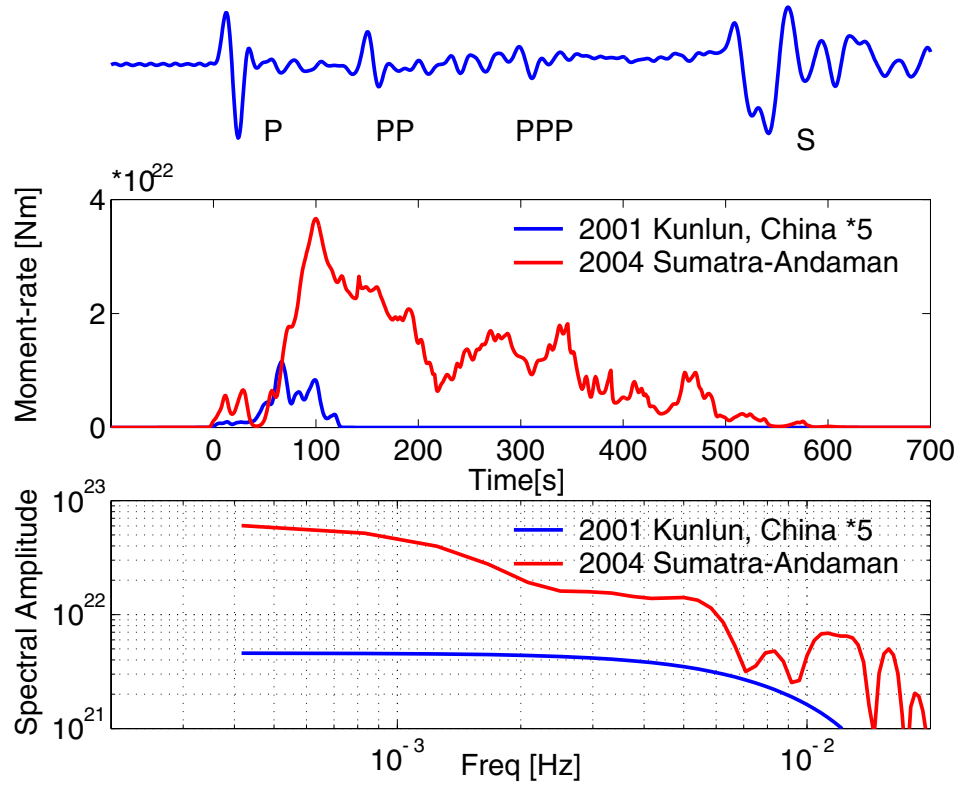


Figure 5.7: The top trace shows a mode-summation synthetic seismogram, for an event with the mechanism of the Harvard CMT, but a short source duration, at a distance of 60° . The central panel depicts the moment rate function for model III (*Ammon et al.*, 2005) on the same time scale as the trace above. For comparison we show the moment-rate function for the 2001 Kunlun earthquake, multiplied by 5. The bottom panel shows the spectral amplitudes of the two moment-rate functions shown in the central panel.

those to data do not provide an independent estimate of the quality of the source models. However, we can test the models by checking their predictions to a new data set, the static offsets.

Traditionally, in geodetic modeling, uniform or layered half-space structural models have been used to invert for the slip on a given fault plane. To explain offsets from great earthquakes at very large distances spherical models are needed (*Banerjee et al.*, 2005). In the previous section we used the spectral element method (SEM) to compute 3D global seismograms (*Komatitsch and Tromp*, 2002a). The method computes the full wave field, and therefore includes the static field “for free.” Here we show how one can estimate the static field from the SEM simulations, and apply the method to several source models produced for the Sumatra earthquake. Using this method we can compute static offsets for a model that incorporates the Earth’s topography, ellipticity and 3D elastic structure.

5.3.1 Data and modeling

Two studies estimate the static field from the earthquake (*Banerjee et al.*, 2005; *Vigny et al.*, 2005). These are difficult measurements and several factors can influence the estimates. Both studies use data from the continuous IGS network, in addition to other data. The first mentioned study estimates the offsets by differencing the averages measured over five days before the earthquake and five days after the earthquake, whereas the latter uses one-day averages. As we expect some postseismic motion, this time difference can influence the estimates of the offsets.

We compute the dynamic field for the entire globe, a total of 100 minutes. The dynamic field includes the static component as shown in Fig. 5.8. In order to estimate the static displacement, we take the average displacement at times between 2000 and 4000 seconds after the initiation of rupture. The start time is chosen to correspond to the time that most of the first-arrival waves have passed, and the end time is such that the second arrival waves have not yet arrived. If the static displacements are very small, the contribution from the waves may be significant, so we only attribute significance to estimates larger than 1 mm. In order to minimize the effect of high frequency waves on the measurements, we alter the time history of the models, such that all the subsources comprising the model, start off at the same time, with a long rise time (200 seconds). As we are looking at the static component the time history of the source does not impact our results.

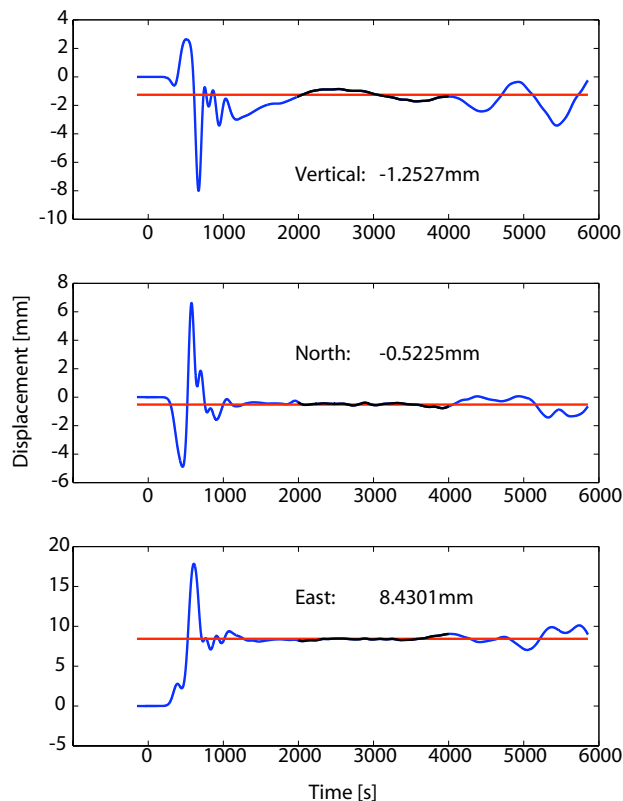


Figure 5.8: Example of estimating the static field from the seismograms. The unfiltered seismogram from the forward run (blue), the time window used for estimating the static offset (black) and the estimated offset (red), for the three components at station IISC.

5.3.2 Results

We compute the static offsets for three source-models; the two finite-fault models presented above (*Ammon et al.*, 2005) and a slip model derived from static offsets in the near field (*Chlieh et al.*, 2007). The first thing to note is that there is a relatively big difference between the data themselves. The largest motions in the far-field are seen to the east and to the west. As we are strictly modeling the coseismic displacements, one would expect the predicted offsets to be closer to the estimate by *Vigny et al.* (2005) than *Banerjee et al.* (2005), as they use a shorter averaging time after the earthquake to obtain the offsets, reducing the influence of postseismic motions. In fact, both *Ammon et al.* (2005) model II and III have slightly smaller predictions than observed by *Vigny et al.* (2005), which are in turn smaller than those estimated by *Banerjee et al.* (2005). The model based on static data predicts, generally, slightly larger motions than the seismic models.

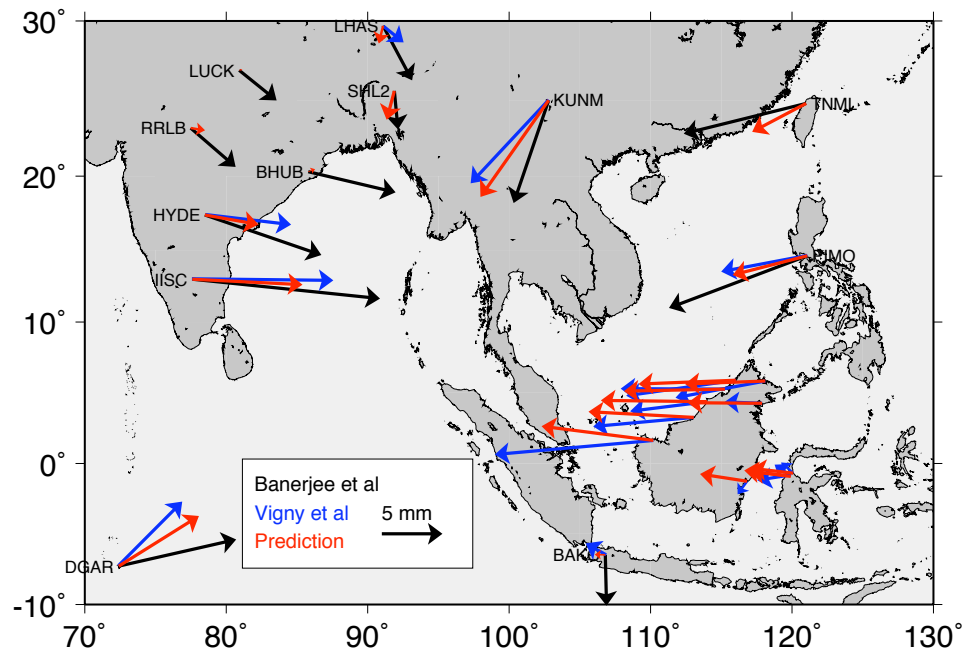


Figure 5.9: Observed (blue and black) and computed (red) static displacements for the combined body-wave and surface-wave model *Ammon et al.* (2005), model III. The two data sets represent data processed by different authors.

5.4 Discussion and conclusions

We have shown how the preliminary finite-fault models failed at predicting the very long-period surface waves, and how a modified model (model III) could match body waves, short-period and long-period surface waves, the Earth's normal modes and far-field static offsets. Tsunami data can also be explained by slip models with similar moments (*Fujii and Satake, 2007; Piatanesi and Lorito, 2007*), although some tsunami researchers advocate slip with a tsunami component (*Seno and Hirata, 2007*). By combining modern broadband records and a wide suite of modeling techniques we obtain a model for the great Sumatra earthquake that is self-consistent over the seismic frequency band. This model involves rupture propagation at a speed on the order of 2.5 km/s and rise times on the order of 20 seconds.

However, our preferred model (model III) has been shown (*Chlieh et al., 2007*) to severely underpredict the near-field static offsets. Part of this discrepancy can be explained by post-seismic motion in the month following the event. Models based on purely static data predict larger slip, in particular in the Nicobar and Andaman segments, and at shallower depths.

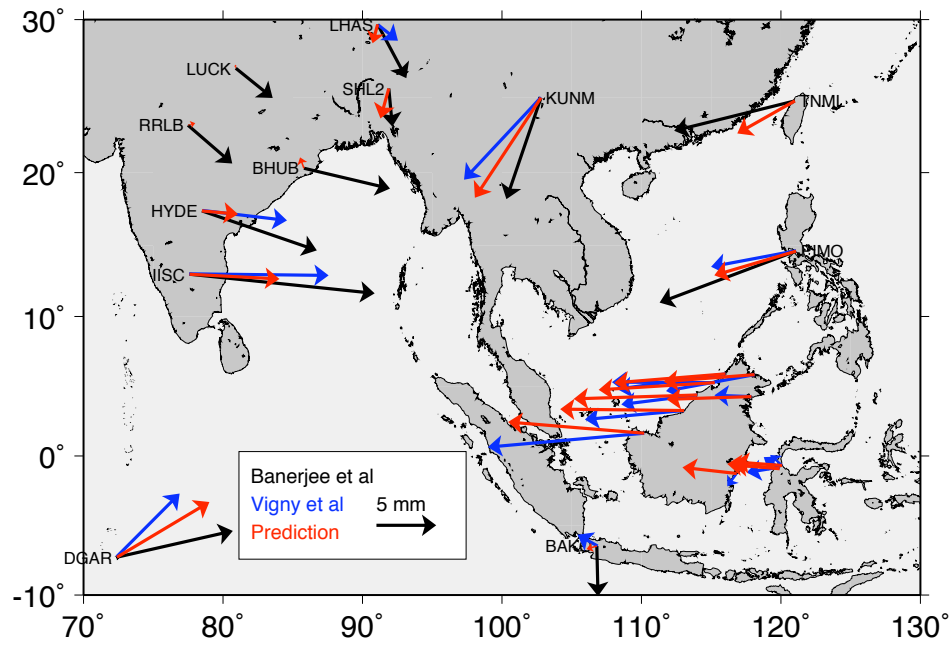


Figure 5.10: Same as Fig. 5.9, with model predictions by *Ammon et al.* (2005), model II. We note that the predicted offsets are somewhat smaller than for model III.

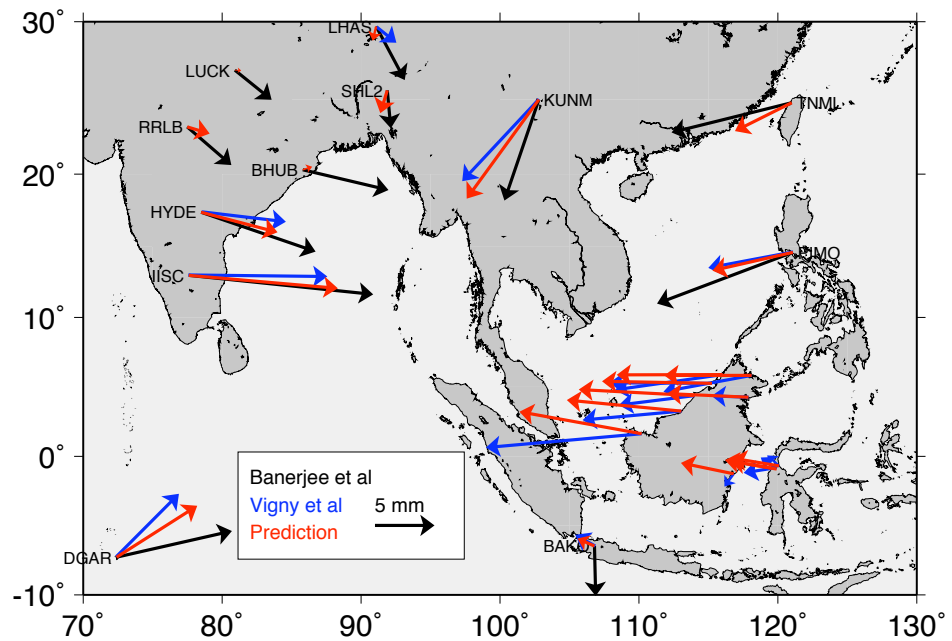


Figure 5.11: Same as Fig. 5.9 with model prediction for a static source model (*Chlieh et al.* (2007), model G.)

The seismic model is not very sensitive to the location of slip down dip, and although not shown here, a large part of the remaining discrepancy could be removed by shifting the slip up dip and making it more compact, while keeping the moment constant, similar to the models presented in (*Chlieh et al.*, 2007). The geodetic data above the fault plane are point measurements, and without the constraint on the moment from seismological data, it is difficult to know how to distribute the slip on the fault plane, between the data points. However, this illustrates how difficult it can be to model the seismic source, and how adding one data set can change seemingly robust results significantly. We emphasize the importance of using multiple data sets for seismic source modeling, and that caution should be exercised when interpreting the details of the models.

5.5 Acknowledgements

The work presented in this chapter was done in close collaboration with Chen Ji, Mohamed Chlieh and Hiroo Kanamori, and was published in part in *Ammon et al.* (2005) and *Chlieh et al.* (2007).

Chapter 6

Adjoint source inversions

6.1 Introduction

As we have seen in previous chapters, the seismic source inverse problem has many trade-offs, and the result of an inversion can change significantly depending on the data set used. The entire waveform contains information about the earthquake source, but in order to minimize the effects of errors in 3D structural parameters, only selected parts are used in most analyses, e.g. body waves and long-period surface waves. By accurately accounting for 3D structure one can use a larger portion of the seismogram to determine the source parameters, thereby reducing trade-offs. In the previous chapters we have shown how this can be accomplished in a forward modeling sense, but now we focus our attention on how we can use the 3D synthetics to invert for source models in an efficient way. As computing accurate broad-band synthetics for a 3D Earth is still expensive, we wish to use a method that limits the number of simulations.

Adjoint methods to obtain structural models were introduced into seismology by *Tarantola* (1984). He shows how, in the acoustic approximation, the gradient of a misfit function can be estimated by propagating the residuals between data and synthetics backward in time. By stepping in the direction of the gradient he iteratively solves for a structural model. He also gives an expression for the updated source time function in terms of the time-reversed wave field. Later studies (*Gauthier et al.*, 1986; *Tarantola*, 1987, 1988) focused on developing and applying the method to improve structural models. A more general description of adjoint methods was given by *Talagrand and Courtier* (1987). An example of estimating the magnitude and direction of a point force, using an adjoint method in combination with a conjugate gradient method, is given by *Tromp et al.* (2005), and an

example of the source-location problem in 2D is given by *Tape et al.* (2007).

The first step of the adjoint method is the back-propagation of the difference between data and synthetics. An initial estimate can be given by the “zero” model, thus back-propagating the data, reversed in time. This step in and of itself is known as “time-reversal imaging”. *McMechan* (1982) illustrates how in an exploration geophysics setting point sources and line sources can be located by back-propagating the recorded data in a synthetic model. In a later study this method is applied to data from the Long Valley caldera in California (*McMechan et al.*, 1985). An example of application to a synthetic finite source is given by *Chang and McMechan* (1991). *Gajewski and Tessmer* (2005) apply time-reversal imaging to synthetic data, emphasizing the ability of this method to locate events without picking phases. Time-reversal imaging has also been used to determine the duration and extent of the 2004 Sumatra earthquake by back-propagating long-period global surface waves (*Larmat et al.*, 2006). To interpret the time-reversed field in terms of a finite source they deconvolve the time-reversed field from a smaller event from that of the main event.

Several studies have focused on the experimental side of time-reversal imaging, which is often referred to as “time-reversal acoustics” or “time-reversal mirrors” (for an overview see *Fink*, 1997). The experiments include a source that sends waves through complex media, and receivers that can retransmit the signal reversed in time such that the waves refocus on the source. The method has been applied successfully in the laboratory and in the ocean.

6.2 Theory

In any modeling process we wish to find a model that can reproduce the observed data. The first question to ask is how to quantify the similarity of the model prediction and the data. In body-wave source modeling it is common practice to use the waveform misfit function (*Nolet*, 1987), or the squared difference between data \mathbf{d} and synthetics \mathbf{s} , recorded at receivers r located at \mathbf{x}_r , integrated over a time window $[0, T]$:

$$\chi(\mathbf{m}) = \frac{1}{2} \sum_{r=1}^N \int_0^T \|\mathbf{s}(\mathbf{x}_r, t, \mathbf{m}) - \mathbf{d}(\mathbf{x}_r, t)\|^2 dt. \quad (6.1)$$

We wish to find the minimum of this function with respect to the model parameters. As shown by *Tarantola* (1984, 1987, 1988) the gradient of this function can be estimated numerically, given a model vector \mathbf{m} , and then one can iteratively take steps towards the minimum. The gradient with respect to the model parameters can be written as:

$$\delta\chi = \sum_{r=1}^N \int_0^T [\mathbf{s}(\mathbf{x}_r, t, \mathbf{m}) - \mathbf{d}(\mathbf{x}_r, t)] \cdot \delta\mathbf{s}(\mathbf{x}_r, t, \mathbf{m}) dt \quad (6.2)$$

We are interested in a source inversion, so the model parameters can be written as a distributed moment-tensor source $\mathbf{m}(\mathbf{x}, t)$ on a fault plane Σ . The surface-density moment tensor is given by (*Dahlen and Tromp*, 1998):

$$\mathbf{m} = \mu\Delta s(\hat{\boldsymbol{\sigma}}\hat{\boldsymbol{\nu}} + \hat{\boldsymbol{\nu}}\hat{\boldsymbol{\sigma}}), \quad (6.3)$$

where μ is the shear modulus, Δs is the magnitude of the slip vector, $\hat{\boldsymbol{\sigma}}$ is the slip direction and $\hat{\boldsymbol{\nu}}$ is the fault normal. It is of convenience to define the distributed moment-tensor source in the volume V ;

$$\tilde{\mathbf{m}}(\mathbf{x}, t) = \mathbf{m}(\mathbf{x}_s, t)\delta(\mathbf{x} - \mathbf{x}_s), \quad (6.4)$$

where $\mathbf{x}_s \in \Sigma$. The i th component of the response can be written as (*Aki and Richards*, 1980; *Dahlen and Tromp*, 1998):

$$s_i(\mathbf{x}, t) = \int_0^t \int_{\Sigma} \partial'_j G_{ik}(\mathbf{x}, \mathbf{x}'; t - t') m_{jk}(\mathbf{x}', t') d^2 x' dt' \quad (6.5)$$

$$= \int_0^t \int_V \partial'_j G_{ik}(\mathbf{x}, \mathbf{x}'; t - t') \tilde{m}_{jk}(\mathbf{x}', t') d^3 x' dt', \quad (6.6)$$

where $\mathbf{G}(\mathbf{x}, \mathbf{x}'; t - t')$ is the Green's function response due to a point force. The change in the response $\delta s_i(\mathbf{x}, t)$ with respect to the model parameters then is:

$$\delta s_i(\mathbf{x}, t) = \int_0^t \int_V \partial'_j G_{ik}(\mathbf{x}, \mathbf{x}'; t - t') \delta \tilde{m}_{jk}(\mathbf{x}', t') d^3 x' dt'. \quad (6.7)$$

Substituting the expression for $\delta s_i(\mathbf{x}, t)$ into Eq. 6.2, and changing the order of integration we get

$$\delta\chi = \sum_{r=1}^N \int_0^T \int_V \int_{t'}^T [s_i(\mathbf{x}_r, t) - d_i(\mathbf{x}_r, t)] \partial'_j G_{ik}(\mathbf{x}, \mathbf{x}'; t - t') \delta \tilde{m}_{jk}(\mathbf{x}', t') d^3 x' dt dt'. \quad (6.8)$$

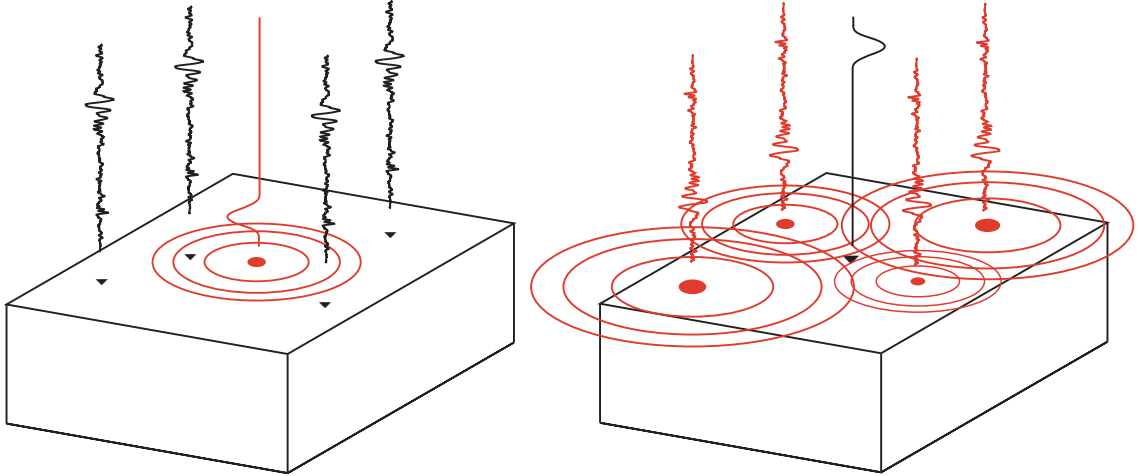


Figure 6.1: A forward simulation on the left, contrasted with an adjoint simulation on the right. In a forward simulation, the source-time function is inserted at the location of the source, and the resulting wave field is recorded at the receiver. In the adjoint simulation, the time-reversed difference between data and synthetics is inserted at the location of the receiver, as a force, and the resulting wave field, the adjoint wave field, is recorded at the location of the initial source. Setting the synthetics to zero, and back-propagating the data directly (as pictured here) is referred to as time-reversal imaging.

Tromp et al. (2005) define the *waveform adjoint source* as:

$$f_i^\dagger(\mathbf{x}, t) = \sum_{r=1}^N [s_i(\mathbf{x}_r, T - t) - d_i(\mathbf{x}_r, T - t)] \delta(\mathbf{x} - \mathbf{x}_r), \quad (6.9)$$

and the resulting *waveform adjoint field* as the field that is generated by this source:

$$s_k^\dagger(\mathbf{x}', t') = \int_0^{t'} \int_V G_{ki}(\mathbf{x}', \mathbf{x}; t' - t) f_i^\dagger(\mathbf{x}, t) d^3 \mathbf{x} dt. \quad (6.10)$$

By change of variables, and invoking the reciprocity of the Green's function, they show that we can write

$$s_k^\dagger(\mathbf{x}', T - t') = \sum_{r=1}^N \int_{t'}^T [s_i(\mathbf{x}_r, t) - d_i(\mathbf{x}_r, t)] \partial'_j G_{ik}(\mathbf{x}, \mathbf{x}'; t - t') dt. \quad (6.11)$$

By substituting this result into Eq. 6.8, and dropping the primes, we get

$$\delta\chi = \int_0^T \int_V \partial_j s_k^\dagger(\mathbf{x}, T - t) \delta \tilde{m}_{jk}(\mathbf{x}, t) d^3 \mathbf{x} dt. \quad (6.12)$$

In vector format

$$\delta\chi = \int_0^T \int_V \nabla \mathbf{s}^\dagger(\mathbf{x}, T-t) : \delta \tilde{\mathbf{m}}(\mathbf{x}, t) d^3 \mathbf{x} dt. \quad (6.13)$$

Using the symmetry of the moment tensor we finally obtain:

$$\delta\chi = \int_0^T \int_V \boldsymbol{\epsilon}^\dagger(\mathbf{x}, T-t) : \delta \tilde{\mathbf{m}}(\mathbf{x}, t) d^3 \mathbf{x} dt \quad (6.14)$$

where we have defined $\boldsymbol{\epsilon}^\dagger = \frac{1}{2}[\nabla \mathbf{s} + (\nabla \mathbf{s})^T]$, which we will refer to as the *adjoint strain*. If we assume that the moment density is confined to a fault plane Σ , and only the moment-density is perturbed, not the fault plane, such that $\delta \tilde{\mathbf{m}}(\mathbf{x}, t) = \delta \mathbf{m}(\mathbf{x}_s, t) \delta(\mathbf{x} - \mathbf{x}_s)$, then we get the result presented by *Tromp et al.* (2005):

$$\delta\chi = \int_0^T \int_\Sigma \boldsymbol{\epsilon}^\dagger(\mathbf{x}_s, T-t) : \delta \mathbf{m}(\mathbf{x}_s, t) d^2 \mathbf{x} dt, \quad (6.15)$$

where $\mathbf{x}_s \in \Sigma$. This equation shows that the adjoint strain tells us in which direction in parameter space to go in order to obtain a better source model.

It can be difficult to visualize the result of integrating the adjoint strain multiplied by the source-time history, which can, generally, be described by a step-like function (such as a Heaviside function or an error function). Another way of writing Eq. 6.15 is obtained by integrating by parts:

$$\delta\chi = [I(\boldsymbol{\epsilon}^\dagger)(\mathbf{x}_s, T-t) : \delta \mathbf{m}(\mathbf{x}_s, t)]_0^T + \int_0^T \int_\Sigma I(\boldsymbol{\epsilon}^\dagger)(\mathbf{x}_s, T-t) : \delta \dot{\mathbf{m}}(\mathbf{x}_s, t) d^2 \mathbf{x} dt, \quad (6.16)$$

where $I(\boldsymbol{\epsilon}^\dagger)(\mathbf{x}, t) = \int_{-\infty}^t \boldsymbol{\epsilon}^\dagger(\mathbf{x}, t') dt'$. We can make the first term vanish by choosing $t=0$ before the initiation of the source, and then $\mathbf{m}(\mathbf{x}, 0) = 0$.

We can also allow for a perturbation in the location of the fault plane $h(\mathbf{x}_s)$, in the direction of the fault normal $\hat{\nu}$. Then we get another term accounting for the mislocation of the fault plane:

$$\delta \dot{\mathbf{m}}(\mathbf{x}, t) = \delta \dot{\mathbf{m}}(\mathbf{x}, t) \delta(\mathbf{x} - \mathbf{x}_s) + \dot{\mathbf{m}}(\mathbf{x}, t) \delta h(\mathbf{x}_s) \partial_\nu \delta(\mathbf{x} - \mathbf{x}_s), \quad (6.17)$$

and the change in misfit becomes:

$$\delta\chi = \int_0^T \int_\Sigma I(\boldsymbol{\epsilon}^\dagger)(\mathbf{x}_s, T-t) : \delta \dot{\mathbf{m}}(\mathbf{x}_s, t) d^2 \mathbf{x} dt + \int_0^T \int_\Sigma \partial_\nu I(\boldsymbol{\epsilon}^\dagger)(\mathbf{x}_s, t) : \dot{\mathbf{m}}(\mathbf{x}_s, t) d^2 \mathbf{x} dt. \quad (6.18)$$

Note that in order to update the location of the fault plane we monitor the directional derivative of the strain across the fault plane. The contraction with \mathbf{m} ensures that only the strains corresponding to large moment-tensor elements contribute to the change in misfit.

For a point source in space, with time dependence $S(t - t_s)$ we write $\dot{\mathbf{m}}(\mathbf{x}, t) = \mathbf{M}\delta(\mathbf{x} - \mathbf{x}_s)\dot{S}(t - t_s)$. Now the change in the moment density with respect to the source parameters $(\mathbf{M}, \mathbf{x}_s, t_s)$ is:

$$\delta\dot{\mathbf{m}}(\mathbf{x}, t) = \delta\mathbf{M}\delta(\mathbf{x} - \mathbf{x}_s)\dot{S}(t - t_s) + \delta\mathbf{x}_s \cdot \nabla\delta(\mathbf{x} - \mathbf{x}_s)\mathbf{M}\dot{S}(t - t_s) - \delta t_s\mathbf{M}\delta(\mathbf{x} - \mathbf{x}_s)\ddot{S}(t - t_s), \quad (6.19)$$

and the change in misfit is:

$$\delta\chi = \int_0^T \dot{S}(t - t_s)I(\boldsymbol{\varepsilon}^\dagger)(\mathbf{x}_s, T - t) : \delta\mathbf{M}dt \quad (6.20)$$

$$+ \int_0^T \dot{S}(t - t_s)\delta\mathbf{x}_s \cdot \nabla_s I(\boldsymbol{\varepsilon}^\dagger)(\mathbf{x}_s, T - t) : \mathbf{M}dt \quad (6.21)$$

$$- \int_0^T \ddot{S}(t - t_s)\delta t_s I(\boldsymbol{\varepsilon}^\dagger)(\mathbf{x}_s, T - t) : \mathbf{M}dt. \quad (6.22)$$

A similar result for waves on a membrane was obtained by *Tape et al.* (2007). As the slip-rate is often described by a gaussian, or a box-car, the first term shows that the change in the point-source moment-tensor elements is given by an integral of a windowed version of the integral of the adjoint strain. The second term again shows how an update of the location of the source can be obtained by monitoring the gradient of the adjoint strain, at the location of the source. The third term describes how to update the source-time history.

In finite fault modeling, one often chooses a fault plane discretization in space and time, such that:

$$\dot{\mathbf{m}}(\mathbf{x}, t) = \sum_p \sum_q \dot{\mathbf{m}}_{pq}\delta(\mathbf{x} - \mathbf{x}_p)\delta(t - t_q). \quad (6.23)$$

Substituting for $\delta\dot{\mathbf{m}}$ in Eq. 6.15 we have:

$$\delta\chi = \sum_p \sum_q \delta\dot{\mathbf{m}}_{pq} : I(\boldsymbol{\varepsilon}^\dagger)(\mathbf{x}_p, T - t_q) \quad (6.24)$$

The quantity $I(\boldsymbol{\varepsilon}^\dagger)(\mathbf{x}_p, T - t_q)$ therefore corresponds to the moment-rate function of the updated source.

Finally it is of interest to write the change in moment tensor elements in terms of the standard fault parameters, strike ζ , dip i and rake γ . Writing (*Aki and Richards, 1980*)

$$\begin{aligned}
\mathbf{m} = & \mu\Delta s[\sin 2i \sin \gamma \hat{\mathbf{r}}\hat{\mathbf{r}} - (\sin i \cos \gamma \sin 2\zeta + \sin 2i \sin \gamma \sin^2 \zeta)\hat{\boldsymbol{\theta}}\hat{\boldsymbol{\theta}} \\
& + (\sin i \cos \gamma \sin 2\zeta - \sin 2i \sin \gamma \cos^2 \zeta)\hat{\boldsymbol{\phi}}\hat{\boldsymbol{\phi}} \\
& - (\cos i \cos \gamma \cos \zeta + \cos 2i \sin \gamma \sin \zeta)(\hat{\mathbf{r}}\hat{\boldsymbol{\theta}} + \hat{\boldsymbol{\theta}}\hat{\mathbf{r}}) + (\cos i \cos \gamma \sin \zeta - \cos 2i \sin \gamma \cos \zeta)(\hat{\mathbf{r}}\hat{\boldsymbol{\phi}} + \hat{\boldsymbol{\phi}}\hat{\mathbf{r}}) \\
& - (\sin i \cos \gamma \cos 2\zeta + \frac{1}{2} \sin 2i \sin \gamma \sin 2\zeta)(\hat{\boldsymbol{\theta}}\hat{\boldsymbol{\phi}} + \hat{\boldsymbol{\phi}}\hat{\boldsymbol{\theta}})]. \tag{6.25}
\end{aligned}$$

We can now write the perturbation in \mathbf{m} in terms of the fault parameters $(\mu\Delta s, \zeta, i, \gamma)$. Substituting into Eq. 6.4 then Eq. 6.14 we can write the change in misfit as

$$\begin{aligned}
\delta\chi = & \int_0^T \int_{\Sigma} K_{\Delta s}(\mathbf{r}, T-t) \delta(\mu\Delta s)(\mathbf{r}, t) d\Sigma dt + \int_{\Sigma} K_{\gamma}(\mathbf{r}) \delta\gamma(\mathbf{r}) d\Sigma + \int_{\Sigma} K_i(\mathbf{r}) \delta i(\mathbf{r}) d\Sigma \\
& + \int_{\Sigma} K_{\zeta}(\mathbf{r}) \delta\zeta(\mathbf{r}) d\Sigma + \int_{\Sigma} K_h(\mathbf{r}) \delta h(\mathbf{r}) d\Sigma. \tag{6.26}
\end{aligned}$$

Explicit expressions for the kernels $K_{\Delta s}$, K_{γ} , K_i , K_{ζ} , and K_h are given in appendix B.

Here we have obtained expressions for the gradient of a waveform misfit function. *Tromp et al. (2005)* show how choosing a different misfit function, such as a travel-time or amplitude misfit, can be used in a similar manner as the waveform misfit, and the difference appears in the form of the adjoint source $\mathbf{f}^\dagger(\mathbf{x}, t)$.

We have shown several ways to estimate the gradient of the misfit function, $\delta\chi$, depending on the parametrization of the earthquake source. In order to update the model parameters, \mathbf{m} , we need to decide how to use the gradient to get a new estimate. There are several known methods, such as *steepest decent* methods and *conjugate gradient* methods. The inversion for the amplitude of a point force source (*Tromp et al., 2005*) in 3D and the location and timing of a point source in 2D (*Tape et al., 2007*) were performed using a conjugate gradient method.

6.3 The connection between adjoint methods, time-reversal imaging and stacking

As we saw in the previous section, the first step of an adjoint method is the back-propagation of the time-reversed data traces. This is the core of time-reversal methods (*McMechan,*

1982). Lately, several studies have applied stacking methods, in order to track the origin of high frequency radiation of large earthquakes (*Krüger and Ohrnberger, 2005a; Ishii et al., 2005*) and to locate earthquakes that do not have a clear beginning (*Kao and Shan, 2004; Ekström, 2006*). Here we wish to show the similarity between time-reversal imaging and stacking methods, by relating the adjoint field (Eq. 6.10) to the equation given for the stack by *Ishii et al. (2005)*:

$$s_j(t) = \sum_{k=1}^N (p_k/A_k) u_k(t - t_{jk}^P + \Delta t_k), \quad (6.27)$$

where $s_j(t)$ is the stack at test location j , u_k is the vertical component seismogram recorded at station k , p_k is a polarity correction, A_k is an amplitude correction, t_{jk} is the travel time between test source j and station k computed for a 1D reference model, and Δt_k is an empirical “station correction” for 3D effects. The amplitude, polarity and station correction factors are obtained by cross-correlating the very first few seconds of the recorded seismograms with a reference stack. To enhance the image, the authors square the stack and integrate over short time windows to obtain the “brightness”. They relate the brightness to the energy radiated from the test-source location during each successive time window.

For comparison, we start with the adjoint source (Eq. 6.9) for the “zero” model, i.e. with the synthetics set to zero. We also allow for a weighting factor w_r and a time shift Δt_r for each trace:

$$f_i^\dagger(\mathbf{x}, t) = \sum_{r=1}^N w_r u_i(\mathbf{x}_r, T - t + \Delta t_r) \delta(\mathbf{x} - \mathbf{x}_r). \quad (6.28)$$

We now convolve this source with the Green’s function to obtain the adjoint wave field

$$s_k^\dagger(\mathbf{x}, t) = \int_0^t \int_V G_{ki}(\mathbf{x}, \mathbf{x}'; t - t') f_i^\dagger(\mathbf{x}', t') d^3 \mathbf{x}' dt' = \quad (6.29)$$

$$\sum_{r=1}^N \int_0^t w_i G_{ki}(\mathbf{x}, \mathbf{x}_r; t - t') u_i(\mathbf{x}_r, T - t' + \Delta t_r) dt'. \quad (6.30)$$

In order to compare to Eq. 6.27 we focus on the vertical component of the wave field, and use only the vertical component of the adjoint field. We can then drop the indices denoting the component:

$$s^\dagger(\mathbf{x}, t) = \int_0^t \sum_{r=1}^N w_i G(\mathbf{x}, \mathbf{x}_r; t - t') u(\mathbf{x}_r, T - t' + \Delta t_r) dt' \quad (6.31)$$

We now decide to record the adjoint field only at selected test locations j (which could be located on a grid). We further refer to the locations of the receivers as k . Now we can drop the \mathbf{x} -dependence and the Green's function G_{jk} then corresponds to the zz element of the Green's tensor, from source location j to receiver location k :

$$s_j^\dagger(t) = \sum_{k=1}^N \int_0^t w_i G_{jk}(t-t') u_k(T-t' + \Delta t_k) dt'. \quad (6.32)$$

At this point we have to assume the shape of the Green's function. Comparing to the direct P-wave, we can assume that the Green's function is a delta function at time t_{jk} , which is the travel time between test source j and receiver k , multiplied by an amplitude factor, a_{jk} , that contains information on excitation and path effects, or $G_{jk}(t-t') = a_{jk} \delta(t-t'-t_{jk})$ (*Aki and Richards*, 1980). Now the adjoint field can be written as:

$$s_j^\dagger(t) = \sum_{k=1}^N \int_0^t w_i a_{jk} \delta(t-t'-t_{jk}) u_k(T-t' + \Delta t_k) dt' \quad (6.33)$$

If we want to look at the adjoint field at and just after the start time of the source T we get:

$$s_j^\dagger(T-t) = \sum_{k=1}^N w_k a_{jk} u_k(t-t_{jk} + \Delta t_k), \quad (6.34)$$

which can be compared to:

$$s_j(t) = \sum_{k=1}^N (p_k/A_k) u_k(t-t_{jk}^P + \Delta t_k). \quad (6.35)$$

Thus, in order to compare the results, we can multiply the adjoint sources f_k^\dagger by $w_k = p_k/(A_k a_{jk})$. If we are using the same Earth model for the back-propagation as is used to compute t_{jk}^P we can also apply the shifts Δt_k (obtained from cross-correlation), to the data before back-propagation in order to correct for 3D effects.

6.4 Back-propagation of high frequency radiation

In order to demonstrate the similarity between the time-reversal method and stacking methods in practice, we apply the theory to the Hinet data set for the Sumatra earthquake. Hinet (<http://www.hinet.bosai.go.jp/>) is a dense array of high-frequency bore-hole instruments in

Japan. The sensors have a corner frequency of 1 second and are all buried by at least 100 meters, reducing noise from the surface. There are around 700 Hinet stations distributed over the Japanese Islands, continuously recording, providing us with an unequaled high-frequency data set for a giant earthquake. The data set has been shown to give an estimate of the extent and duration of the 2004 Sumatra earthquake using stacking methods (*Ishii et al.*, 2005; *Krüger and Ohrnberger*, 2005b). The location of the array relative to the earthquake source area is shown in Fig. 6.2.



Figure 6.2: Geometry of the simulations used for stacking and back-propagation of high-frequency data. The Hinet stations used in the study are shown with red triangles and the source area is shown with the small rectangle. The region of simulations for the back-propagation is shown with a large rectangle (65° across in each direction).

6.4.1 Stacking

Here we repeat the experiment of *Ishii et al.* (2005) for comparison with the back-propagation method. We compute the stacks for a grid of test locations in the region around the source, according to Eq. 6.27. We start with a total of 552 vertical component records. We estimate the time-shifts and polarity corrections, Δt_k and p_k , based on cross-correlation of the first four seconds of the records with a reference stack, as described by *Ishii et al.* (2005). Only records with cross-correlation factors higher than 0.7 are retained, leaving 384 records. The

amplitude normalizing factor A_k is given by the ratio of the maximum amplitude within the four second window of the trace versus the stack. Once the stack is obtained for all the test locations, we compute the square of each stack, and integrate over 30 second time windows. The integral over the time window at each location is referred to as the brightness and can be related to the energy radiated from the test location within the time window (*Ishii et al., 2005*). By tracking the location of high brightness through successive time windows one can monitor the spatio-temporal origin of the high-frequency energy. The results of the stacking the unfiltered Hinet data is shown in Fig. 6.3. The high-frequency stacks show remarkable focusing on a small region on the fault plane. Some smearing (southwest to northeast) is visible, in the direction of the array. The highest brightness is seen at times between 60-90 seconds and 300-330 seconds. The integral of the brightness over times from 0-600 seconds is also shown in Fig. 6.3. As is evident from Eq. 6.27 the stack is only based on the direct P-wave. The other arrivals within the seismograms stack incoherently and therefore do not contribute as much to the stack as the direct P-wave. Furthermore, at these very high frequencies (the dominant frequencies in the Hinet records are 1-2 seconds), phases that travel substantial distances near the surface (such as PP) are highly attenuated. The favorable stacking properties of high-frequency P-waves together with the spatially dense high-quality data lead to the stunning results shown in Fig. 6.3. Despite recent development in high-performance computing, simulating waves at 1 seconds over regional distances is still a challenge. In order to compare to the stacking method to back-propagation methods we therefore need to low-pass filter the Hinet data before stacking. We remove the instrument response from the data by deconvolution and band-pass between 3 and 10 seconds. The results of stacking the filtered data is shown in Fig. 6.4. As to be expected for longer period data the focusing is not as point like. Furthermore, the relative amplitude between successive time-windows changes more than for the shorter period data. At times between 300-330 seconds the highest brightness is off the fault plane. We interpret this as an effect of constructive stacking of other phases than P within the time-window. Also notice that the highest value of integrated brightness over the whole time window is further north than for the unfiltered stacks.

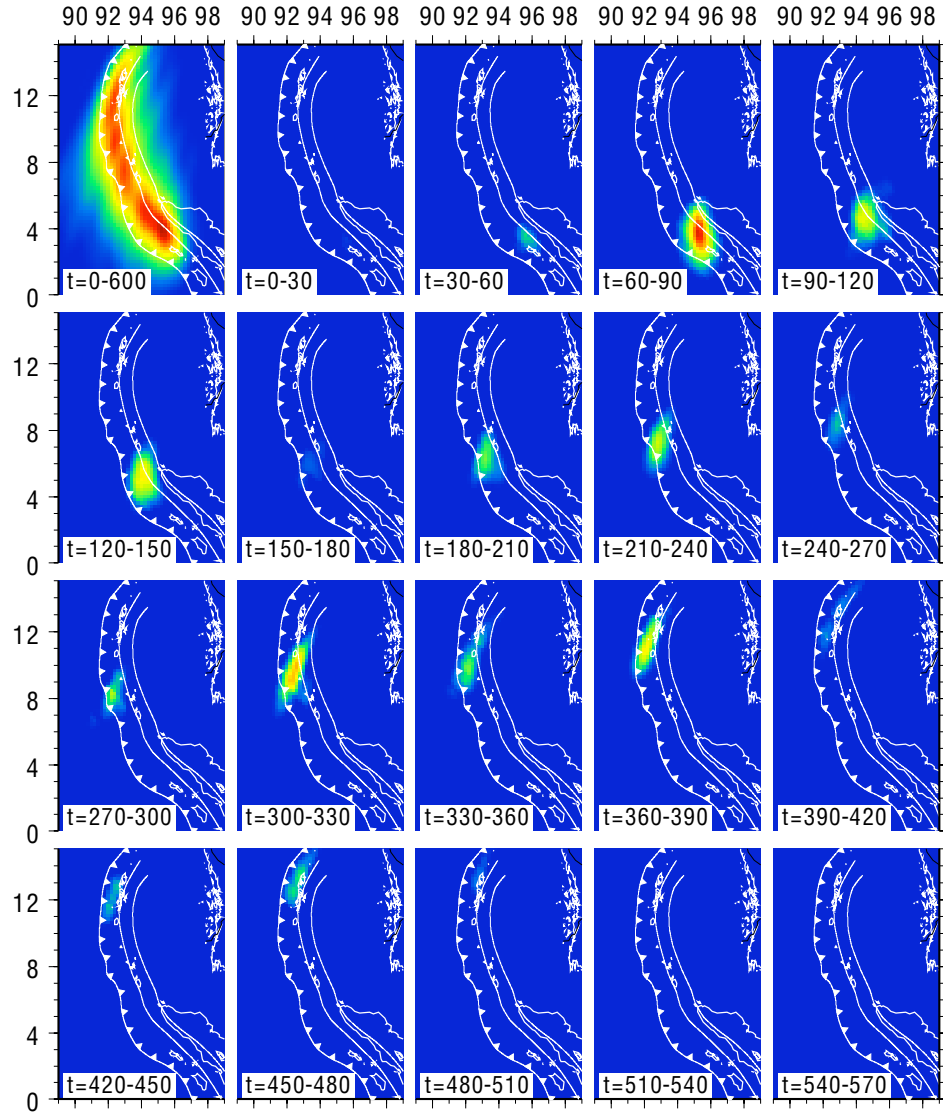


Figure 6.3: The results of stacking unfiltered Hinet data. The color of each pixel indicates the brightness (the relative value of the integral of the squared stack) over the time-window specified. Note the high localization of the source in each window. This is a repeat of the experiment by (*Ishii et al.*, 2005).

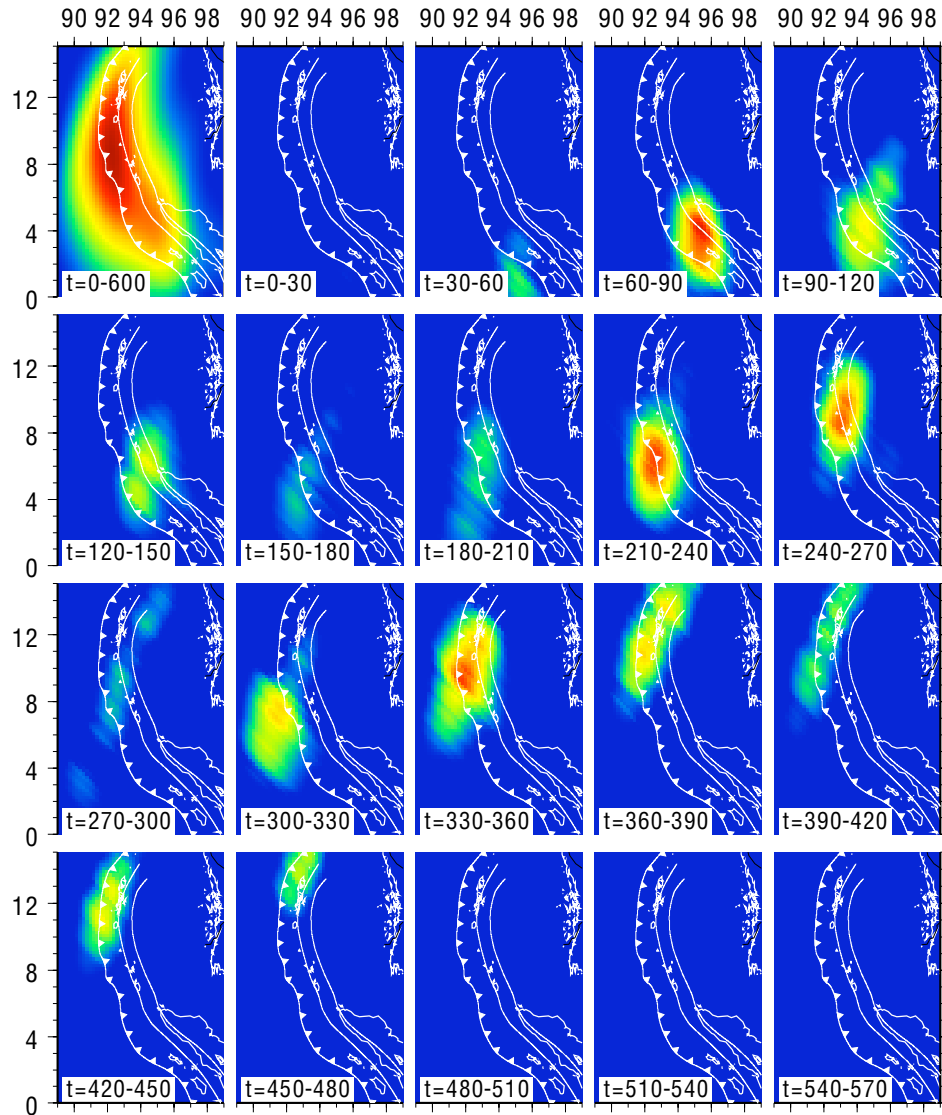


Figure 6.4: Same as Fig. 6.3 except the data has been low-pass filtered at 3 seconds before stacking. Notice the larger area of high brightness, as to be expected due to the longer periods involved. Also note the increase of artifacts, in particular the area of high brightness far west of the subduction zone in the time window between 300 and 330 seconds.

6.4.2 Time-reversal imaging of high-frequency data

Now we wish to repeat the experiment from the last section, where we stacked Hinet data to determine the spatio-temporal location of the source of high-frequency energy, using the time-reversal methodology. We therefore prepare the data in the same way as before, by shifting the traces by Δt_k and multiplying them by p_k/A_k . To be more accurate we should also multiply the traces by the term $1/a_k$, that accounts for the excitation and propagation effect from station to test source. However, since we are using a 1D model, and the paths between all the sources and receivers are similar, that factor is not included. We then reverse the traces in time, and insert them as simultaneous sources into a wave-propagation solver. We use the same spectral-element code as described in previous chapters, with modifications for adjoint simulations (*Liu, 2006*). However, in order to compare to the stacking methods, we use the 1D Earth model PREM *Dziewonski and Anderson (1981)*. The region of the simulation is shown in Fig. 6.2. The simulation takes around 27 hours on 1225 3.2MHz processors, and is accurate to 2.8 seconds. We record the displacement on a grid of test-sources for comparison to the stacks. We now time-reverse the records, and process the traces in the same way as the stacks, i.e. square them and integrate over 30 second time windows. The results are shown in Fig. 6.5.

The location of high brightness shows a propagating rupture starting in the south and moving north, with similar sized area of high brightness as the filtered stack (Fig. 6.4). We do not expect the results to be identical between the two methods, as the back-propagation procedure includes constructive interference of all the phases present within the data traces (one can view this as stacking on all the phases within the seismogram simultaneously), whereas the stacks only include the direct P-wave. However, the figures are remarkably similar, with the exception of the absence of constructive interference in the window between 60–90 seconds and the location of high brightness in time-window 300-330 seconds, which is closer to the fault as seen by the time-reversal experiment.

6.5 Time-reversal imaging of long-period data

We have shown that we can track the propagation of rupture for the Sumatra earthquake, by back-propagation of high-frequency data. At this stage we know just the location of the source of high-frequency energy, and the relative magnitude thereof. However, we are also

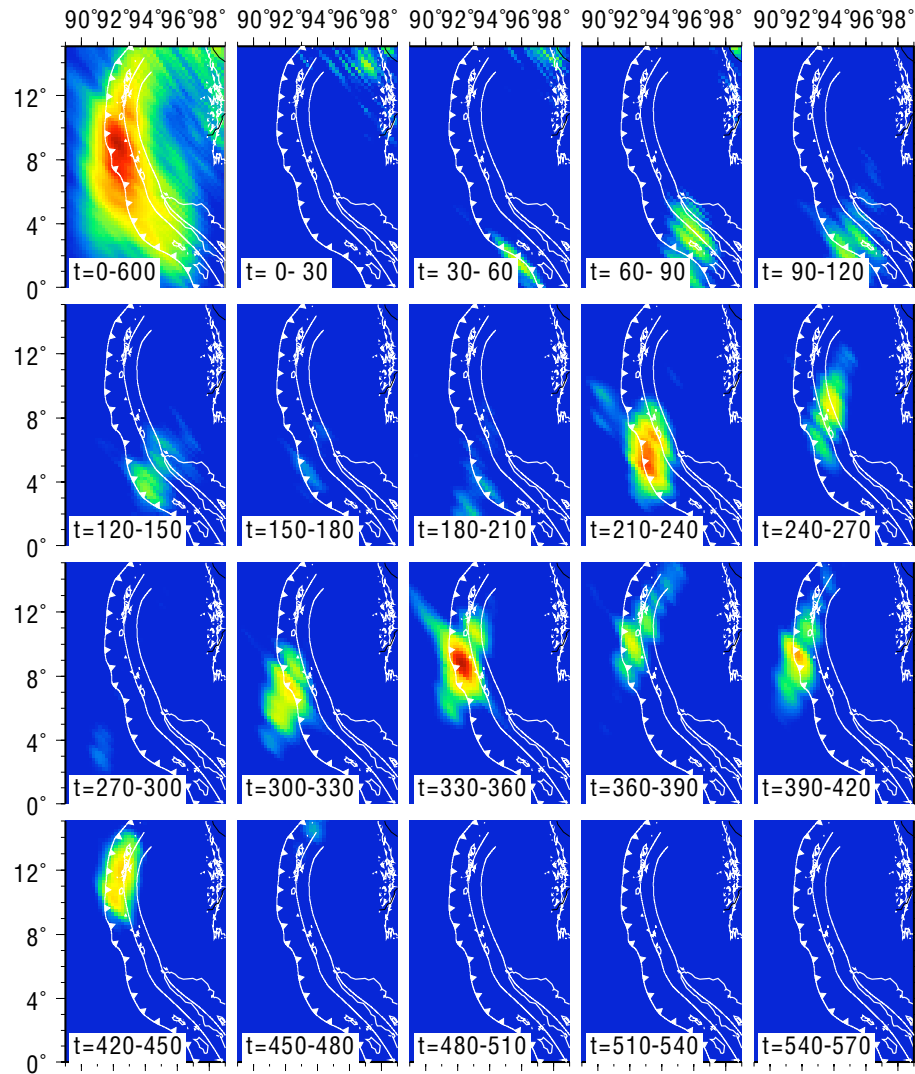


Figure 6.5: Time-reversed high-frequency data from the Hinet array. The time-reversed velocities have been processed in the same way as the stacks in section 6.4.1. Notice how the bright patch in window 300-330 seconds is now concentrated closer to the fault plane.

interested in the magnitude of the slip and the mechanism. We have shown in the previous section how to relate these quantities to the adjoint wave field. We do not expect the high-frequency data to contain much information on these quantities, so we turn to long-period data. *Larmat et al.* (2006) have shown that long-period data (of 200 seconds and longer) from the Sumatra earthquake can be successfully time-reversed with convergence on the source. They deconvolve the time-reversed field for a smaller event from the time-reversed field for the main event to infer the slip history of the source. Here we wish to use the formalism presented in section 6.2 to directly infer the slip history of the source from the time-reversed field. We apply the method to three of the large earthquakes studied in previous chapters, the 2004 Sumatra earthquake, the 2001 Kunlun, China earthquake and the 1998 Balleny Islands earthquake.

6.5.1 Data and processing

We use three component, broad-band data from the global network, obtained from the IRIS data center (<http://www.iris.edu>), deconvolved to displacement and band-pass filtered from 60 to 500 seconds. The duration of the records is 100 minutes starting from the hypocentral time. We then apply weights to the data that are inversely proportional to the number of records in each azimuth range (as seen from the source), so that azimuths with a lot of stations do not dominate the reversed field. We now use the time-reversed records as simultaneous sources and solve for the adjoint wave field, using a spectral-element method, as before. We store the resulting wave field (displacements and strains) on a grid surrounding the epicentral area. We visualize the field in two ways. The first is as snapshots of the integral of the adjoint strain at successive times. We look at each of the six independent components separately. According to Eq. 6.24 the integrated strain at each point is related to the moment-rate function function of the first-guess source model. Together with the snapshots we plot the square of the integral of the adjoint strain integrated over the entire time window to get an estimate of where the largest amplitudes are. In order to graphically enhance the image we also plot the envelope of the strains, squared and subsequently integrated over short time windows. Together with these maps we plot the same quantity integrated over the whole time window.

6.5.2 Interpretation of adjoint strain maps

We wish to interpret the integrated adjoint strain, in terms of the moment-rate function, according to Eq. 6.24. We recall that the moment surface density \mathbf{m} can be written as $\mathbf{m} = \mu\Delta s(\hat{\nu}\hat{\sigma} + \hat{\sigma}\hat{\nu})$ (Eq. 6.3) where μ is the shear modulus, Δs is the magnitude of slip, $\hat{\nu}$ is the fault normal and $\hat{\sigma}$ is the direction of slip. We define $\hat{\mathbf{m}} = \hat{\nu}\hat{\sigma} + \hat{\sigma}\hat{\nu}$, for convenience. Note that in this definition $\hat{\mathbf{m}}$ is not a unit tensor, but has length $\sqrt{2}$. For a vertical, east-west oriented, strike-slip fault $\hat{\nu} = \hat{\mathbf{N}}$ and $\hat{\sigma} = \hat{\mathbf{E}}$, and therefore $\hat{\mathbf{m}} = \hat{\mathbf{E}}\hat{\mathbf{N}} + \hat{\mathbf{N}}\hat{\mathbf{E}}$. Here we have defined $\hat{\mathbf{E}}, \hat{\mathbf{N}}$ and $\hat{\mathbf{Z}}$ to be the unit vectors pointing east, north and up respectively. Comparing this to equation 6.24 we see that for an east-west oriented, vertical, strike-slip earthquake, we expect only the NE component of strain to be large on the fault plane. However, if the fault plane has a non-vertical dip, and $\hat{\nu} = a\hat{\mathbf{N}} + b\hat{\mathbf{Z}}$, then $\hat{\mathbf{m}} = a(\hat{\mathbf{E}}\hat{\mathbf{N}} + \hat{\mathbf{N}}\hat{\mathbf{E}}) + b(\hat{\mathbf{E}}\hat{\mathbf{Z}} + \hat{\mathbf{Z}}\hat{\mathbf{E}})$, and therefore we expect both the NE and EZ components of the adjoint strain to be large on the fault plane. In a general case the relative sizes of the moment-tensor elements *on the fault plane* are thus indicative of the relative size of the moment-tensor elements of the original source.

It is also illuminating to examine the form of the equation describing the gradient of the misfit function, $\delta\chi$, for a point source (Eq. 6.22). The first term shows how the change in moment-tensor elements is governed by the integral of the adjoint strain with the source-time history. The second term, which prescribes how to update the source location, involves the gradient of the adjoint strain with respect to the source coordinates, double dotted with the moment-tensor. Thus, only the gradient of the elements of the strain tensor that are large contribute. In the example of the east-west oriented, vertical strike-slip fault, we would expect the NE component of the adjoint strain field to collapse to a peaked function in space. The second term of Eq. 6.22 describes how to move the source location to the top of the peak. The third terms prescribes how to update the source-time history.

One way of viewing the time-reversed wave field is as the restored original wave field. The slip on the fault plane produces a strain with an orientation governed by $\hat{\nu}\hat{\sigma} + \hat{\sigma}\hat{\nu}$ on the fault. However, the slip on the fault also induces other strains off the fault. As discussed above, an east-west oriented, vertical, purely strike-slip fault results in a large NE component of strain on the fault plane. However, for example, in the extensional and compressional quadrants around the fault plane, we expect to see large EE and NN

components of strain, with opposite sign in the respective quadrants. We expect these secondary strains to appear in the maps of the adjoint strain, *off the fault plane*. In the second iteration of the adjoint method, where we back-propagate the difference between data and synthetics computed for the initial guess source model, these strains will vanish. The off-fault strains in the maps illustrate the trade-off between the source location and the mechanism, inherent in the inversions.

As the surface of the Earth can be assumed to be traction free, the strains involving Z should vanish at the surface. This is connected to the well known problem in seismology that for very shallow earthquakes, the EZ and NZ components of the moment tensor are ill constrained. The ZZ component is often constrained by forcing the moment tensor to have zero trace. As there is no information in the adjoint strain on how to update the EZ , NZ and ZZ elements of the moment tensor, at very shallow depths, the misfit does not depend on them, and they will not be changed from the initial value.

6.5.3 Application to the 2004 Sumatra earthquake

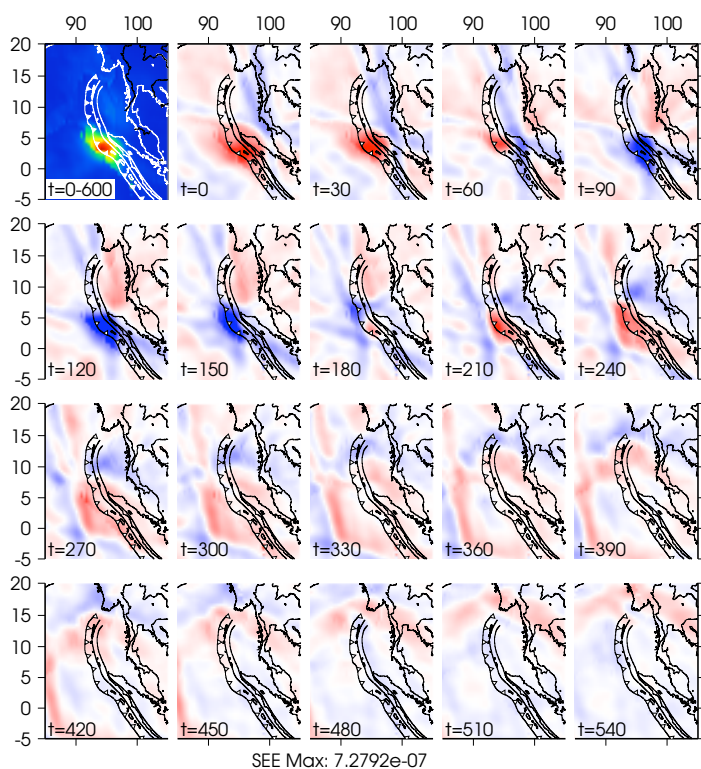
The 2004 Sumatra, Indonesia earthquake occurred on a curved fault plane, with NNW–SSE strike in the south, and N–S strike further north, as discussed in chapter 5. The slip was close to pure thrust in the south, with more oblique slip in the north. The dip of the fault plane is thought to have been close to 10° . We therefore expect $\hat{\nu} = (a\hat{\mathbf{E}} + b\hat{\mathbf{N}} + c\hat{\mathbf{Z}})$ with $c > a > b$, and $\hat{\sigma} = (d\hat{\mathbf{E}} + e\hat{\mathbf{N}} + f\hat{\mathbf{Z}})$ with $d > e > f$. The largest moment tensor elements would therefore be EZ component. However, we also expect large EE and ZZ components.

The time-reversed field for the Sumatra earthquake is shown in Figs. 6.6–6.11. The different components of strain show varying levels of localization on the fault plane. Components EE , NN and ZZ have large amplitudes on the fault plane, whereas others have the largest amplitudes off the fault plane. The northward rupture propagation is visible on several components, although the signature from the southern part of the fault plane is much more visible. Only the EZ component has larger amplitudes in the north than in the south.

6.5.4 Application to the 2001 Kunlun China earthquake

As discussed previously in this thesis the Kunlun earthquake ruptured unilaterally from the west to the east, over a duration of about 120 seconds. The mechanism was left-lateral

SEE Max: 8.435e-06



SEE Max: 7.2792e-07

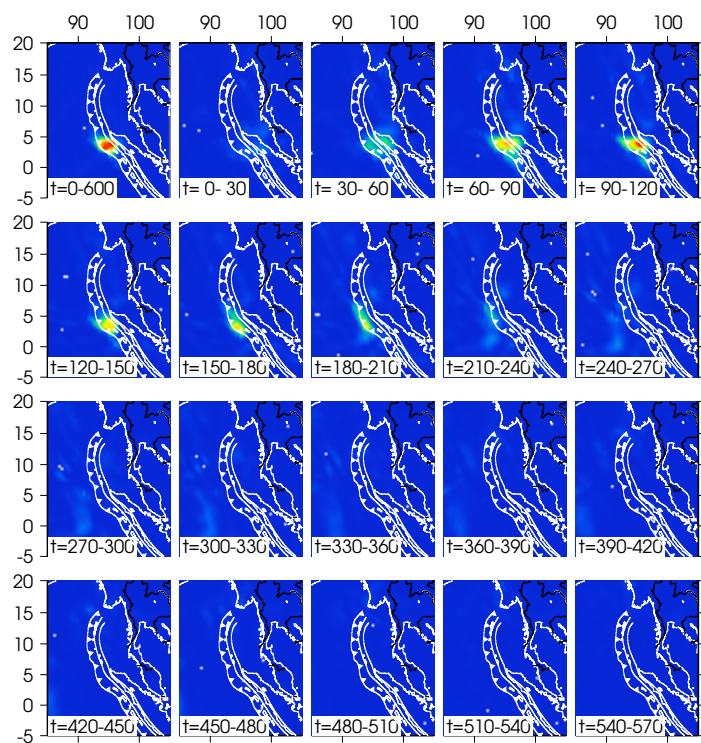


Figure 6.6: Top: Snapshots of the integral of the adjoint strain (component SEE) for the Sumatra earthquake. Bottom: Envelope of adjoint strain (component EE), squared and integrated over the given time windows. The slices are all plotted on the same scale (except the top left one), and the maximum value is given in the title. For more detail see section 6.5.1.

SEZ Max: 2.63515e-06

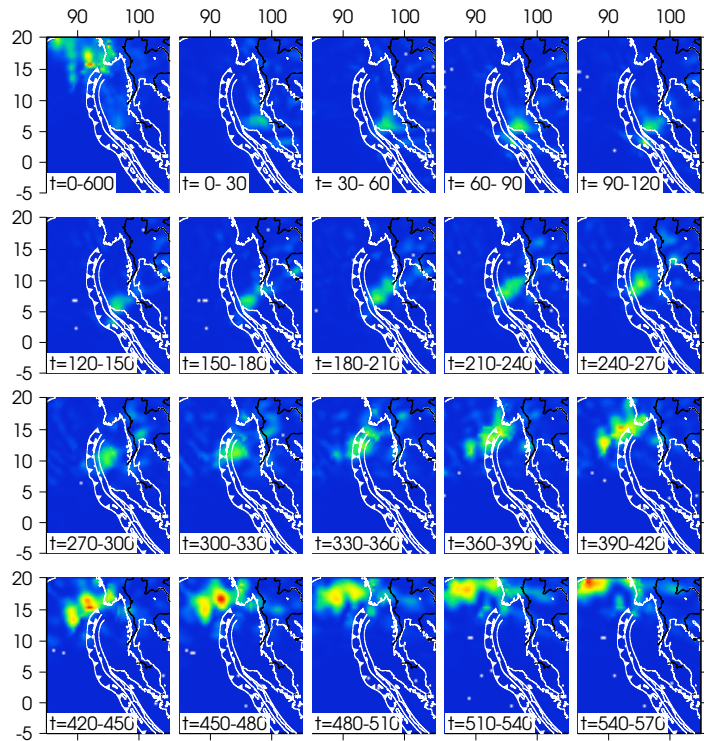
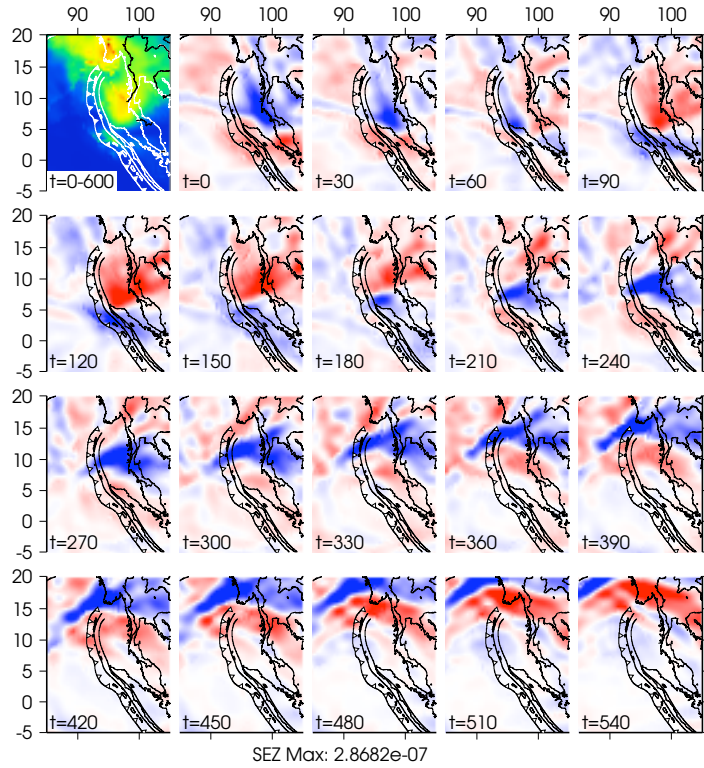
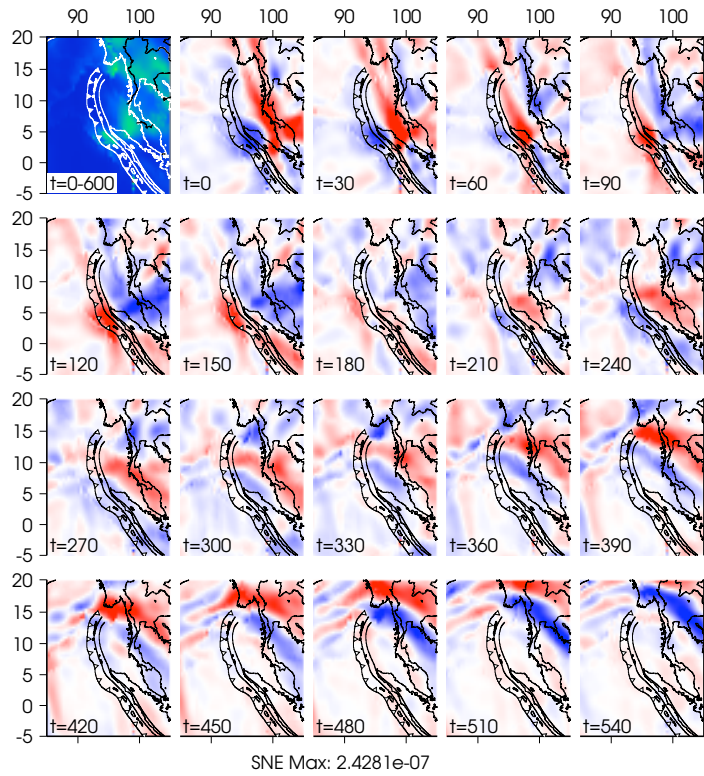


Figure 6.7: Top: Snapshots of the integral of the adjoint strain (component SEZ) for the Sumatra earthquake. Bottom: Envelope of adjoint strain (component EZ), squared and integrated over the given time windows. For more detail see section 6.5.1.

SNE Max: 2.389e-06



SNE Max: 2.4281e-07

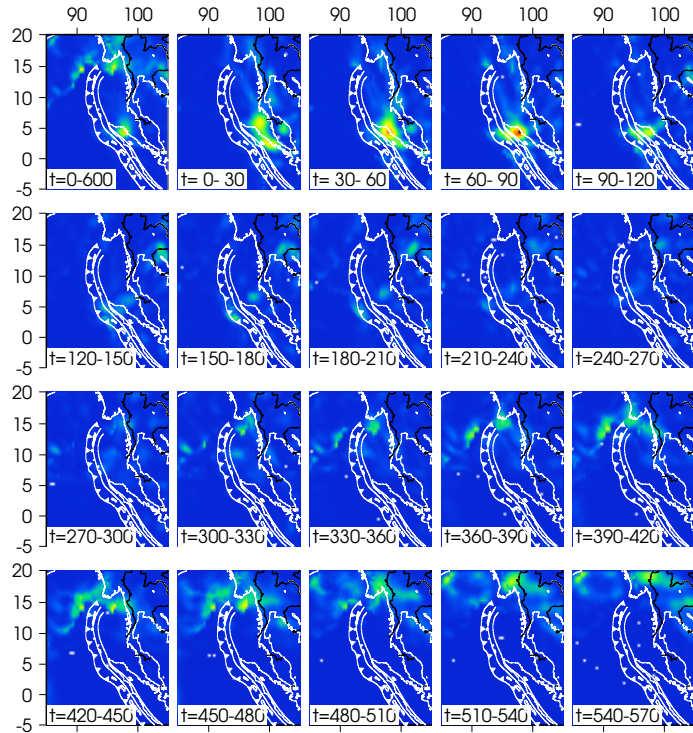


Figure 6.8: Top: Snapshots of the integral of the adjoint strain (component SNE) for the Sumatra earthquake. Bottom: Envelope of adjoint strain (component NE), squared and integrated over the given time windows. The slices are all plotted on the same scale (except the top left one), and the maximum value is given in the title. For more detail see section 6.5.1.

SNN Max: 1.1574e-05

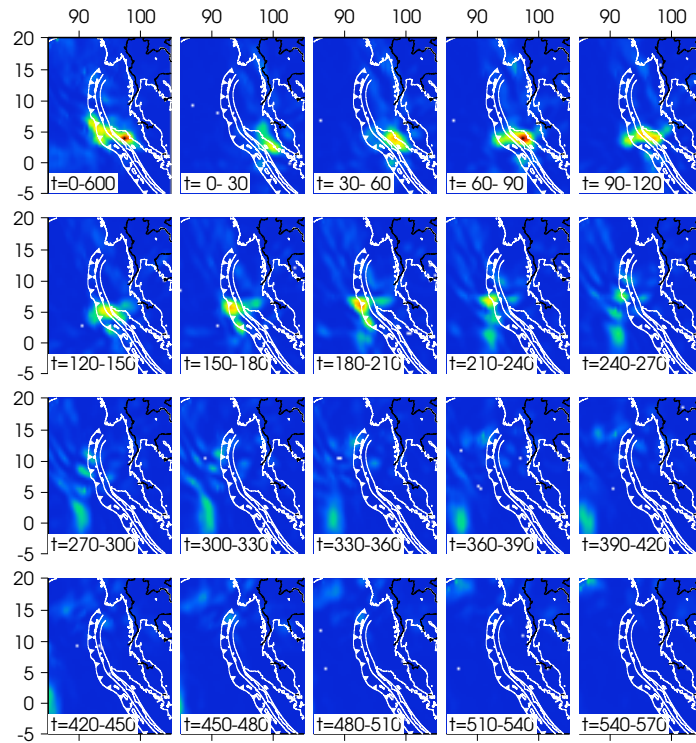
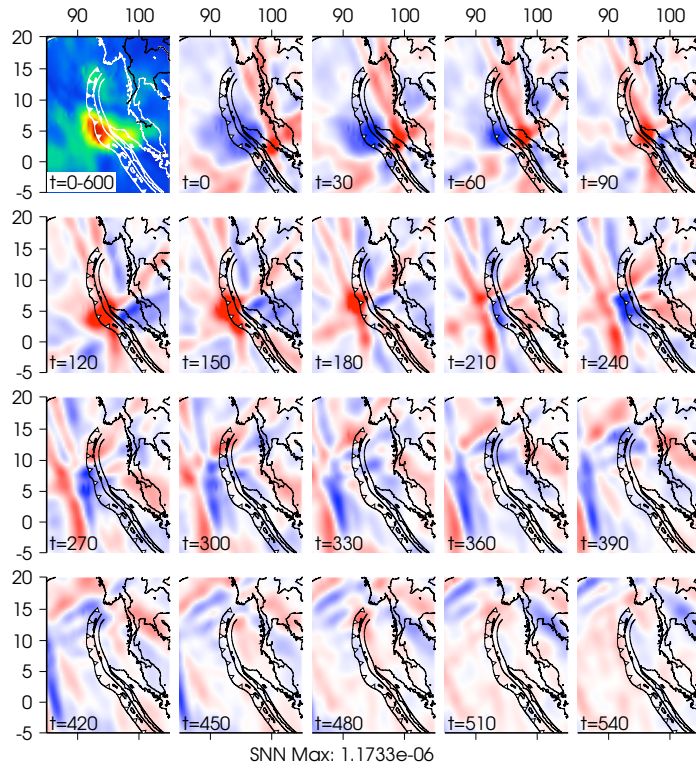


Figure 6.9: Top: Snapshots of the integral of the adjoint strain (component SNN) for the Sumatra earthquake. Bottom: Envelope of adjoint strain (component NN), squared and integrated over the given time windows. The slices are all plotted on the same scale (except the top left one), and the maximum value is given in the title. For more detail see section 6.5.1.

SNZ Max: 9.3105e-06

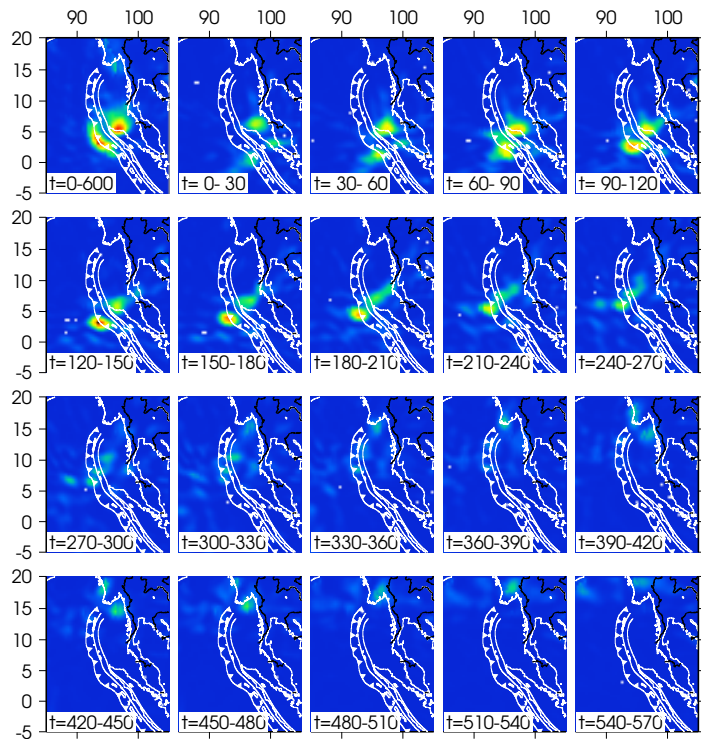
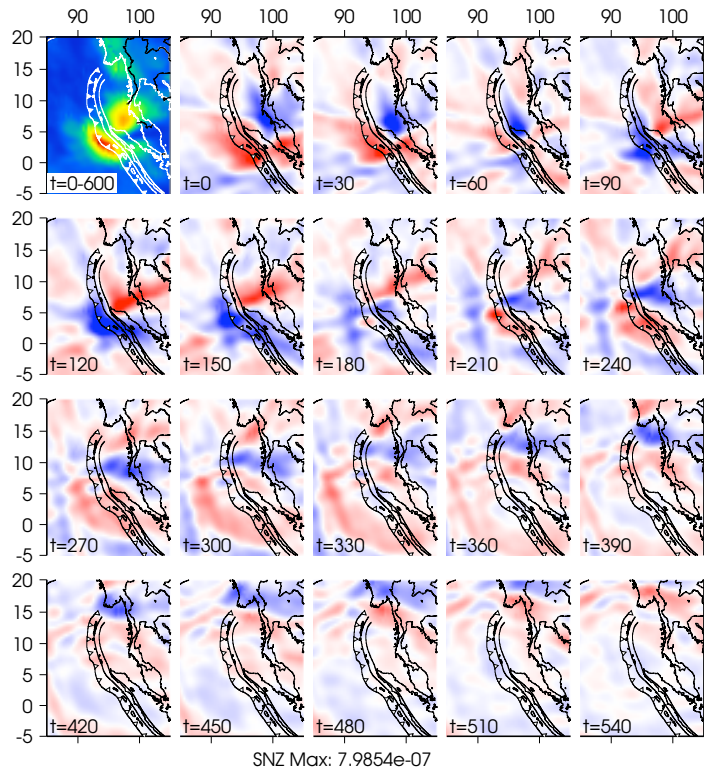


Figure 6.10: Top: Snapshots of the integral of the adjoint strain (component NZ) for the Sumatra earthquake. Bottom: Envelope of adjoint strain (component NZ), squared and integrated over the given time windows. The slices are all plotted on the same scale (except the top left one), and the maximum value is given in the title. For more detail see section 6.5.1.

SZZ Max: 1.20935e-05

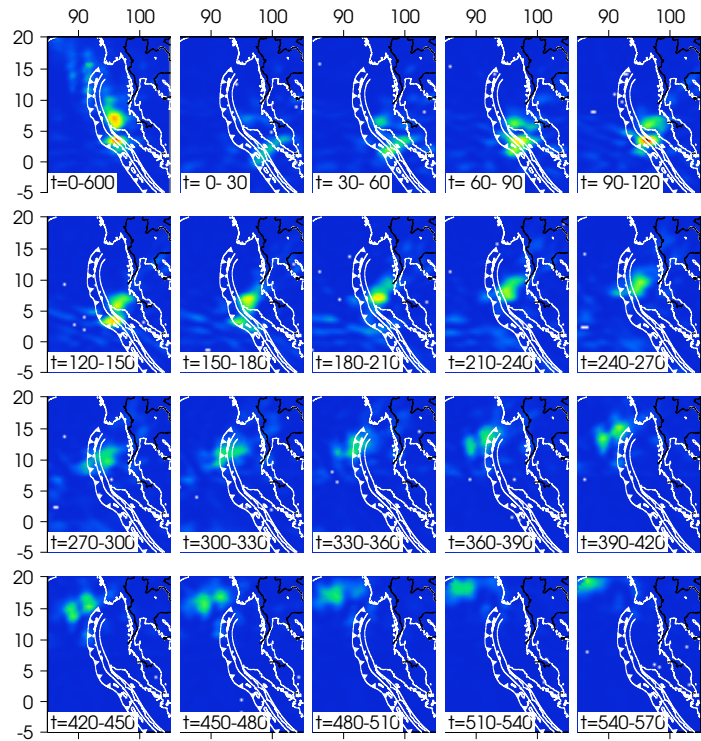
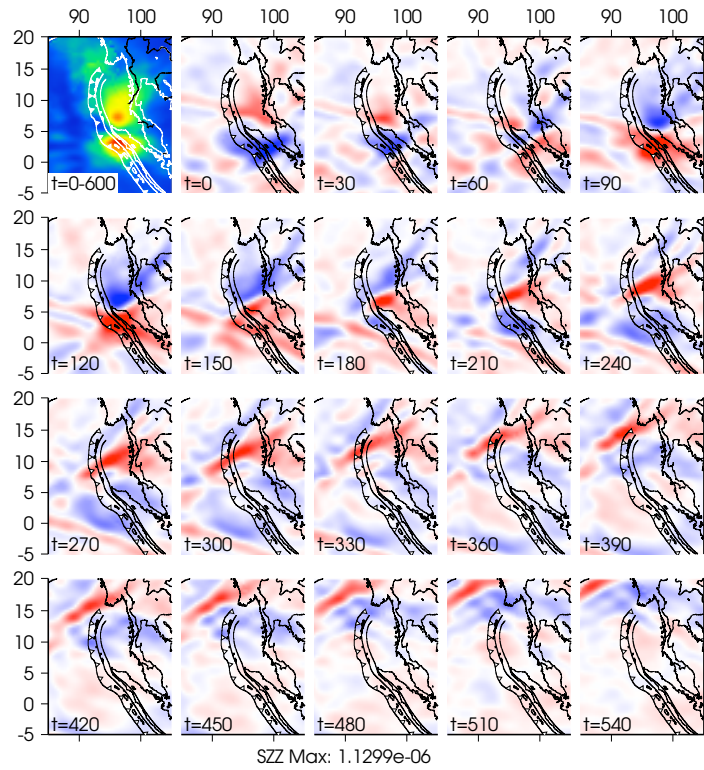


Figure 6.11: Top: Snapshots of the integral of the adjoint strain (component ZZ) for the Sumatra earthquake. Bottom: Envelope of adjoint strain (component ZZ), squared and integrated over the given time windows. The slices are all plotted on the same scale (except the top left one), and the maximum value is given in the title. For more detail see section 6.5.1.

strike slip on a fault-plane dipping 74° to the north, with components of thrust and normal faulting at different locations along strike. The largest moment-rate was observed at around 60 seconds after the initiation of rupture. The fault normal is $\hat{\nu} = (a\hat{\mathbf{N}} + b\hat{\mathbf{Z}})$ with $a > b$ and the slip vector is $\hat{\sigma} = (c\hat{\mathbf{E}} + d\hat{\mathbf{Z}})$ with $c > d$. We therefore expect the large on-fault strains to be the NE , the EZ , NZ and the ZZ components.

The time reversed field for the Kunlun earthquake is shown in Figs. 6.12-6.17. Indeed the adjoint strain shows a clear westward propagation, with large on fault strains for the NE and NZ components. The ZZ component is also non-zero on the fault, but not as localized as the NE and NZ components. The other components have larger off-fault strains. The largest strains are observed at times between 30-120 seconds. Thus both the location timing, and relative magnitude of the strains are consistent with what we expect from the discussion above (section 6.2).

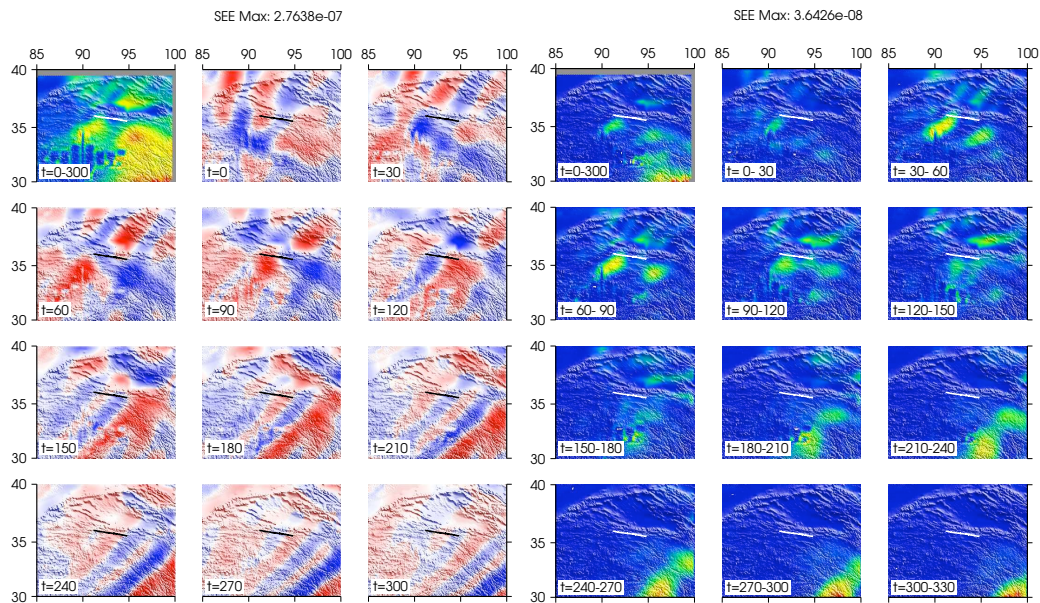


Figure 6.12: Left: Snapshots of the integral of the adjoint strain (component EE) for the Kunlun earthquake. Right: Envelope of adjoint strain (component EE), squared and integrated over the given time windows. The slices are all plotted on the same scale (except the top left one), and the maximum value is given in the title. The bold line indicates the fault trace (*Xu et al.*, 2006). For more detail see section 6.5.1.

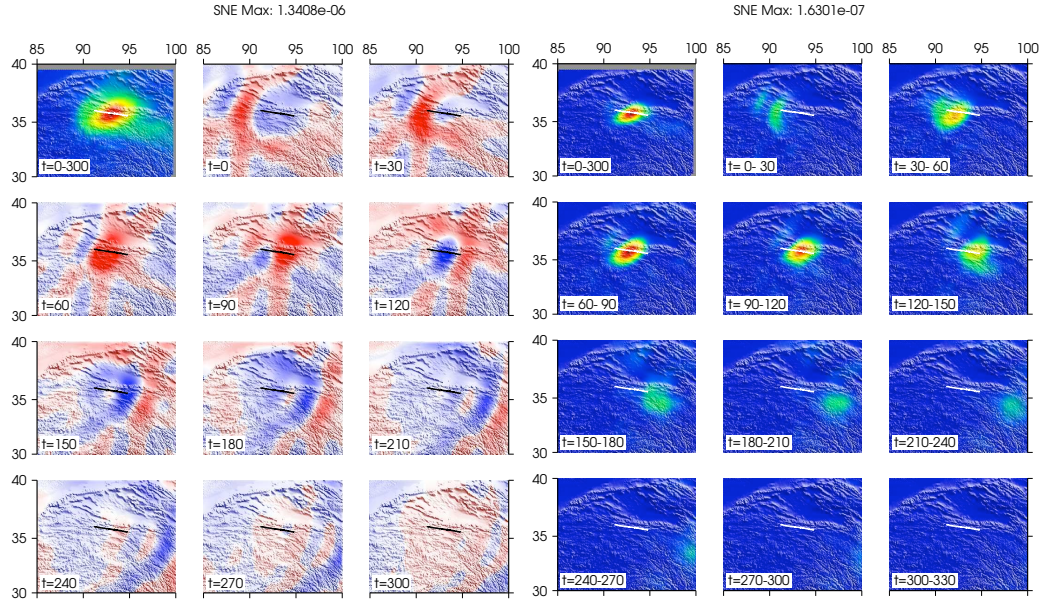


Figure 6.13: Left: Snapshots of the integral of the adjoint strain (component NE) for the Kunlun earthquake. Right: Envelope of adjoint strain (component NE), squared and integrated over the given time windows. The slices are all plotted on the same scale (except the top left one), and the maximum value is given in the title. The bold line indicates the fault trace (*Xu et al.*, 2006). For more detail see section 6.5.1.

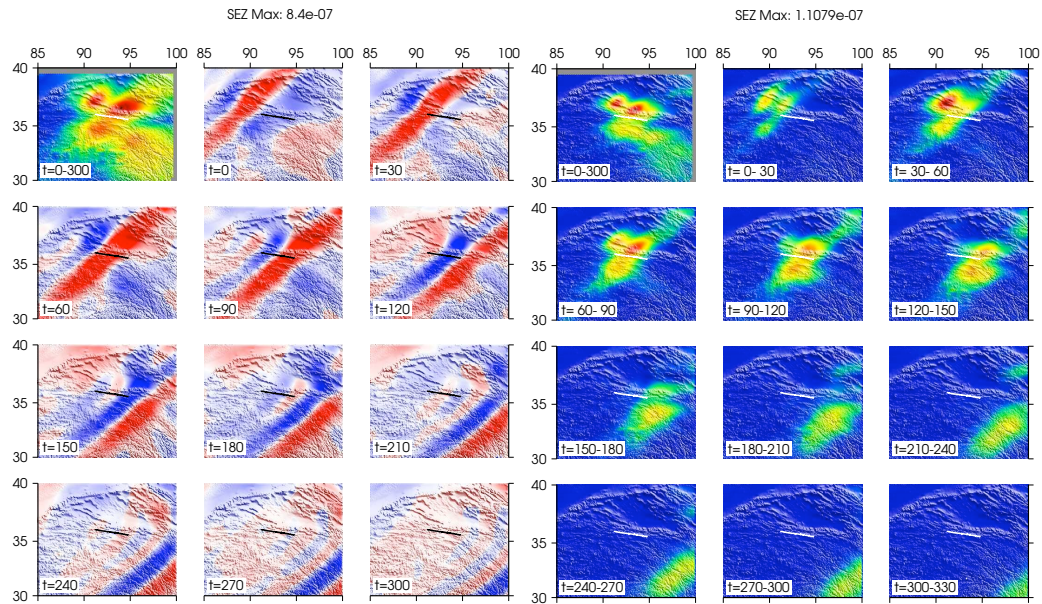


Figure 6.14: Left: Snapshots of the integral of the adjoint strain (component EZ) for the Kunlun earthquake. Right: Envelope of adjoint strain (component EZ), squared and integrated over the given time windows. The slices are all plotted on the same scale (except the top left one), and the maximum value is given in the title. The bold line indicates the fault trace (*Xu et al.*, 2006). For more detail see section 6.5.1.

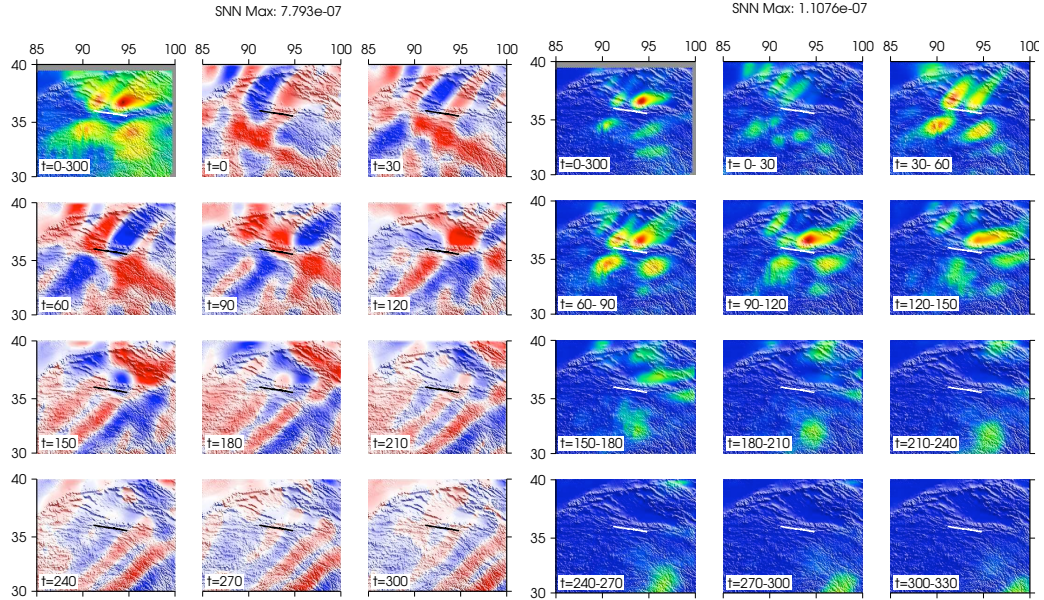


Figure 6.15: Left: Snapshots of the integral of the adjoint strain (component NN) for the Kunlun earthquake. Right: Envelope of adjoint strain (component NN), squared and integrated over the given time windows. The slices are all plotted on the same scale (except the top left one), and the maximum value is given in the title. The bold line indicates the fault trace (*Xu et al.*, 2006). For more detail see section 6.5.1.

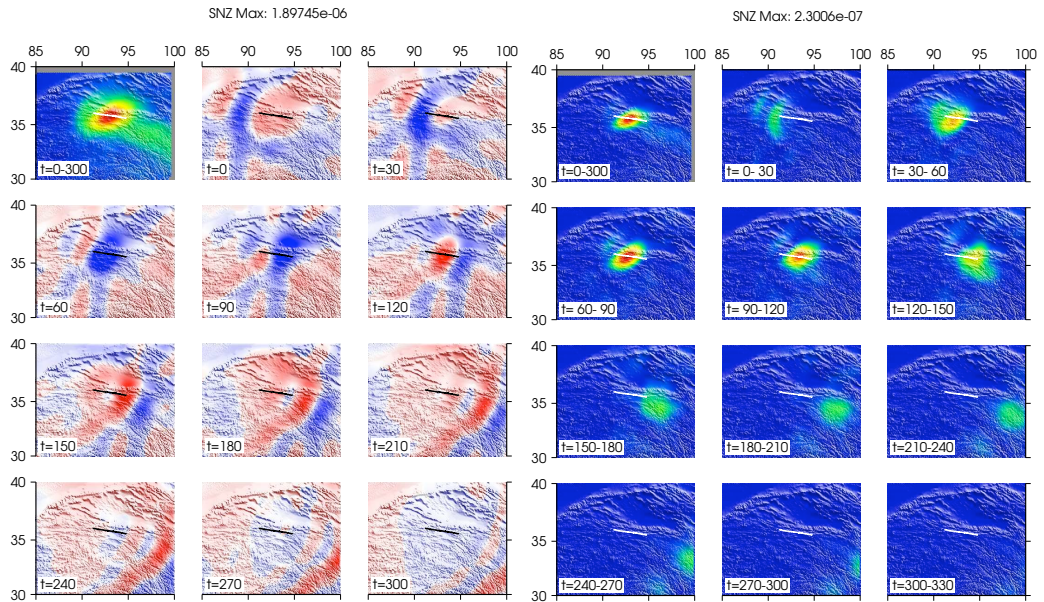


Figure 6.16: Left: Snapshots of the integral of the adjoint strain (component NZ) for the Kunlun earthquake. Right: Envelope of adjoint strain (component NZ), squared and integrated over the given time windows. The slices are all plotted on the same scale (except the top left one), and the maximum value is given in the title. The bold line indicates the fault trace (*Xu et al.*, 2006). For more detail see section 6.5.1.

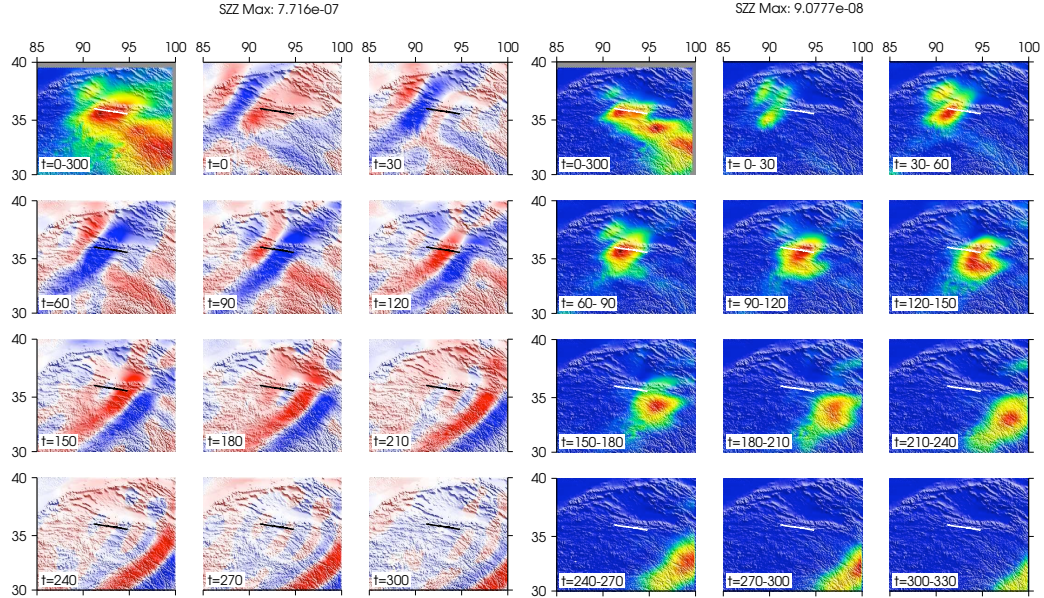


Figure 6.17: Left: Snapshots of the integral of the adjoint strain (component ZZ) for the Kunlun earthquake. Right: Envelope of adjoint strain (component ZZ), squared and integrated over the given time windows. The slices are all plotted on the same scale (except the top left one), and the maximum value is given in the title. The bold line indicates the fault trace (*Xu et al.*, 2006). For more detail see section 6.5.1.

6.5.5 Application to the 1998 Balleny Islands earthquake

The 1998 Balleny Island earthquake ruptured unilaterally from the east to west, over a duration of about 100 seconds. The mechanism is debated, but left-lateral slip on a southward dipping fault plane is advocated by several researchers (for more discussion see chapter 4 this thesis). The highest moment-rate was observed at around 60 seconds after the initiation of rupture. The orientation of the fault is very similar as to the Kunlun earthquake, with a fault normal is $\hat{\nu} = (a\hat{\mathbf{N}} + b\hat{\mathbf{Z}})$ with $a > b$ and the slip vector is $\hat{\sigma} = (c\hat{\mathbf{E}} + d\hat{\mathbf{Z}})$ with $c > d$. We therefore expect the large on-fault strains to be the NE , the EZ , NZ and the ZZ components.

The time reversed field for the Balleny Islands earthquake is shown in Figs. 6.18-6.23. The adjoint strain shows an eastward propagation, with large on fault strains for the EE , EZ , NE and NN components. The other components have larger off-faults strains. The largest strains are observed during the first 60 seconds.

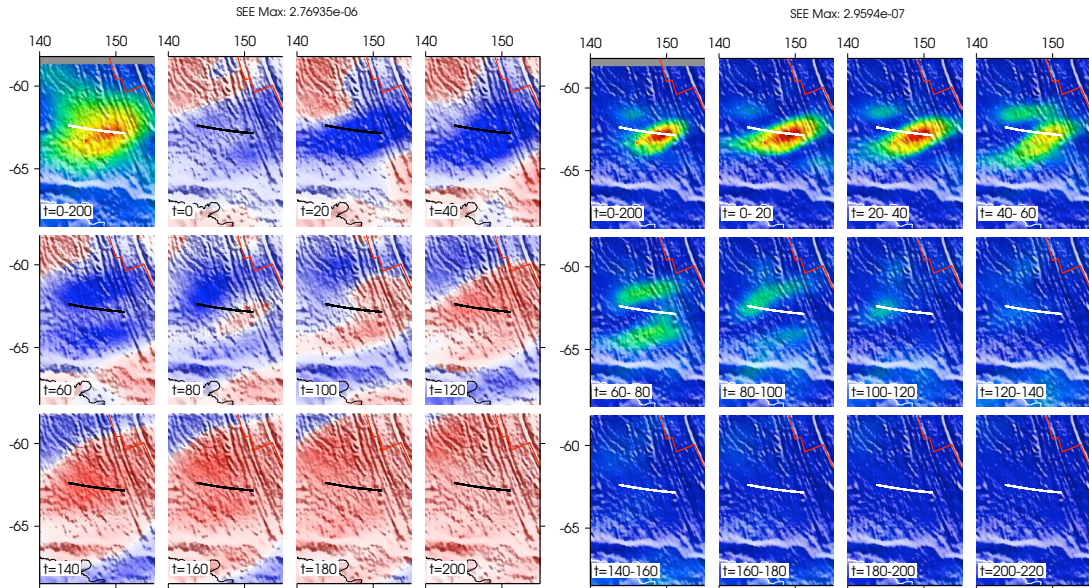


Figure 6.18: Left: Snapshots of the integral of the adjoint strain (component EE) for the Balleny Islands earthquake. Right: Envelope of adjoint strain (component EE), squared and integrated over the given time windows. The slices are all plotted on the same scale (except the top left one), and the maximum value is given in the title. The bold line indicates the fault trace used in Chapter 4. For more detail see section 6.5.1.

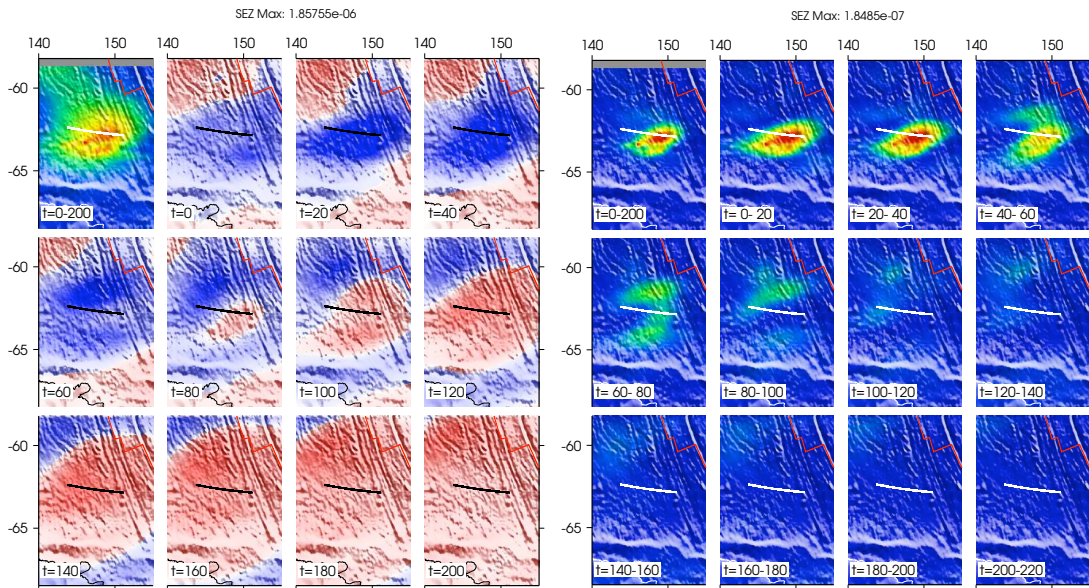


Figure 6.19: Left: Snapshots of the integral of the adjoint strain (component EZ) for the Balleny Islands earthquake. Right: Envelope of adjoint strain (component EZ), squared and integrated over the given time windows. The slices are all plotted on the same scale (except the top left one), and the maximum value is given in the title. The bold line indicates the fault trace used in Chapter 4. For more detail see section 6.5.1.

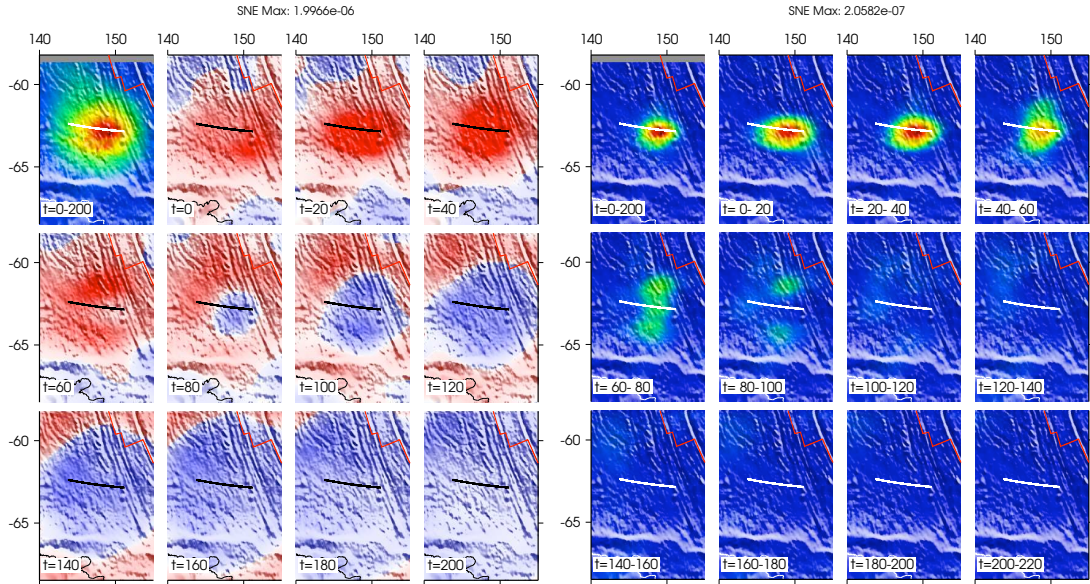


Figure 6.20: Left: Snapshots of the integral of the adjoint strain (component NE) for the Balleny Islands earthquake. Right: Envelope of adjoint strain (component NE), squared and integrated over the given time windows. The slices are all plotted on the same scale (except the top left one), and the maximum value is given in the title. The bold line indicates the fault trace used in Chapter 4. For more detail see section 6.5.1.

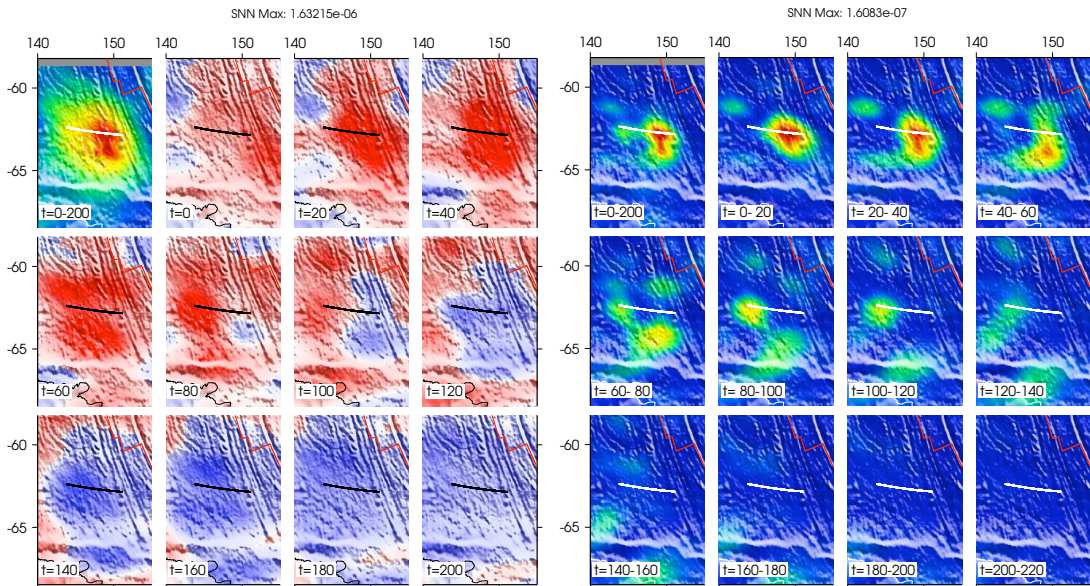


Figure 6.21: Left: Snapshots of the integral of the adjoint strain (component NN) for the Balleny Islands earthquake. Right: Envelope of adjoint strain (component NN), squared and integrated over the given time windows. The slices are all plotted on the same scale (except the top left one), and the maximum value is given in the title. The bold line indicates the fault trace used in Chapter 4. For more detail see section 6.5.1.

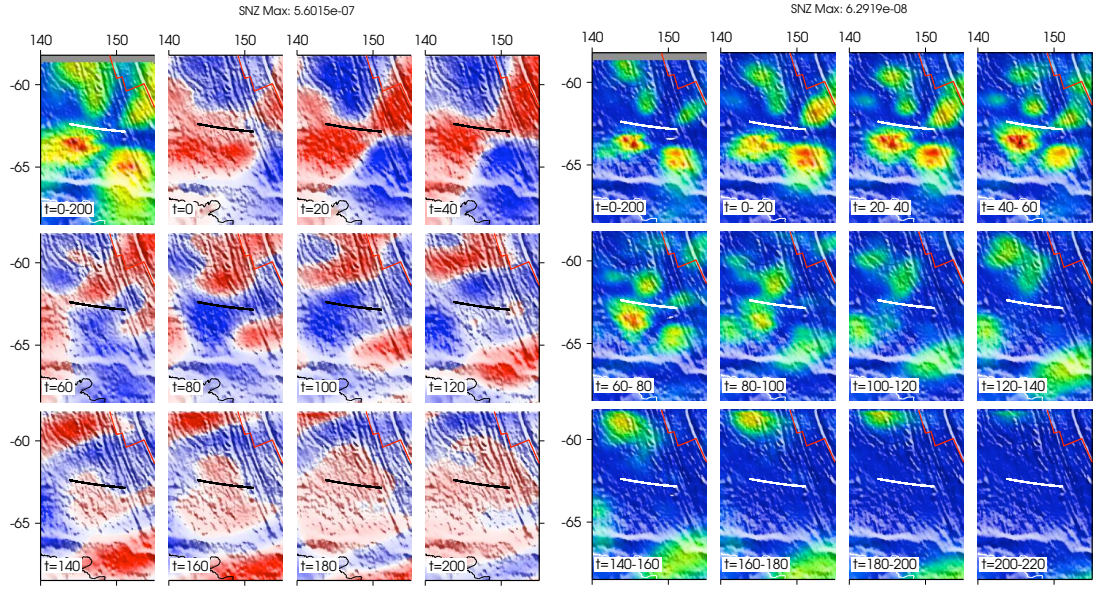


Figure 6.22: Left: Snapshots of the integral of the adjoint strain (component NZ) for the Balleny Islands earthquake. Right: Envelope of adjoint strain (component NZ), squared and integrated over the given time windows. The slices are all plotted on the same scale (except the top left one), and the maximum value is given in the title. The bold line indicates the fault trace used in Chapter 4. For more detail see section 6.5.1.

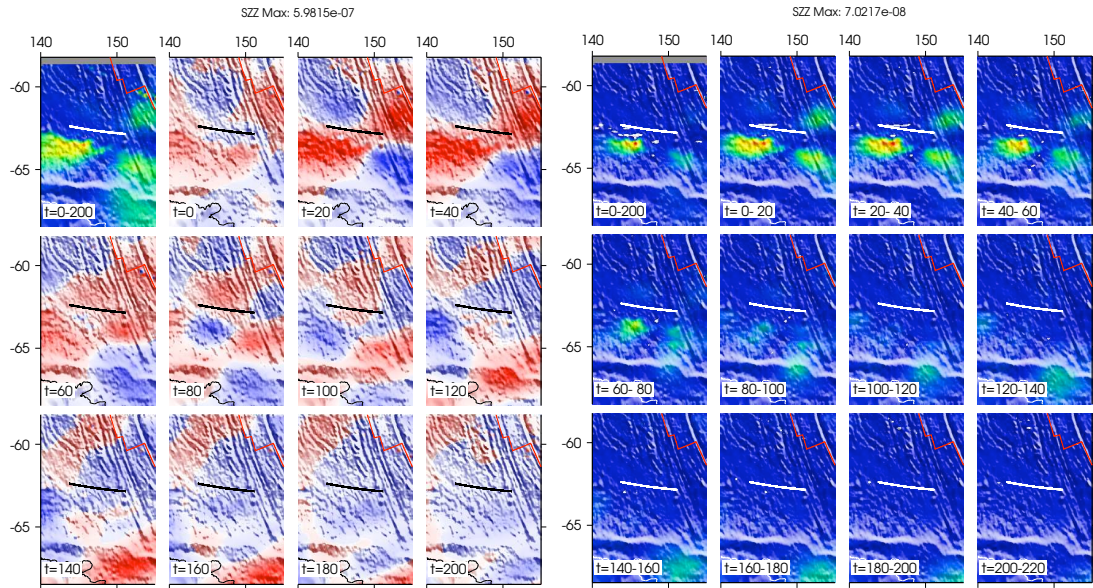


Figure 6.23: Left: Snapshots of the integral of the adjoint strain (component ZZ) for the Balleny Islands earthquake. Right: Envelope of adjoint strain (component ZZ), squared and integrated over the given time windows. The slices are all plotted on the same scale (except the top left one), and the maximum value is given in the title. The bold line indicates the fault trace used in Chapter 4. For more detail see section 6.5.1.

6.6 Conclusions and future direction

We have discussed the theory of an adjoint source inversion and detailed how it can be applied, for several source parameterizations. We have examined the connections between adjoint methods, time-reversal imaging and stacking. We have applied time-reversal imaging to a high frequency data set, from the Japanese Hinet array, and compared to results from stacking. We further applied time-reversal imaging to full waveforms from three large earthquakes, back-propagating them through a 3D synthetic model, accurate at periods of 60 seconds and longer. The resulting adjoint strains show the propagation of rupture on the fault plane, indicating the feasibility of using them in an adjoint source inversion. The maps of integrated adjoint strain give us an indication of the location (in space and time) of slip without any a priori assumptions on the fault parameters. These maps can be used to choose a fault parameterization, which can then be used to take the next step in an adjoint inversion.

We have made several choices along the way that affect the evaluation of the gradient of the misfit function. We chose to use a waveform misfit, but alternatively we could have used a travel time or amplitude misfit. We also chose to use the whole waveform, but we could have chosen to use several different windows with different weights. The filtering of data is also important, and it would be of interest to use higher frequency data to obtain more detail. The limitation is that the 3D Earth model used should be able to produce synthetics that accurately match the data in the chosen time and frequency windows. Other choices to be made are the fault parameterization and the specific gradient-based inverse method to use.

In cases where the 3D models do not accurately account for the structure, corrections can be applied to the adjoint sources before back-propagation. An example of that was given for the time-reversal imaging of the Hinet dataset, where the data were shifted and multiplied before back-propagating. One could also imagine a setting where a smaller “calibration” event could be used obtain corrections to certain phases, that could be applied to the data before back-propagating.

By using adjoint methods to obtain finite-fault source models, we can efficiently account for the Earth’s 3D structure in the modeling, allowing us to use a larger portion of the seismogram. This in turn can help reduce some of the trade-offs plaguing finite fault modeling.

The next step in this line of research would be to carry out the inversion, using one of the gradient based methods, such as the conjugate gradient one. The maps of the adjoint strain for the Kunlun and Balleny earthquakes in particular show good promise for applying this technique. The adjoint method gives us a new way of viewing the inverse problem, allowing for inclusion of data that is dependent on the Earth's 3D structure, that could provide us with more details about the slip-history of earthquakes. By better constraining the kinematic slip models we can provide better constraints on parameters important for rupture dynamics, for example the rupture speed and the continuity of slip.

6.7 Acknowledgments

We thank Mizuho Ishida and Masako Sakanashi at the National Institute for Earth Science and Disaster Prevention (NEID), Japan for providing us with the Hinet data used in this study.

Appendix A

Quantifying differences between two time series: Multitaper measurements

We quantify the difference between data and synthetics in terms of a transfer function. We use a multitaper measurement technique (*Thomson, 1982*), based upon prolate spheroidal eigentapers (*Slepian, 1978*). This method was first applied to geophysical applications by *Park et al. (1987)*. The following is based on the treatment by *Laske and Masters (1996)* and *Zhou (2004)*. Another useful discussion of multitaper measurements can be found in *Percival and Walden (1993)*, p 333–347.

We wish to quantify the differences between two time series. We start with a data trace $d(t)$ and a corresponding synthetic trace $s(t)$. We want to compare individual phases in the seismograms. More specifically, we want to estimate the time shift and amplitude ratio between the traces, as a function of frequency, within a given time window. We quantify the difference between the data and synthetics in terms of a transfer function, $T(f)$, that satisfies

$$[d(f) - T(f)s(f)]^2 = \text{minimum} \quad (\text{A.1})$$

In this case the solution is just:

$$T(f) = \frac{d(f)}{s(f)}. \quad (\text{A.2})$$

Writing the synthetic as $s = Ae^{-i\tau}$ and the data as $d = [A + \delta A]e^{-i[\tau + \delta\tau]}$ we can write:

$$d = Ts = s[1 + \delta A/A]e^{-i\delta\tau} \quad (\text{A.3})$$

with $T = [1 + \delta \ln A]e^{-i\delta\tau}$. In the Born approximation $d = s + \delta s$, and thus $T = 1 + \delta T$ where $\delta T = \delta s/s$. For small $\delta\tau$ we have $e^{-i\delta\tau} \approx 1 - i\delta\tau$. Correct to first order in small perturbations:

$$\delta T = T - 1 = [1 + \delta \ln A][1 - i\delta\tau] - 1 \approx \delta \ln A - i\delta\tau \quad (\text{A.4})$$

and finally

$$\delta\tau = -\text{Im}\left(\frac{\delta s}{s}\right), \quad \delta \ln A = \text{Re}\left(\frac{\delta s}{s}\right) \quad (\text{A.5})$$

A.1 Multitaper measurements

In the discussion above we did not specify the type of window to use. Care has to be taken when windowing, as the type of window can affect the measurement, due to spectral leakage. This is a well-known problem in signal processing, as windowing in the time domain corresponds to convolution of the Fourier transform of the windowing function in the frequency domain. Denoting the window in the time domain by $h(t)$ and in the frequency domain by $h(f)$ the windowed data becomes

$$d_w(t) = h(t)d(t) \quad (\text{A.6})$$

or in the frequency domain

$$d_w(f) = h(f) \otimes d(f) \quad (\text{A.7})$$

where \otimes denotes convolution. To get an accurate estimate $d_w(f)$ of $d(f)$ we want $h(f)$ to be as close to a delta function as possible. If we choose $h(t)$ to be a boxcar, then $h(f)$ is a sinc-function (Fig. A.1). When we convolve $d(f)$ with the sinc-function, its side lobes cause the spectral values away from f to contribute to the estimated value at f . This example suggests we should choose a windowing function without side lobes in the frequency domain, such as a cosine taper. This choice reduces the spectral leakage, but it creates a new problem, as the signal in the middle of the window is weighted more heavily than the signal at the edges, thereby biasing the measurement. In order to minimize the spectral leakage while keeping the bias at a minimum, we use a multitaper measurement technique (*Thomson*, 1982). This technique uses several tapers, $h_j(t)$, all concentrated within a small window in the frequency domain, without side lobes, to window the data and the synthetics. We denote

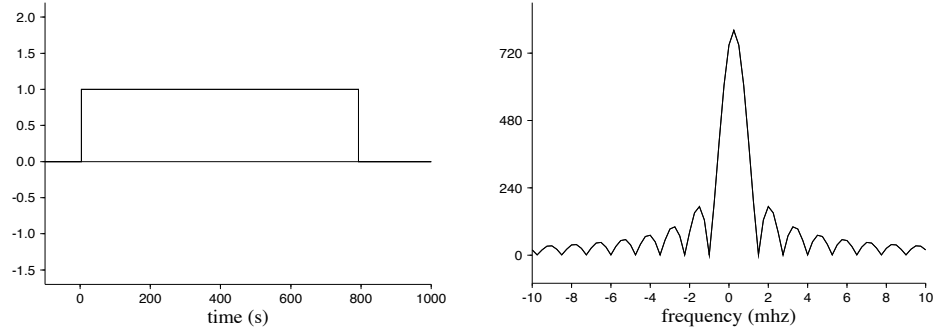


Figure A.1: The time and frequency versions of a boxcar.

the data windowed by the j th taper by $d_j(f)$ and the corresponding windowed synthetic by $s_j(f)$. The basic idea is that even though the spectra from each of the windowed traces is biased, by using orthogonal tapers and averaging the spectra one gets a less biased final spectral estimate. An added benefit is that since we get several estimates for each spectral measurement we can compute the error in the estimate, in addition to the average.

A.2 Prolate spheroidal eigentapers

Now we focus our efforts on finding the ideal tapers (or windows) that have compact support in the frequency domain while still sampling a large part of the trace in the time domain. Suppose we have chosen a measurement window with width

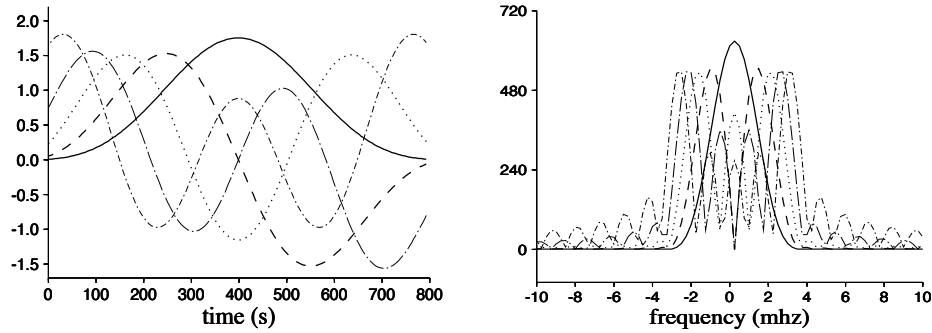
$$L = N\Delta t, \tag{A.8}$$

where L denotes the length of the time window, Δt the sampling rate, and N the number of time samples contained in the window. The Rayleigh frequency is then

$$f_R = \frac{1}{L} = \frac{1}{N\Delta t}. \tag{A.9}$$

This is the lowest frequency, i.e., the longest period, that we can hope to resolve with a window length L . The highest frequency, i.e., shortest period, that we can resolve is determined by the Nyquist frequency:

$$f_c = \frac{1}{2\Delta t}. \tag{A.10}$$

Figure A.2: The first five 2.5π tapers.

The frequency content of our time window $[0, L]$ lies between $[-f_c, f_c]$. The frequency spacing Δf is equal to the Rayleigh frequency:

$$\Delta f = \frac{2f_c}{N} = \frac{1}{N\Delta t} = f_R. \quad (\text{A.11})$$

Our objective is to find functions (tapers) that are optimally concentrated within the window W in the frequency domain. For convenience we define the window width in terms of the Rayleigh frequency f_R , such that $W = kf_R$. Now our objective is accomplished by optimizing the quantity

$$\lambda = \frac{\int_{-W}^W |h(f)|^2 df}{\int_{-f_c}^{f_c} |h(f)|^2 df}. \quad (\text{A.12})$$

This leads to an eigenvalue problem with eigenvalues λ_j and associated eigenfunctions (“prolate multitapers”) $h_j(f)$ (Slepian, 1978). A remarkable property of the eigenvalues λ_j is that the first $2k = 2LW$ values are ~ 1 , and the remaining eigenvalues quickly drop off to zero. The implication is that only the first $2k$ eigentapers are optimally concentrated in the window W . So for small k the window is narrow, and for large k it is wider. Similarly, for a long time window L the frequency window W is narrower, and for a short time window L the frequency window W is wider. Effectively one is choosing the width W around the target frequency of interest over which you are going to average the measurement. Frequently the tapers are referred to in terms of their k in the form “ $k \pi$ tapers” (“ π ” for prolate).

Next, one uses the multitapers as windowing functions. Suppose we have a time series $s(t)$ with a corresponding spectrum $s(f)$. Now, rather than working with the time series directly, we multiply it by the $2k$ multitapers to get $2k$ versions of the time series:

$$s_j(t) = h_j(t)s(t), \quad j = 1, \dots, 2k. \quad (\text{A.13})$$

In the frequency domain, this corresponds to a convolution with the frequency-version of the taper, leading to $2k$ spectral estimates:

$$s_j(f) = s(f) \otimes h_j(f) = \int_{-f_c}^{f_c} s(f')h_j(f - f') df', \quad j = 1, \dots, 2k. \quad (\text{A.14})$$

Here one can really see how the spectrum $s(f')$ is convolved with the taper centered on f' , $h_j(f - f')$. So the wider the bandwidth of h_j , i.e., the wider W , the more we average over neighboring frequencies. In the limit $k \rightarrow 0$ we get a delta function, which corresponds to an infinite boxcar taper in the time domain.

A.3 Transfer function for multitaper measurements

Now that we have made a choice of windowing function, we can go back to estimating the transfer function $T(f)$. In this case we wish to find $T(f)$ such that:

$$\|\mathbf{d}(f) - T(f)\mathbf{s}(f)\|^2 = \text{minimum} \quad (\text{A.15})$$

where $\mathbf{d}(f) = [d_1(f), \dots, d_j(f), \dots, d_{2k}(f)]^T$ is a $2k$ -dimensional vector that contains the $2k$ spectral estimates $d_j(f) = d(f) \otimes h_j(f)$. The solution is given by $\mathbf{s}^T[\mathbf{d} - T\mathbf{s}] = 0$, i.e.,

$$T = \frac{\sum_{j=1}^{2k} d_j s_j^*}{\sum_{j=1}^{2k} s_j s_j^*} \quad (\text{A.16})$$

Now we have $T = \mathbf{s}^T \mathbf{d} / \mathbf{s}^T \mathbf{s} = \mathbf{s}^T (\mathbf{s} + \delta \mathbf{s}) / \mathbf{s}^T \mathbf{s}$ or with $T = 1 + \delta T$:

$$\delta T = \frac{\sum_{j=1}^{2k} \delta s_j s_j^*}{\sum_{j=1}^{2k} s_j s_j^*} \quad (\text{A.17})$$

Remembering eq. (A.4) we get the expressions:

$$\delta \tau = -\text{Im} \left[\frac{\sum_{j=1}^{2k} \delta s_j s_j^*}{\sum_{j=1}^{2k} s_j s_j^*} \right], \quad \delta \ln A = \text{Re} \left[\frac{\sum_{j=1}^{2k} \delta s_j s_j^*}{\sum_{j=1}^{2k} s_j s_j^*} \right] \quad (\text{A.18})$$

A.4 Effect of taper parameters

The main parameter controlling the behavior of the taper is k . Figures (A.3)-(A.4) illustrate the effect of k . We use the first five prolate spheroidal tapers to estimate the spectra. The spectra of these tapers are localized within $2.5/L$ where L is the length of the time series. Remembering equation (A.7), this leads to independent estimates of the true spectra every $2.5/L$ Hz. For a window length of 800 s this corresponds to independent estimates every $2.5/800 = 0.003125$ Hz.

A.5 Combining measurements

Each multitaper measurement gives us an estimate of the time shift, $\delta\tau_i(f)$, and the amplitude anomaly, $\delta \ln A_i(f)$, at station i and frequency f . This provides us with oodles of measurements for each run. In order to visualize the results we combine the measurements, either integrating over all frequencies at a given station and to see the variation with receiver location or summing all the measurements at a given frequency over stations to see the variation with frequency. We define the average time shift at a given frequency as:

$$\overline{\delta\tau}(f) = \frac{1}{N} \sum_{i=1}^N \delta\tau_i(f) \quad (\text{A.19})$$

and the average time shift at station i :

$$\overline{\delta\tau}_i = \frac{1}{f_1 - f_0} \int_{f_0}^{f_1} \delta\tau_i(f) df \quad (\text{A.20})$$

finally, the average over all measurements is given by:

$$\overline{\delta\tau} = \frac{1}{N} \sum_{i=1}^N \frac{1}{f_1 - f_0} \int_{f_0}^{f_1} \delta\tau_i(f) df \quad (\text{A.21})$$

It can also be of interest to see how much the data varies around the average value. Since each measurement is not independent of the adjacent values, and is not normally distributed, these are not the standard deviations in the language of statistics, but is the second moment

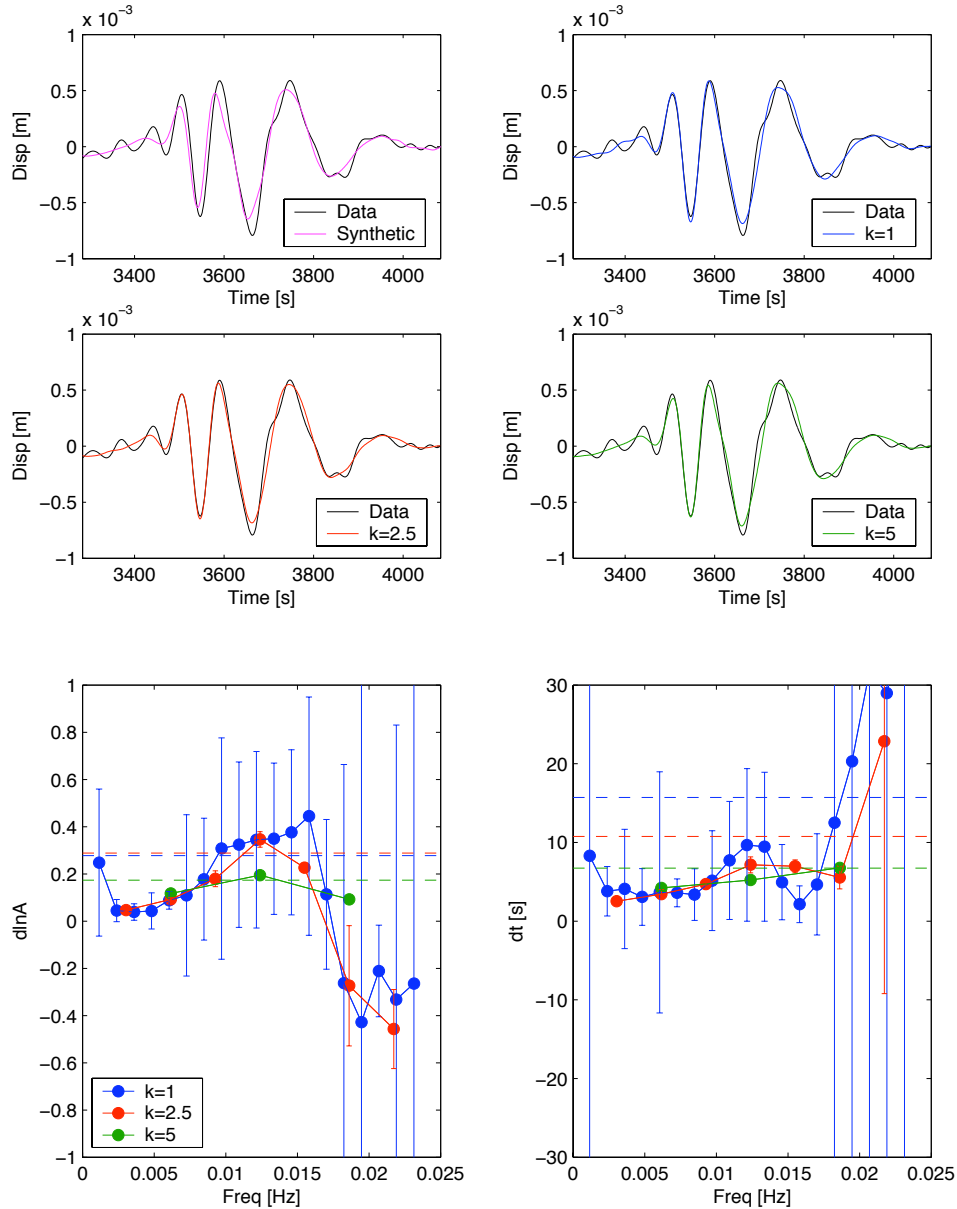
PFO.II Az: 6.64° Δ : 122° 

Figure A.3: The effect of changing k for a fixed window length. The observed (black) and synthetic (magenta) traces are shown at the top left. The other waveform plots compare the data to the reconstructed seismograms for various k . The multitaper measurements, with error bars, are shown on the left, the square of the measurements is shown on the right. The colored lines represent measurements made using different k . The number of tapers is set to $2k$. Here we only show measurements that are “independent,” or k/L apart in the frequency domain. Notice how small values of k give many measurements with high variance, and large values of k give few measurements (in the case of $k=5$, only three measurements), but small variance. Fig. A.4 shows the same, for $k=2, 2.5, 3$.

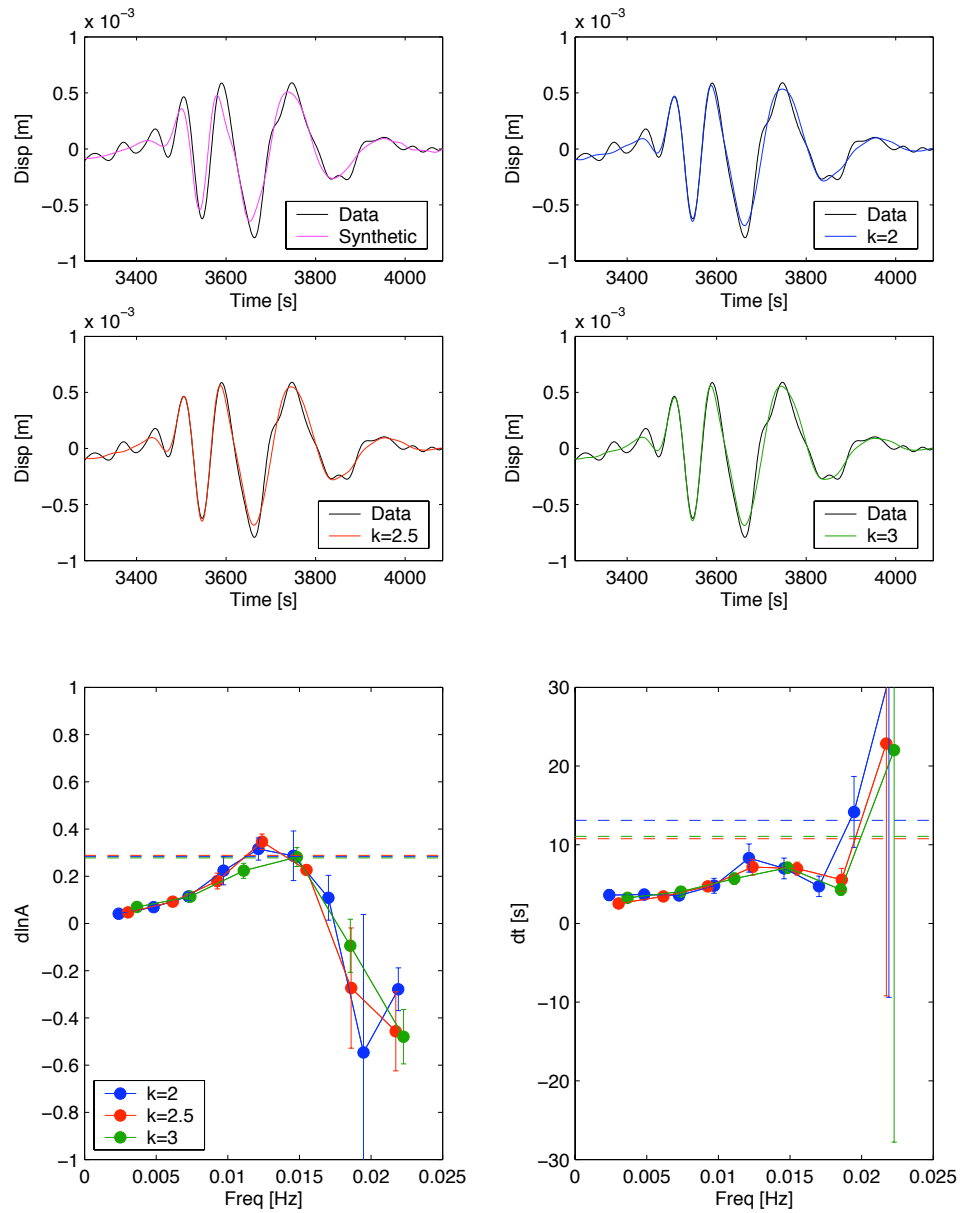
PFO.II Az: 6.64° Δ : 122° 

Figure A.4: The effect of changing k for a fixed window length. Same as Fig. A.3 except other values of k .

of the measurements around the mean. We define the variations around the averages as:

$$\sigma^\tau(f) = \sqrt{\frac{1}{N} \sum_{i=1}^N (\delta\tau_i(f) - \overline{\delta\tau}(f))^2} \quad (\text{A.22})$$

and the average time-shift at station i :

$$\sigma_i^\tau = \sqrt{\frac{1}{f_1 - f_0} \int_{f_0}^{f_1} (\delta\tau_i(f) - \overline{\delta\tau}_i)^2 df} \quad (\text{A.23})$$

finally, the average over all measurements is given by:

$$\sigma^\tau = \sqrt{\frac{1}{N} \sum_{i=1}^N \frac{1}{f_1 - f_0} \int_{f_0}^{f_1} (\delta\tau_i(f) - \overline{\delta\tau})^2 df} \quad (\text{A.24})$$

For the amplitudes, we define $\overline{\delta \ln A}(f)$, $\overline{\delta \ln A}_i$, $\overline{\delta \ln A}$, $\sigma^{\ln A}(f)$, $\sigma_i^{\ln A}$, $\sigma^{\ln A}$ in the same manner.

Appendix B

Fault-Plane Kernels

In this appendix we give explicit expressions for the finite-fault kernels $K_{\Delta s}$, K_γ , K_i , K_ζ , and K_h . The variation of the moment-density tensor (6.25) with respect to the scalar moment density $\mu\Delta s$, the rake angle γ , and the dip and strike angles i and ζ , which control the orientation of the local fault plane, is given by

$$\begin{aligned}
\delta\mathbf{m} = & [\sin 2i \sin \gamma \hat{\mathbf{r}}\hat{\mathbf{r}} - (\sin i \cos \gamma \sin 2\zeta + \sin 2i \sin \gamma \sin^2 \zeta) \hat{\boldsymbol{\theta}}\hat{\boldsymbol{\theta}} + (\sin i \cos \gamma \sin 2\zeta - \sin 2i \sin \gamma \cos^2 \zeta) \hat{\boldsymbol{\phi}}\hat{\boldsymbol{\phi}} \\
& - (\cos i \cos \gamma \cos \zeta + \cos 2i \sin \gamma \sin \zeta) (\hat{\mathbf{r}}\hat{\boldsymbol{\theta}} + \hat{\boldsymbol{\theta}}\hat{\mathbf{r}}) + (\cos i \cos \gamma \sin \zeta - \cos 2i \sin \gamma \cos \zeta) (\hat{\mathbf{r}}\hat{\boldsymbol{\phi}} + \hat{\boldsymbol{\phi}}\hat{\mathbf{r}}) \\
& - (\sin i \cos \gamma \cos 2\zeta + \frac{1}{2} \sin 2i \sin \gamma \sin 2\zeta) (\hat{\boldsymbol{\theta}}\hat{\boldsymbol{\phi}} + \hat{\boldsymbol{\phi}}\hat{\boldsymbol{\theta}})] \delta(\mu\Delta s) \\
& + \mu\Delta s [\sin 2i \cos \gamma \hat{\mathbf{r}}\hat{\mathbf{r}} + (\sin i \sin \gamma \sin 2\zeta - \sin 2i \cos \gamma \sin^2 \zeta) \hat{\boldsymbol{\theta}}\hat{\boldsymbol{\theta}} \\
& - (\sin i \sin \gamma \sin 2\zeta + \sin 2i \cos \gamma \cos^2 \zeta) \hat{\boldsymbol{\phi}}\hat{\boldsymbol{\phi}} \\
& + (\cos i \sin \gamma \cos \zeta - \cos 2i \cos \gamma \sin \zeta) (\hat{\mathbf{r}}\hat{\boldsymbol{\theta}} + \hat{\boldsymbol{\theta}}\hat{\mathbf{r}}) - (\cos i \sin \gamma \sin \zeta + \cos 2i \cos \gamma \cos \zeta) (\hat{\mathbf{r}}\hat{\boldsymbol{\phi}} + \hat{\boldsymbol{\phi}}\hat{\mathbf{r}}) \\
& + (\sin i \sin \gamma \cos 2\zeta - \frac{1}{2} \sin 2i \cos \gamma \sin 2\zeta) (\hat{\boldsymbol{\theta}}\hat{\boldsymbol{\phi}} + \hat{\boldsymbol{\phi}}\hat{\boldsymbol{\theta}})] \delta\gamma \\
& + \mu\Delta s [2 \cos 2i \sin \gamma \hat{\mathbf{r}}\hat{\mathbf{r}} - (\cos i \cos \gamma \sin 2\zeta + 2 \cos 2i \sin \gamma \sin^2 \zeta) \hat{\boldsymbol{\theta}}\hat{\boldsymbol{\theta}} \\
& + (\cos i \cos \gamma \sin 2\zeta - 2 \cos 2i \sin \gamma \cos^2 \zeta) \hat{\boldsymbol{\phi}}\hat{\boldsymbol{\phi}} \\
& + (\sin i \cos \gamma \cos \zeta + 2 \sin 2i \sin \gamma \sin \zeta) (\hat{\mathbf{r}}\hat{\boldsymbol{\theta}} + \hat{\boldsymbol{\theta}}\hat{\mathbf{r}}) - (\sin i \cos \gamma \sin \zeta - 2 \sin 2i \sin \gamma \cos \zeta) (\hat{\mathbf{r}}\hat{\boldsymbol{\phi}} + \hat{\boldsymbol{\phi}}\hat{\mathbf{r}}) \\
& - (\cos i \cos \gamma \cos 2\zeta + \cos 2i \sin \gamma \sin 2\zeta) (\hat{\boldsymbol{\theta}}\hat{\boldsymbol{\phi}} + \hat{\boldsymbol{\phi}}\hat{\boldsymbol{\theta}})] \delta i \\
& + \mu\Delta s [(2 \sin i \cos \gamma \cos 2\zeta + \sin 2i \sin \gamma \sin 2\zeta) (\hat{\boldsymbol{\phi}}\hat{\boldsymbol{\phi}} - \hat{\boldsymbol{\theta}}\hat{\boldsymbol{\theta}}) \\
& + (\cos i \cos \gamma \sin \zeta - \cos 2i \sin \gamma \cos \zeta) (\hat{\mathbf{r}}\hat{\boldsymbol{\theta}} + \hat{\boldsymbol{\theta}}\hat{\mathbf{r}}) + (\cos i \cos \gamma \cos \zeta + \cos 2i \sin \gamma \sin \zeta) (\hat{\mathbf{r}}\hat{\boldsymbol{\phi}} + \hat{\boldsymbol{\phi}}\hat{\mathbf{r}}) \\
& + (2 \sin i \cos \gamma \sin 2\zeta - \sin 2i \sin \gamma \cos 2\zeta) (\hat{\boldsymbol{\theta}}\hat{\boldsymbol{\phi}} + \hat{\boldsymbol{\phi}}\hat{\boldsymbol{\theta}})] \delta\zeta. \tag{B.1}
\end{aligned}$$

Therefore, the Fréchet derivative (6.14) may be rewritten in the form (6.26), where

$$\begin{aligned}
K_{\Delta s} = \boldsymbol{\varepsilon}^\dagger : & [\sin 2i \sin \gamma \hat{\mathbf{r}}\hat{\mathbf{r}} - (\sin i \cos \gamma \sin 2\zeta + \sin 2i \sin \gamma \sin^2 \zeta) \hat{\boldsymbol{\theta}}\hat{\boldsymbol{\theta}} \\
& + (\sin i \cos \gamma \sin 2\zeta - \sin 2i \sin \gamma \cos^2 \zeta) \hat{\boldsymbol{\phi}}\hat{\boldsymbol{\phi}}
\end{aligned}$$

$$\begin{aligned}
& - (\cos i \cos \gamma \cos \zeta + \cos 2i \sin \gamma \sin \zeta)(\hat{\mathbf{r}}\hat{\boldsymbol{\theta}} + \hat{\boldsymbol{\theta}}\hat{\mathbf{r}}) + (\cos i \cos \gamma \sin \zeta - \cos 2i \sin \gamma \cos \zeta)(\hat{\mathbf{r}}\hat{\boldsymbol{\phi}} + \hat{\boldsymbol{\phi}}\hat{\mathbf{r}}) \\
& - (\sin i \cos \gamma \cos 2\zeta + \frac{1}{2} \sin 2i \sin \gamma \sin 2\zeta)(\hat{\boldsymbol{\theta}}\hat{\boldsymbol{\phi}} + \hat{\boldsymbol{\phi}}\hat{\boldsymbol{\theta}})], \tag{B.2}
\end{aligned}$$

$$\begin{aligned}
K_\gamma &= \int_0^T \boldsymbol{\varepsilon}^\dagger(T-t) : [\sin 2i \cos \gamma \hat{\mathbf{r}}\hat{\mathbf{r}} + (\sin i \sin \gamma \sin 2\zeta - \sin 2i \cos \gamma \sin^2 \zeta)\hat{\boldsymbol{\theta}}\hat{\boldsymbol{\theta}} \\
& - (\sin i \sin \gamma \sin 2\zeta + \sin 2i \cos \gamma \cos^2 \zeta)\hat{\boldsymbol{\phi}}\hat{\boldsymbol{\phi}} + (\cos i \sin \gamma \cos \zeta - \cos 2i \cos \gamma \sin \zeta)(\hat{\mathbf{r}}\hat{\boldsymbol{\theta}} + \hat{\boldsymbol{\theta}}\hat{\mathbf{r}}) \\
& - (\cos i \sin \gamma \sin \zeta + \cos 2i \cos \gamma \cos \zeta)(\hat{\mathbf{r}}\hat{\boldsymbol{\phi}} + \hat{\boldsymbol{\phi}}\hat{\mathbf{r}}) \\
& + (\sin i \sin \gamma \cos 2\zeta - \frac{1}{2} \sin 2i \cos \gamma \sin 2\zeta)(\hat{\boldsymbol{\theta}}\hat{\boldsymbol{\phi}} + \hat{\boldsymbol{\phi}}\hat{\boldsymbol{\theta}})] \mu \Delta s(t) dt, \tag{B.3}
\end{aligned}$$

$$\begin{aligned}
K_i &= \int_0^T \boldsymbol{\varepsilon}^\dagger(T-t) : [2 \cos 2i \sin \gamma \hat{\mathbf{r}}\hat{\mathbf{r}} - (\cos i \cos \gamma \sin 2\zeta + 2 \cos 2i \sin \gamma \sin^2 \zeta)\hat{\boldsymbol{\theta}}\hat{\boldsymbol{\theta}} \\
& + (\cos i \cos \gamma \sin 2\zeta - 2 \cos 2i \sin \gamma \cos^2 \zeta)\hat{\boldsymbol{\phi}}\hat{\boldsymbol{\phi}} + (\sin i \cos \gamma \cos \zeta + 2 \sin 2i \sin \gamma \sin \zeta)(\hat{\mathbf{r}}\hat{\boldsymbol{\theta}} + \hat{\boldsymbol{\theta}}\hat{\mathbf{r}}) \\
& - (\sin i \cos \gamma \sin \zeta - 2 \sin 2i \sin \gamma \cos \zeta)(\hat{\mathbf{r}}\hat{\boldsymbol{\phi}} + \hat{\boldsymbol{\phi}}\hat{\mathbf{r}}) \\
& - (\cos i \cos \gamma \cos 2\zeta + \cos 2i \sin \gamma \sin 2\zeta)(\hat{\boldsymbol{\theta}}\hat{\boldsymbol{\phi}} + \hat{\boldsymbol{\phi}}\hat{\boldsymbol{\theta}})] \mu \Delta s(t) dt, \tag{B.4}
\end{aligned}$$

$$\begin{aligned}
K_\zeta &= \int_0^T \boldsymbol{\varepsilon}^\dagger(T-t) : [(2 \sin i \cos \gamma \cos 2\zeta + \sin 2i \sin \gamma \sin 2\zeta)(\hat{\boldsymbol{\phi}}\hat{\boldsymbol{\phi}} - \hat{\boldsymbol{\theta}}\hat{\boldsymbol{\theta}}) \\
& + (\cos i \cos \gamma \sin \zeta - \cos 2i \sin \gamma \cos \zeta)(\hat{\mathbf{r}}\hat{\boldsymbol{\theta}} + \hat{\boldsymbol{\theta}}\hat{\mathbf{r}}) + (\cos i \cos \gamma \cos \zeta + \cos 2i \sin \gamma \sin \zeta)(\hat{\mathbf{r}}\hat{\boldsymbol{\phi}} + \hat{\boldsymbol{\phi}}\hat{\mathbf{r}}) \\
& + (2 \sin i \cos \gamma \sin 2\zeta - \sin 2i \sin \gamma \cos 2\zeta)(\hat{\boldsymbol{\theta}}\hat{\boldsymbol{\phi}} + \hat{\boldsymbol{\phi}}\hat{\boldsymbol{\theta}})] \mu \Delta s(t) dt, \tag{B.5}
\end{aligned}$$

$$\begin{aligned}
K_h &= \int_0^T \partial_\nu \boldsymbol{\varepsilon}^\dagger(\mathbf{r}, T-t) : [\sin 2i \sin \gamma \hat{\mathbf{r}}\hat{\mathbf{r}} - (\sin i \cos \gamma \sin 2\zeta + \sin 2i \sin \gamma \sin^2 \zeta)\hat{\boldsymbol{\theta}}\hat{\boldsymbol{\theta}} \\
& + (\sin i \cos \gamma \sin 2\zeta - \sin 2i \sin \gamma \cos^2 \zeta)\hat{\boldsymbol{\phi}}\hat{\boldsymbol{\phi}} - (\cos i \cos \gamma \cos \zeta + \cos 2i \sin \gamma \sin \zeta)(\hat{\mathbf{r}}\hat{\boldsymbol{\theta}} + \hat{\boldsymbol{\theta}}\hat{\mathbf{r}}) \\
& + (\cos i \cos \gamma \sin \zeta - \cos 2i \sin \gamma \cos \zeta)(\hat{\mathbf{r}}\hat{\boldsymbol{\phi}} + \hat{\boldsymbol{\phi}}\hat{\mathbf{r}}) \\
& - (\sin i \cos \gamma \cos 2\zeta + \frac{1}{2} \sin 2i \sin \gamma \sin 2\zeta)(\hat{\boldsymbol{\theta}}\hat{\boldsymbol{\phi}} + \hat{\boldsymbol{\phi}}\hat{\boldsymbol{\theta}})] \mu \Delta s(t) dt. \tag{B.6}
\end{aligned}$$

Bibliography

- Aki, K., and P. G. Richards (1980), *Quantitative Seismology, Theory and Methods*, W. H. Freeman, San Francisco, Calif.
- Ammon, C., et al. (2005), Rupture process of the 2004 Sumatra-Andaman earthquake, *Science*, *3*(5725), 1133–1139.
- Antolik, M., and D. S. Dreger (2003), Rupture process of the 26 January 2001 M_w 7.6 Bhuj, India, Earthquake from teleseismic broadband data, *Bull. Seismo. Soc. Am.*, *93*(3), 1235–1248.
- Antolik, M., A. Kaverina, and D. S. Dreger (2000), Compound rupture of the great 1998 Antarctic plate earthquake, *Jour. Geophys. Res.*, *105*(B10), 23,825–23,838.
- Antolik, M., R. A. Abercrombie, and G. Ekström (2004), The 14 November, 2001 Kokoxili (Kunlunshan), Tibet, earthquake: Rupture transfer through a large extensional step-over, *Bull. Seismo. Soc. Am.*, *94*(4), 1173–1194.
- Banerjee, P., F. Pollitz, and R. Bürgmann (2005), The size and duration of the Sumatra-Andaman earthquake from far-field static offsets, *Science*, doi:10.1126/science.1113746.
- Bassin, C., G. Laske, and G. Masters (2000), The current limits of resolution for surface wave tomography in North America, *EOS*, *81*(F897), also available at mahi.ucsd.edu/Gabi/crust2.html.
- Beck, S. L., and L. J. Ruff (1987), Rupture process of the great 1963 Kuril Islands earthquake sequence: Asperity interaction and multiple event rupture, *Jour. Geophys. Res.*, *92*(B13), 14,123–14,138.
- Ben-Menahem, A. (1961), Radiation of seismic surface-waves from finite moving sources, *Bull. Seismo. Soc. Am.*, *51*(3), 401–435.
- Ben-Menahem, A., and D. Harkrider (1964), Radiation patterns of seismic surface waves from buried dipolar point sources in a flat stratified Earth, *Jour. Geophys. Res.*, *69*, 2605–2620.
- Bilham, R., R. Engdahl, N. Feldl, and S. Satyabala (2005), Partial and complete rupture of the Indo-Andaman plate boundary 1847-2004, *Seismological Res. Lett.*, *76*, 299–311.

- Bouchon, M., and M. Vallée (2003), Observation of long supershear rupture during the magnitude 8.1 Kunlunshan earthquake, *Science*, *301*(5634), 824–826.
- Chang, W., and G. McMechan (1991), Wavefield extrapolation of body waves for 3-D imaging of earthquake sources, *Geophys. Jour. Int.*, *106*, 85–98.
- Chlieh, M., et al. (2007), Coseismic slip and afterslip of the great M_w 9.15 Sumatra-Andaman earthquake of 2004, *Bull. Seismo. Soc. Am.*, *97*(1A), S152–S173, doi:10.1785/0120050631.
- Dahlen, F., and J. Tromp (1998), *Theoretical Global Seismology*, Princeton University Press.
- Dziewonski, A. M., and D. L. Anderson (1981), Preliminary reference Earth model, *Phys. of Earth and Planetary Interiors*, *25*(4), 297–356.
- Ekström, G. (1989), A very broad band inversion method for the recovery of earthquake source parameters, *Tectonophysics*, *166*, 73–100.
- Ekström, G. (2006), Global detection and location of seismic sources by using surface waves, *Bull. Seismo. Soc. Am.*, *96*(4), 1201–1212.
- Ekström, G., A. M. Dziewonski, N. N. Maternovskaya, and M. Nettles (2003), Global seismicity of 2001: Centroid-moment tensor solutions for 961 earthquakes, *Phys. of Earth and Planetary Interiors*, *136*(3-4), 165–185, also available online at <http://www.seismology.harvard.edu/CMTsearch.html>.
- Eshelby, J. D. (1969), Elastic field of a crack extending non-uniformly under general anti-plane loading, *Journal of the mechanics and physics of solids*, *17*(3), 177.
- Fink, M. (1997), Time reversed acoustics, *Physics Today*, *50*(3), 34–40.
- Freund, L. B. (1972), Energy flux into the tip of an extending crack in an elastic solid, *Journal of Elasticity*, *2*(4), 341–349.
- Fu, B., Y. Awata, J. Du, Y. Ninomiya, and W. He (2005), Complex geometry and segmentation of the surface rupture associated with the 14 November 2001 great Kunlun earthquake, northern Tibet, China, *Tectonophysics*, *407*, 43–63.
- Fujii, Y., and K. Satake (2007), Tsunami source of the 2004 Sumatra-Andaman earthquake inferred from tide gauge and satellite data, *Bull. Seismo. Soc. Am.*, *97*(1A), S192–S207, doi:10.1785/0120050613.
- Gajewski, D., and E. Tessmer (2005), Reverse modelling for seismic event characterization, *Geophys. Jour. Int.*, *163*(1), 276–284, doi:10.1111/j.1365-246X.2005.02732.x.

- Gauthier, O., J. Virieux, and A. Tarantola (1986), Two-dimensional nonlinear inversion of seismic waveforms: Numerical results, *Geophysics*, *51*, 1387–1403.
- Gudmundsson, O., and M. Sambridge (1998), A regionalized upper mantle (RUM) seismic model, *Jour. Geophys. Res.*, *103*, 7121–7136.
- Henry, C., S. Das, and J. H. Woodhouse (2000), The great March 25, 1998, Antarctic Plate earthquake: Moment tensor and rupture history, *Jour. Geophys. Res.*, *105*(B7), 16,097–16,118.
- Ishii, M., P. Shearer, H. Houston, and J. Vidale (2005), Extent, duration and speed of the 2004 Sumatra-Andaman earthquake imaged by the Hi-Net array, *Nature*, *435*, doi:10.1038/nature03675.
- Ji, C. (2005), USGS Earthquake Hazards Program: Finite fault model: Preliminary result for slip history of 04/12/26 (Mw 9.0) , OFF W COAST of Northern Indonesia earthquake, *Website:neic.usgs.gov/neis/eq-depot/2004/eq-041226/neic_slav_ff.html*.
- Ji, C., D. J. Wald, and D. V. Helmberger (2002), Source Description of the 1999 Hector Mine, California, Earthquake, Part I: Wavelet Domain Inversion Theory and Resolution Analysis, *Bull. Seismo. Soc. Am.*, *92*(4), 1192–1207, doi:10.1785/0120000916.
- Kanamori, H., and J. Given (1981), Use of long-period surface waves for rapid determination of earthquake-source parameters, *Phys. of Earth and Planetary Interiors*, *27*, 8–31.
- Kao, H., and S. Shan (2004), The source-scanning algorithm: Mapping the distribution of seismic sources in time and space, *Geophys. Jour. Int.*, *157*(589-594), 589–594.
- Kikuchi, M., and Y. Fukao (1987), Inversion of long-period P-waves from great earthquakes along subduction zones, *Tectonophysics*, *144*, 231–247.
- King, G., Y. Klinger, D. Bowman, and P. Tapponnier (2005), Slip-partitioned surface breaks for the M_w 7.8 2001 Kokoxili earthquake, China, *Bull. Seismo. Soc. Am.*, *95*(2), 731–738.
- Klinger, Y., X. Xu, P. Tapponnier, J. Van der Woerd, C. Lasserre, and G. King (2005), High-resolution satellite imagery mapping of the surface rupture and slip distribution of the $M_w \sim 7.8$, 14 November 2001 Kokoxili earthquake, Kunlun fault, Northern Tibet, China, *Bull. Seismo. Soc. Am.*, *95*(5), 1970–1987.
- Klinger, Y., R. Michel, and G. King (2006), Evidence for an earthquake barrier model from $M_w \sim 7.8$ Kokoxili (Tibet) earthquake slip-distribution, *Earth Plan. Sci. Lett.*, *242*, 354–364.
- Komatitsch, D., and J. Tromp (2002a), Spectral-element simulations of global seismic wave propagation - I. Validation, *Geophys. Jour. Int.*, *149*(2), 390–412.

- Komatitsch, D., and J. Tromp (2002b), Spectral-element simulations of global seismic wave propagation - II. Three-dimensional models, oceans, rotation and self-gravitation, *Geophys. Jour. Int.*, *150*(1), 303–318.
- Kostrov, B. V. (1966), Unsteady propagation of longitudinal shear cracks, *PMM Journal of applied mathematics and mechanics*, *30*(6), 1241–1248.
- Krüger, F., and M. Ohrnberger (2005a), Tracking the rupture of the $M_w = 9.3$ Sumatra earthquake over 1150 km at teleseismic distance, *Nature*, *435*, doi:10.1038/nature03696.
- Krüger, F., and M. Ohrnberger (2005b), Spatio-temporal source characteristics of the 26 December 2004 Sumatra Earthquake as imaged by teleseismic arrays, *Geophys. Res. Lett.*, *32*, doi:10.1029/2005GL023939.
- Kuge, K., M. Kikuchi, and Y. Yamanaka (1999), Non-double-couple moment tensor of the March 25, 1998, Antarctic earthquake: Composite rupture of strike-slip and normal faults, *Geophys. Res. Lett.*, *26*(22), 3401–3404.
- Larmat, C., J. Montagner, M. Fink, Y. Capdeville, A. Tourine, and E. Clévedé (2006), Time-reversal imaging of seismic sources and application to the great Sumatra earthquake, *Geophys. Res. Lett.*, *33*, doi:10.1029/2006GL026336.
- Laske, G., and G. Masters (1996), Constraints on global phase velocity maps from long-period polarization data, *Jour. Geophys. Res.*, *101*(B7), 16,059–16,075.
- Lasserre, C., G. Peltzer, F. Crampé, Y. Klinger, J. Van der Woerd, and P. Tapponnier (2005), Coseismic deformation of the 2001 $M_w = 7.8$ Kokoxili earthquake in Tibet, measured by synthetic aperture radar interferometry, *Jour. Geophys. Res.*, *110*(B12408).
- Lay, T., and H. Kanamori (1985), Geometric effects of global lateral heterogeneity on long-period surface-wave propagation, *Jour. Geophys. Res.*, *90*(NB1), 605–621.
- Lin, A. M., B. H. Fu, J. M. Guo, Q. L. Zeng, G. M. Dang, W. G. He, and Y. Zhao (2002), Co-seismic strike-slip and rupture length produced by the 2001 M_s 8.1 Central Kunlun earthquake, *Science*, *296*(5575), 2015–2017.
- Lin, A. M., M. Kikuchi, and B. H. Fu (2003), Rupture segmentation and process of the 2001 M_w 7.8 Central Kunlun, China, earthquake, *Bull. Seismo. Soc. Am.*, *93*(6), 2477–2492.
- Liu, Q. (2006), Spectral-element simulations of 3D seismic wave propagation and applications to source and structural inversions, Ph.D. thesis, California Institute of Technology.

- McMechan, G. (1982), Determination of source parameters by wavefield extrapolation, *Geophysical Journal of Royal Astronomical Society*, *71*, 613–628.
- McMechan, G., J. Luetgert, and W. Mooney (1985), Imaging of earthquake sources in Long Valley caldera, California, 1983, *Bull. Seismo. Soc. Am.*, *75*(4), 1005–1020.
- Mori, J. (2001), Aftershocks and slip distribution of mainshock - Slip distribution of main shock, in *A comprehensive survey of the 26 January 2001 earthquake (Mw 7.7) in the state of Gujarat, India. Report by the research team supported by the grant-in-aid for specially promoted research provided by MEXT of Japan in the fiscal year of 2000*, edited by T. Sato.
- Mott, N. F. (1948), Fracture of metals: Theoretical considerations, *Engineering*, *165*, 16–18.
- Negishi, H., J. Mori, T. Sato, R. P. Singh, and S. Kumar (2001), Aftershocks and slip distribution of mainshock - Aftershock observations, in *A comprehensive survey of the 26 January 2001 earthquake (Mw 7.7) in the state of Gujarat, India. Report by the research team supported by the grant-in-aid for specially promoted research provided by MEXT of Japan in the fiscal year of 2000*, edited by T. Sato.
- Nettles, M., T. C. Wallace, and S. L. Beck (1999), The March 25, 1998 Antarctic plate earthquake, *Geophys. Res. Lett.*, *26*(14), 2097–2100.
- Nolet, G. (1987), Waveform tomography, in *Seismic Tomography: With Applications in Global Seismology and Exploration Geophysics*, edited by G. Nolet, pp. 301–322, Reidel Publishing, Dordrecht, The Netherlands.
- Ozacar, A., and S. Beck (2004), The 2002 Denali fault and 2001 Kunlun fault earthquakes: Complex rupture processes of two large strike-slip events, *Bull. Seismo. Soc. Am.*, *94*(6B), S278–S292.
- Park, J., C. Linderberg, and F. Vernon (1987), Multitaper spectral analysis of high-frequency seismograms, *Jour. Geophys. Res.*, *92*(B12), 12,675–12,684.
- Park, J., et al. (2005), Earth's free oscillations excited by the 26 December 2004 Sumatra-Andaman earthquake, *Science*, *3*(5725), 1139–1144.
- Percival, D., and A. Walden (1993), *Spectral Analysis for Physical Applications*, Cambridge University Press.
- Piatanesi, A., and S. Lorito (2007), Rupture process of the 2004 Sumatra-Andaman earthquake from tsunami waveform inversion, *Bull. Seismo. Soc. Am.*, *97*(1A), S223–S231, doi:10.1785/0120050627.

- Ritsema, J., H. J. van Heijst, and J. H. Woodhouse (1999), Complex shear wave velocity structure imaged beneath Africa and Iceland, *Science*, *286*(5446), 1925–1928.
- Robinson, D., C. Brough, and S. Das (2006), The M_w 7.8, 2001 Kunlunshan earthquake: Extreme rupture speed variability and effect of fault geometry, *Jour. Geophys. Res.*, *111*(B08303).
- Seno, T., and K. Hirata (2007), Did the 2004 Sumatra-Andaman earthquake involve a component of tsunami earthquakes?, *Bull. Seismo. Soc. Am.*, *97*(1A), S296–S306, doi:10.1785/0120050615.
- Slepian, D. (1978), Prolate spheroidal wave functions, Fourier analysis, and uncertainty. V: The discrete case, *Bell Syst. Tech. J.*, *57*, 1371–1430.
- Talagrand, O., and P. Courtier (1987), Variational assimilation of meteorological observations with the adjoint vorticity equation. I: Theory, *Q. J. R. Meteorol. Soc.*, *113*, 1311–1328.
- Tape, C., Q. Liu, and J. Tromp (2007), Finite-frequency tomography using adjoint methods—Methodology and examples using membrane surface waves, *Geophys. Jour. Int.*, *168*(3), 1105–1129, doi:10.1111/j.1365-246X.2006.03191.x.
- Tarantola, A. (1984), Inversion of seismic reflection data in the acoustic approximation, *Geophysics*, *49*, 1259–1266.
- Tarantola, A. (1987), Inversion of travel times and seismic waveforms, in *Seismic Tomography: With Applications in Global Seismology and Exploration Geophysics*, edited by G. Nolet, pp. 135–157, Reidel Publishing, Dordrecht, The Netherlands.
- Tarantola, A. (1988), Theoretical background for the inversion of seismic waveforms, including elasticity and attenuation, *Pure Appl. Geophys.*, *128*, 365–399.
- Thomson, D. (1982), Spectrum estimation and harmonic analysis, *IEEE Proc.*, *70*(1055–1096).
- Tromp, J., C. Tape, and Q. Liu (2005), Seismic tomography, adjoint methods, time reversal and banana-doughnut kernels, *Geophys. Jour. Int.*, *160*(1), 195–216.
- Tsuboi, S., M. Kikuchi, Y. Yamanaka, and M. Kanao (2000), The March 25, 1998 Antarctic earthquake: Great earthquake caused by postglacial rebound, *Earth, Planets and Space*, *52*(2), 133–136.
- van der Woerd, J., A.-S. Mériaux, K. Y., F. J. Ryerson, Y. Gaudemer, and P. Tapponnier (2002), The 14 November 2001, $M_w = 7.8$ Kokoxili earthquake in Northern Tibet (Qinghai province, China), *Seismological Res. Lett.*, *73*(2), 125–134.

- Vigny, C., et al. (2005), Insight into the 2004 Sumatra-Andaman earthquake from GPS measurements in southeast Asia, *Nature*, *436*, 201–206.
- Xu, X., W. Chen, W. Ma, G. Yu, and G. Chen (2002), Surface rupture of the Kunlunshan earthquake (M_s 8.1), Northern Tibetan plateau, China, *Seismological Res. Lett.*, *72*(441), 445–446.
- Xu, X., G. Yu, Y. Klinger, P. Tapponnier, and J. Van der Woerd (2006), Reevaluation of surface rupture parameters and faulting segmentation of the 2001 Kunlunshan earthquake (M_w 7.8), northern Tibetan Plateau, China, *Jour. Geophys. Res.*, *111*(B05316).
- Zhou, Y. (2004), Surface wave propagation in laterally heterogeneous media: with application to global upper-mantle tomography, Ph.D. thesis, Princeton.